Doctoral Dissertation

Developments of New Analysis Functions for the Muon Spin Relaxation Spectroscopy

[（ミュオンスピン緩和分光法の新解析機能の開発）]

Muhamad Darwis Umar

Graduate School of Science, Hokkaido University
Department of Condensed Matter Physics

September, 2021

Abstract

Developments of New Analysis Functions for the Muon Spin Relaxation Spectroscopy

by Muhamad Darwis UMAR

The muon spin relaxation method (μSR) is a powerful microscopic tool to probe electronic states of materials observing local magnetic field distributions on the muon. How to choose analysis functions is a key matter to deduce the information in physics from the μSR results in order to understand changes in electronic states in various temperature regions. It often happens that a distribution of local magnetic fields shows intermediate states between Gaussian and Lorentzian shapes. An intermediate μSR time spectrum can be considered as a cross-over distribution, which has characteristics somewhere between Gaussian and Lorentzian. For instance, in case that there are two independent field contributions, one having the Gaussian distribution and the other Lorentzian, the intermediate local field distribution can be realized. Another possible case is when the source is from one magnetic origin but the number of contributing magnetic spins is small though not one. Recently, another example to realize the intermediate μSR time spectrum was reported in the case that systems had non-uniform and/or low density distributions of nuclear magnetic moments. Organic molecular superconductors are typical examples showing this kind of distribution.

For the current study, we described the crossover field in terms of a convoluted function of Gaussian and Lorentzian. We derived the equation of the three-dimensional (3D) convolution in two ways. The first derivation uses the convolution integral starting directly in the 3D space. The other derivation starts from that of the one-dimensional (1D) convolution and make it to be converted to the 3D form. From the latter, we showed that the equation can be decomposed to a sum of three known convolutions. By applying the Fourier transform to this equation, we achieved the correct relaxation function for the zero-field condition, which was found to be given by a simple analytical equation. We also approximate 3D-convolution in the form of mixing 3D-Gaussian and -Lorentzian distributions with a weighting factor, and the approximation equation well approach the analytical one with maximum discrepancy 10% concentrated around the dip of approximation function. In addition, we tried to describe the intermediate analysis function under applied magnetic fields and under dynamic fluctuations on the basis of the development of the zero-field intermediate analysis function. Finally, we applied our developed analysis function to some μSR results in order to make sure its validity.

We fit the μSR time spectra of $\lambda - (\mathbf{BETS})_2\,\mathbf{GaCl}_4$ with a static analysis function, and the function well approach the μSR time spectra of the sample. The fitting results proposed the random internal fields are static at all considered temperatures indicating the local random local fields originate from nuclear dipole moments. The

dynamic function is applied to μSR time spectra of $La_{2-x}Sr_xCuO_4$ (x = 0.024) and the dynamic analysis function also well approaches the μSR time spectra. The fitting results suggest: 1. The intermediate relaxation between Gaussian- and Lorentzian-shape induced by the static parameter. 2. Nuclear dipole moment dynamics enter the μSR time windows caused by a coupled state with another sources of weak random fields.

Contents

List of Figures

List of Tables

Chapter 1

Introduction

1.1 Conventional Superconductor

Superconductivity is a phase of material signed by two main physical properties that are electrical resistance vanishes and magnetic flux fields are excluded from the interior of material. First property was observed by a Dutch physicist, Heike Kamerlingh Onnes, driven by his triumph in experimental work to successfully liquefy Helium in 1908 where He found the resistivity of Mercury (Hg) suddenly drops to zero when the temperature of Mercury decreases below 4.2 Kelvin as shown by Fig. 1.1.The second phenomenon known as Meissner effect were discovered by Walther Meisnerr and Robert Ochsenfeld in 1933 from measuring magnetic field distribution outside Tin (Sn) and Lead (Pb) materials during the material transiting into superconducting state.

1.1.1 Type I and Type II Superconductivity

There are two types of superconductor classified based on their respond to an applied magnetic field just below a transition temperature (T_c) respectively called type I and type II superconductors, see Fig. 1.1. In type I superconductor, magnetic flux will be suddenly and completely forced out from the interior of superconductor material (or perform a perfect diamagnetism) started at T_c. The applied magnetic field at T_c is called critical field (H_c). In the second type (type II superconductor), the penetrating magnetic flux is not completely excluded from the interior of superconductor material at T_c, and the applied field at which superconductor material starting to be in a mixed state (mixing metal and superconductor) is called upper critical field (H_{c2}). The remain penetrating magnetic flux (metallic region) will organize their self into regular pattern of vortices known as an Abrikosov lattice. The diameter of a vortex with cylinder shape is called the coherence length in which the order parameter does not change. The supercurrent flows around the vortex with radius called penetration depth of superconductor (λ) where the magnetic flux will decay exponentially from the edge of the vortex. When the magnitude of the applied magnetic fields at Tc is decreased, the size of the vortex also reduced until the second critical field or a lower critical field (H_{c1}) reached, all penetrated fields are completely forced

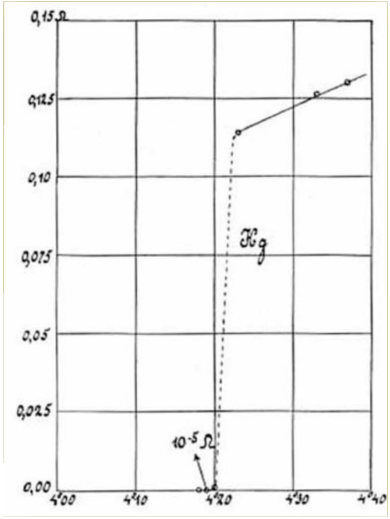

FIGURE 1.1: A plot-historic result of the resistance (ohms) versus temperature (Kelvin) performed by H. Kammerling Onnes in 1911 showing the superconductivity occurs at 4.2 K.

out from the interior of the superconductor material. Since the relation among magnetization $\vec{M}$, applied magnetic field $\vec{H}$ and magnetic flux density $\vec{B}$ expressed by a Maxwell equation

$$\vec{B} = \mu_0 \left(\vec{M} + \vec{H} \right) \tag{1.1}$$

then perfect diamagnetism $\left(\vec{B} = 0 \right)$ causing $\vec{M} = -\vec{H}$ being presented by Fig. 1.1.2. The magnetization is manifested as a surface current to screen the applied magnetic field.

1.1.2 BCS theory

The movement of electrons in an ionic lattice environment without dissipation has been a long challenging for theoretical physicists since superconductivity phenomena was observed. The theoretical pursuit of the physics mechanism underlying superconductivity phenomena expanded almost 50 years until Barden, Cooper and Schrieffer known as BCS theory [16] creating an established physics mechanism which includes a quantized lattice vibration called phonon. This theory was guided by experimental results finding the relation between T_c and isotope representing the effect of the mass of the lattice ions on the attractive Coulomb potential via the lattice vibration [133, 168]. According to the BCS theory, the superconducting state marks the formation of cooper pairs or the coupling of two fermion electrons with spin ½ via an attractive Coulomb force to form a boson- particle with spin 0 or 1. The average of the maximum distance of two coupled electrons as copper pairs is named coherence length (ξ), and since cooper pairs are boson particles, they can occupy the same state. In real space, the attractive force between two electrons is indirectly mediated by ionic lattice. When an electron passing the lattice of positively charged

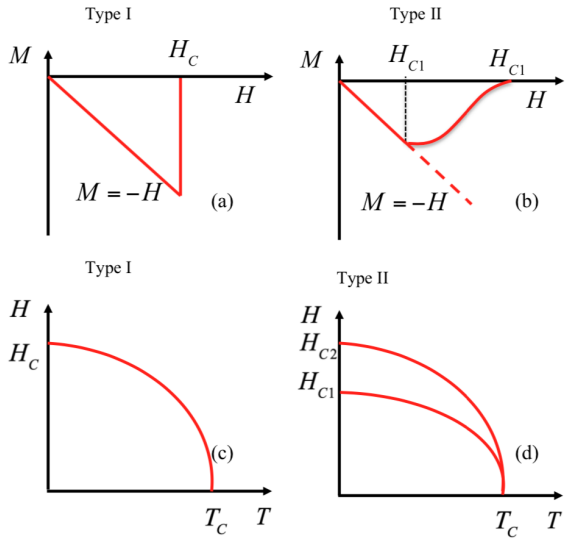

FIGURE 1.2: Panels (a) and (b) describe the magnetization $\|\vec{M}\|$ as a function of $\|\vec{H}\|$ in type-I and type-II superconductors. Panels (c) and (d) represent the $H - T$ phase diagram of type-I and type-II superconductors.

ions, the electron will disturb ions. The positive ions moving toward to the electron will increase the density of positive ions in the vicinity of the electron, and the excess of the density will attract the second electron, see an illustration in figure 1. 3. To reach the equilibrium position after changing their positions due to screening process, lattice ions will vibrate and propagate as phonon. The Coulomb attraction force between two electrons must exceed the Coulomb repulsive force between them. In momentum space, the cooper pairs can be understood as the exchange of phonon virtual. In superconducting state, there is no dissipation from electrons transport, and the momentum of cooper pairs from scattering process between electrons and lattice ions conserves, whereas the difference of total kinetic energy between before and after scattering will be transformed in to attractive coulomb potential. From momentum conservation, the first electron will release phonon followed by decreasing the magnitude of the momentum electron and changing the momentum direction, meanwhile the second electron will absorb the phonon, and increase the magnitude of momentum and also change momentum direction, see Figure 1. 3. The maximum gap will occur when the momentum of two-particle is in opposite direction.

The superconductor materials in which the pairing mechanism is based on the phonon exchange are called conventional superconductors. The attractive Coulomb potential to bound two electrons depends on energy of electron being considered (ω) and Deybe frequency $(\omega_D)$where the attractive potential can be approximated by an equation

$$V_{\mathbf{eff}} = |g_{\mathbf{eff}}| \frac{1}{\omega^2 - \omega_D^2}, \tag{1.2}$$

where $|g_{\mathbf{eff}}|$ describes probability of the fist electron to emit a virtual phonon and the

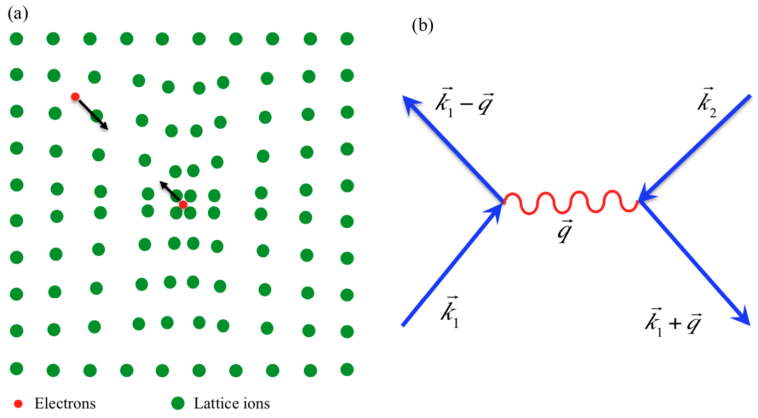

FIGURE 1.3: Panels (a) illustrates the attraction of two electrons mediated by lattice deformation. Panel (b) describes the process of cooper-pair formation in momentum space where the first incoming electron in state $\vec{k_1}$ will release virtual phonon $\vec{q}$ and change his momentum into a new state $\vec{k_1} - \vec{q}$, the second incoming electron in a state $\vec{k_2}$ will absorb the virtual phonon and change its momentum into $\vec{k_2} + \vec{q}$

second electron to absorb the virtual phonon. The superconducting gap of conventional superconductors has s-wave symmetry. It means cooper pairs will have the uniform attractive Coulomb potential in any direction (isotropic) in Fermi surface. Energy to break the cooper pairs is proportional to the superconducting gap. As in Eq. (1.2), the maximum transition temperature for conventional superconductor will be determined by frequency Debye or the theoretical value of maximum frequency of phonon in material. The theoretical prediction of maximum transition temperature for conventional superconductor is around 30 K.

1.2 Cuprate-Based High Temperature Superconductivity

Bednorz and Müller discovered the superconductivity phenomenon in the copper oxide perovskite $La_{2-x}Ba_xCuO_4$ as a new class of superconductor in 1986 [20]. The temperature transition of the $La_{2-x}Ba_xCuO_4$ material is 35 K [20]. Comparing to previous class superconductor such as alloys, binary compounds, heavy fermion and organic superconductors, the cuprate-based superconductor reaches the highest recorded transition temperature 135 K at the normal atmosphere pressure and 165 K under pressure for HgBaCaCuO material. Besides the transition temperatures of the cuprate-based superconductor dominantly exceed the highest temperature of the theoretical prediction based on phonon exchange or BCS theory that is around 30 K, there are some properties of cuprate-based superconductors differentiating them from conventional superconductor:

1. The superconducting state originates from a doping process on the parent compound that is an antiferromagnetic insulating material. This indicates the relation between superconductivity and magnetism.

2. Cuprate-based superconductor materials have layered structure induced the strongly difference between resistivity at $a - b$ plane and c direction.

3. In normal state, the resistivity values of cuprate-based superconductor are greatly bigger than metal-based superconductors in two orders.

4. The conduction carrier density is much lower than metal-based superconductor in two orders.

The general crystal structures of cuprate-based superconductors consist of two kinds of layer. The cooper oxide plane plays role as a conducting plane sandwiched by insulating layers playing role as charge reservoir. The number of conducting layers in crystal unit of the different cuprate-superconductor materials varies from 1 to 3 (see figure 1.2.1) and more than 3 layers for HgBa2$Ca_{n-1}Cu_nO_y$, TI$Ba_2Ca_{n-1}Cu_nO_y$, (Cu, C)$Ba_2Ca_{n-1}Cu_nO_y$, (Cu, V) $Ba_2Ca_{n-1}Cu_nO_y$, (Cu, Cr) $Ba_2Ca_{n-1}Cu_nO_y$ and (Cu, C, N) $Ba_2Ca_{n-1}Cu_nO_y$ [82] where the transition temperature shows a dependence on the number of conducting layers with the maximum Tc coming from 3 CuO2 layers cuprate-based material as shown in Fig. 1. 5. [82]. The charge carriers will emerge in the conducting plane when the ratio number of oxygen elements changes, and the ionic element at insulating layers is replaced by other elements with different ionization degree for instance La^{3+} replaced by Sr^{2+} in $La_{2-x}Sr_xCuO_4$ material. Fig. 1. 6. show that the doping process can be done on both electron-doped or hole doped, and the phase transition between the two difference class of doping show the similar pattern in the recent experiments indicating the same pairing mechanism.

Cuprate-based high temperature superconductors are type-II superconductor. The normal state of these materials are still incompletely defined, so electrons state in vortex regions has taken a long attention. In 2002, [34] suggested a modulation of conduction-electron density in real space known as charge density wave (CDW) coexisting with antiferromagnetism presents in vortex region of $Bi_2Sr_2CaCu_2O_{8+\delta}$ material. But, later in 2016, the electrons at vortex region were detected in the form of a modulation Cooper pair or called pair density wave or PDW in the same material [65]. Fulde and Ferrel [59] as well as Larkin and Ovchinnikov [107] separately predicted the PDW state in 1964. According to the two separate proposed models, magnetic field applied to material which is in superconducting state and containing magnetic impurities will induce ferromagnetism exchange interaction among magnetic impurities, and the ferromagnetic spins and Cooper pairs which interact each other with comparable the exchange and superconducting-gap energies will create a new ground state in the form of PDW [59, 107].In cuprate-based material, the ferromagnetism may take place in the background of Cu spins. The recent detection of PDW has been driven not only intense theoretical and experimental researches to

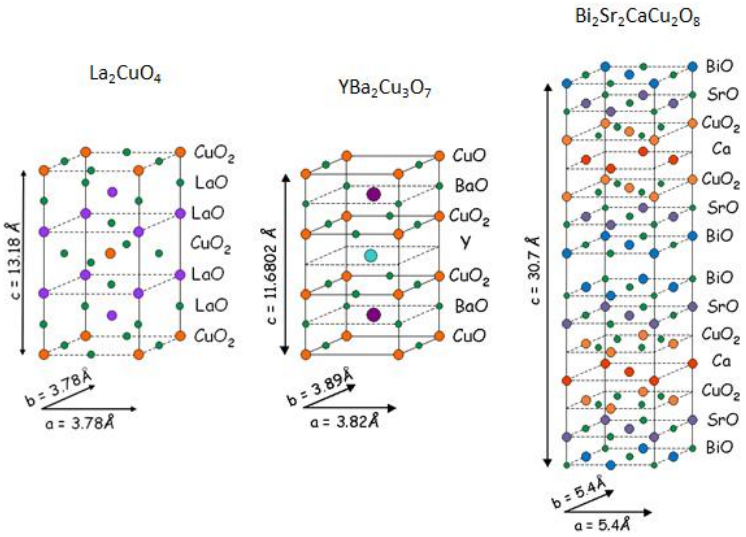

FIGURE 1.4: The crystal structure of LSCO, YBCO and BSCCO respectively representing 1, 2 and 3 conducting layers (copper oxide planes) in every crystal unit [52]

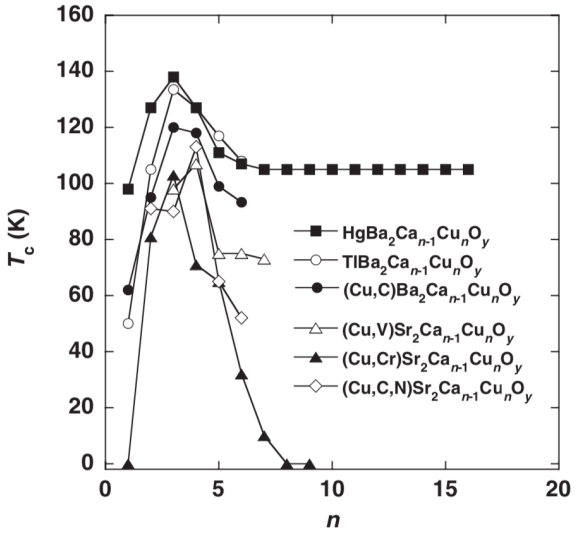

FIGURE 1.5: The transition-temperature (T_c) dependence of the number of conducting layers (n) [82]

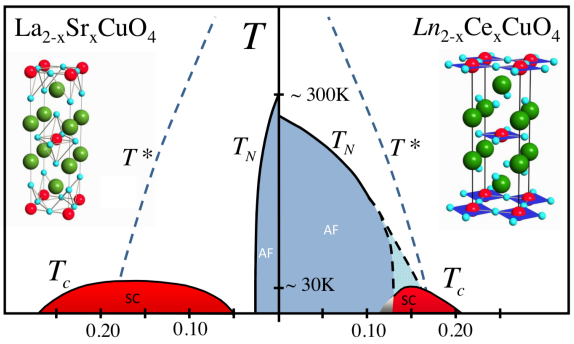

FIGURE 1.6: Schematic diagram of hole-dope $La_{2-x}Sr_xCuO_4$ and the electron-doped $Ln_{2-x}Ce_xCuO_4$ [56]

study PDW's role and its interrelation with charge density wave in pseudogap and bad (strange) metal regimes of cuprate-phase diagram, but also another challenge in order to found the comprehensively theoretical model of pairing mechanism in cuprate-based material.

The superconducting gap of cuprate-based materials is anisotropy because of having d-wave symmetry [225, 202], and the gap shown an independence of doping concentration. Since the wave function of two-fermion particles (or a Cooper pair) must be antisymmetric, and the spatial (orbital) wavefunction of cuprate-based material is corresponding to d-angular momentum that is even $(l = 2)$, then spin wavefunction of cooper pairs must be singlet (or antisymmetric). There are nodals at 2-dimensional $k-$space that are $\theta = 45°, 135°, 225°$ and $315°$ as in Fig. 1.2.4. The nodal can be interpreted as the state of cooper pairs without attractive Coulomb potential (or zero gap), or, in this direction, electrons will be in metal state and experience resistance, so to avoid the dissipation, the electrons will prefer to be in direction at which they will be in superconducting state or moving without resistance. Getting away from nodals, the superconducting gap will increase and reach a maximum value at anti-nodal with $\theta = 0°, 90°, 180°$ and $270°$, see Fig. 1.7. The trend of the ratio change of the energy gap (2Δ) to transition temperature T_c in cuprate-based material is different from conventional superconductor [78], and the experiments in different cuprate materials shown that the superconducting gap deviates from simple $d-$wave form as a function of doping concentration [66], The difference of superconducting gap symmetry from conventional superconductors ($s-$wave symmetry) indicate the difference of pairing mechanism between two different classes of superconductor. Since the superconductivity in cuprate-based materials was observed in 1986, it has no been yet consensus on the pairing mechanism. There are generally two theoretical models to explain pairing mechanism. The first theoretical model is based on BCS-like theory in which the pairing mechanism needs mediator such as vibration lattice, meanwhile in the second theoretical approach; cooper pairs do not need a mediator. There are several models based on BCS-like theory. The first idea comes from Müller [142]. Since the distance of the apical oxygen with respect to Cu

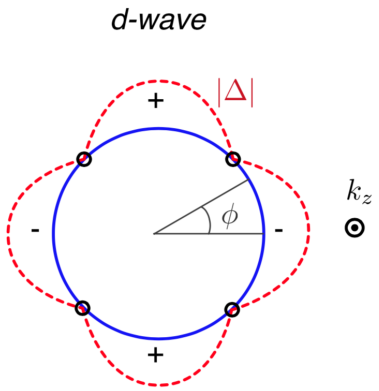

FIGURE 1.7: The change of superconducting gap on Fermi surface, blue circle line is two-dimensional Fermi surface. The red dashed line represents the wave of superconducting gap on Fermi surface [167]

ion in CuO_6 octahedron or CuO_5 pyramid clusters is longer than the distance of planar oxygen to the same Cu atom due to Jahn-Teller effect, the hole-doped will induce anti-Jahn-Teller effect where apical oxygen will approach Cu atoms. The deformation of octahedrons or pyramid structures due to anti-Jahn-Teller effect will couple with hole as polarons. These polarons is named Jahn-Teller polarons. According to Alexandrov and Mott [4], the Jahn-Teller polarons possibly form a bounded pairs called bipolaron at which they can condensate to superconducting state as bosonic particles when electron-phonon coupling is large [88]. Other BCS-like theories are based on different mediators to bound electrons as cooper pairs. Since phonon as spin 0 or 1 particle (called boson particle) is a quasiparticle generated by a collective excitation in the background of lattice vibration, the emergence of phonon is formally called bosonic excitation.

The magnetic coupling between electron- or hole-quasiparticles with dynamical spin fluctuation firstly proposed to be responsible for pairing mechanism [28, 183, 138, 140]. The dynamical spin fluctuation takes place in the background of antiferromagnetic spin or spin density wave (SDW) fluctuations in the forms of commensurate or incommensurate antiferromagnetism in a localized or an itinerant electron system [54]. In spin-fluctuation driven superconductivity, the quasiparticle generated by a collective excitation in the background of antiferromagnetic spin or SDW fluctuation will play role as mediator like phonon in conventional superconductor. The quasiparticle due to the SDW fluctuation is a short range of quantized spin wave called paramagnon antiferromagnetic. The phase diagram of cuprate-based superconductor materials as showed in Fig. 1. 8. [38] suggests the competition between antiferromagnetism and superconductivity since the robust of long-range antiferromagnetic order followed by the emergence of superconductivity. Y. Ando *etal*. [13] reported the hole mobility of LSCO material is proportional to invers of antiferromagnetic correlation [13], however SDW is found coexisting with the superconducting state in the underdoped regime of LSCO as shown in figure 1. 2. 5. In the real

space, the spin fluctuation will induce the change of exchange energy between metal electrons. Because the exchange energy basically represents a Coulomb interaction depending on spins structure, the change of the exchange energy will directly represent an additional attractive coulomb potential (force) to form Cooper pairs and induce a phase transitions from metal to superconducting states. The spin fluctuation is believed to be generated by quantum fluctuation originating from opening a quantum critical point (QCP) above zero temperature. The QCP is a concentration or pressure generating a second order of phase transition in zero temperature. It is similar to SDW fluctuation; the fluctuation of orbital current modeled by Varma [207, 208, 210, 211] has been also proposed to interact with electrons in order to mediate cooper pairs [35]. Quantum criticality in Varma' scenario is driven by the instability of hybridization of $d-p$ orbitals due to doping or pressure treatments. In one of new recent proposals based on incompletely coupled holes between oxygen and Copper atoms as Zhang-Rice singlet, Barzykin and Pines proposed two coupled components model where a part of localized Cu spins forms spin-liquid state, a part of holes plays role as conduction hole and the remain Cu and O atoms will hybridize [19]. In this scheme, a quasiparticle coming from an excitation in spin liquid state will mediate electrons to condensate to superconductivity state as cooper pairs [28]. Spin-liquid is a state in which there is strong exchange interaction between spins, but spins are still in disordered state and fluctuate even at temperature close to zero, whereas the hybridization in this context is a superposition of $d-$ and $p-$orbital to form new states with energy being higher than $d-$ and $p-$orbital known as anti-bonding state and lower energy known as bonding state.

Another BCS-like model is based on charge-density-wave (CDW) fluctuation [30, 158, 9]. CDW is a modulation of the density of conduction electron [239]. CDW can come from by electron-phonon interaction or Fermi nesting and electron-electron interaction [239]. In the scenario of the Cooper pair mediated by CDW fluctuation, the quasiparticle from a collective excitation in background of CDW fluctuation will play role as phonon playing in conventional superconductor. It is like the spin fluctuation, the charge fluctuation in weak-coupling approximation is also proposed to be induced by quantum fluctuation due to electron-phonon interaction generated by doping or pressure where the QCP will open above zero temperature [30]. Quantum fluctuation it self is fluctuation driven by Heisenberg uncertainty and not by thermal energy. The fluctuation of CDW in LSCO material was observed above T_c as shown in Fig. 1.2.4. The neutron scattering and x-ray diffraction studies indicated CDW and superconductivity compete each other [38]. Meanwhile a theoretical study predicted that static CDW will suppress superconductivity, but the fluctuation of CDW will mediate superconductivity [30]. The last model of BCS-like theory proposed to understand the pairing mechanism in cuprate-based superconductor is based on the coupling of the inharmonic vibration of oxygen planar in CuO2 plane and metal electrons (holes). In this scenario, the bosonic excitation in the background of inharmonic vibration of oxygen planar clusters will play role as a mediator to pairing

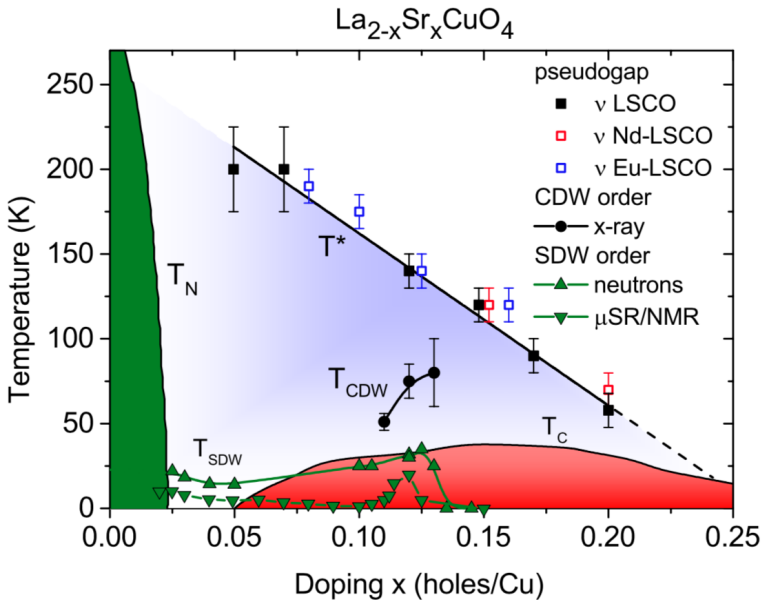

FIGURE 1.8: Phase diagram of LSCO material, the green lines are temperatures at which SDW or incommensurate antiferromagnetic order observed by neutron scattering, nuclear magnetic resonance (NMR) and muon spin relaxation/rotation/resonance (μSR) [38]

mechanism [73].

Besides BCS-like models, there is a model of superconductivity without pairing mechanism knows as RVB theory. This model was proposed by Anderson [10] and developed by other condensed matter Physicists. The main idea of this model is that spins of Cu atoms in CuO_2 planes will be in a superposition of all-possible configuration of singlet pairs. Singlet state is an antisymmetry coupling between two electron/hole spins where the total magnetic moment of two spins at ground state is zero, whereas antisymmetry means that the wavefunction of spin will change from positive to negative or vice versa when we change the particles. In RVB theory, the excitation in a liquid of singlets is spin = ½ called chargeless spinon. The chargeless means the excitation with respect to the ground state does not change the number of charges as a whole. Whereas, a doped hole will break a singlet and produce a holon that is a charge particle without spin and a spinon with respect to the ground state. In this separation scenario, spinons and holons can move independently, even though the well-defined quasi-particle above T_c around Fermi-arc has driven another proposal on the coupling of the spinon and the holon to form quasiparticle propagating with both spin and charge in pseudogap regime. The liquid character of resonating singlet pairs make holes be able to coherently propagate through them and become super current at low temperatures [95]. In strong coupling limit of Hubbard model, or onsite Coulomb interaction is much bigger that kinetic energy of hopping, with a single band model constructed by Zhang-Rice singlet known as $t-j$ model, the recombination of spinon and holon will take place below the crossover

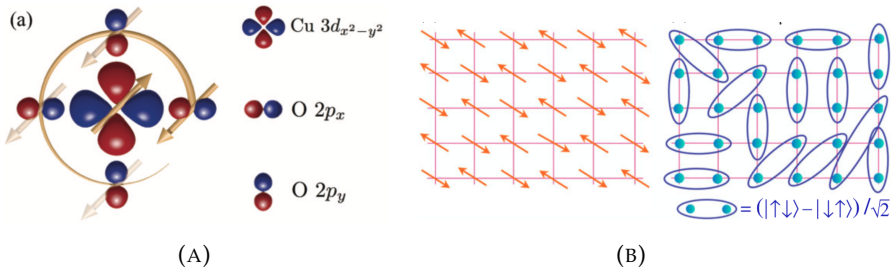

FIGURE 1.9: The above panel (A) is the schematic formation of Zhang-Rice singlet, hole in an oxygen site spread out in four-planar oxygen, and the hole spins at Cu and O sites are coupled as singlet [33]. The below panel (B) is an illustration of one possible of singlet combination in antiferromagnetic background lattice. The RVB state is all possible combination of singlet [174]

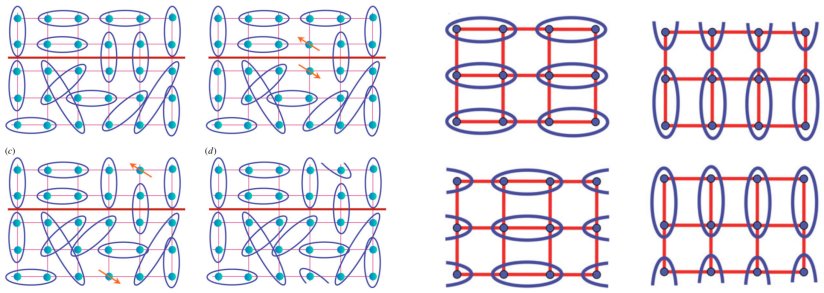

FIGURE 1.10: represent the excitation of a singlet will produce two spinons (two spin particles without charge), the two spinons will move in a certain the background of singlet combination and produce a new combination of singlet or induce resonance in singlet combination [174]. The right panel represents the formation of only short range of singlet known as Valence-Bond-Solid (VBS) [174]. The light and blue circles represent Cu spin and the ovals represent singlet of two Cu spins.

between temperature singlet formation and temperature of coherent holon formation [88]. In the same spirit as RVB state, another model proposes that the ground state of spins state in CuO_2 planar is only short range of RVB state also know as valence-bond-solid (VBS) [176]. The illustration of the formation on Zhang-rice singlet, RVB and VBS state is respectively presented by Fig. 1. 9 and Fig 1. 10.

Emery *etal*.proposed another scenario of the superconductivity mechanism in cuprate-based superconductor based also on spin-charge separation [49]. In this model, the superconductivity occurs when charge pairs in charge stripe or 1-dimensional electron gas hop between charge stripe and spin-stripes (antiferromagnetic stripes) that is in spin-gap state. This mechanism can be understood due to a magnetic proximity effect [49].

1.3 $La_{2-x}Sr_xCuO_4$ (LSCO)

$La_{2-x}Sr_xCuO_4$ is the member of first group of cuprate-based superconductors discovered, just around two years after $La_{2-x}Sr_xCuO_4$ being reported. This material has been intensively investigated since it was the simplest cuprate-based superconductor making easier to prepare a high-quality sample, furthermore it can be conducted subsequent characterization. The parent of this compound is La_2CuO_4, and without doping, it exhibits antiferromagnetic insulating behavior. In high temperature this material has a body-centered tetragonal structure tetragonal structure $(I4/mmm)$ known as high-temperature tetragonal (HTT) with lattice constants being $a = b = 3.78A^\circ$. When temperature decreased, HTT will transform to orthorhombic structure $(Bmab)$ known as low-temperature orthorhombic (LTO) at temperature 520 K [85, 93]. The lattice constants of LTO structure are $a = 5.35A^\circ$, $b = 5.4A^\circ$ and $c = 13.2A^\circ$. The structural transition temperature will dramatically decrease by increasing doping concentration and end at superconducting state with Sr-concentration around 20%,see Figure 1.2.5. The structural transition from HTT to LTT followed by uniformly tilting of octahedral about 4$\circ$ at $a - b$ plane [90], see Figure 1.3.1.

The Neel temperature of LCO is approximately 325 K [164], and spins of Cu antiferromagnetically ordered with the magnetic moment of each Cu atom being around $0.5\mu_{\mathbf{B}}$ [206].This observed value is almost a half of theoretical value for Cu^{2+} ion that is $\mu = g\langle S\rangle \mu_{\mathbf{B}} \cong 1.1\mu_{\mathbf{B}}$ with lande factor for Cu^{2+} ion $g \cong 2.2$ [164] and $\langle J\rangle = \langle S\rangle$ due to orbital quenching induced by crystal electric field. This reduced value of the magnetic moment is addressed to quantum spin fluctuation [125] and the covalency of Cu-O bonding in cuprate-based superconductor material [215, 134]. According to Hubbard model, the localized spins Cu as a Mott insulator is caused by strongly onsite Coulomb interaction at $d-$orbital of Cu atoms, and the antiferromagnetic long-range order is underlined by the virtual hoping of electrons between Cu and O atoms. From fig 1. 2. 4, the antiferromagnetic order below Neel temperature (T_N) will dramatically robust by the doping process, and long-antiferromagnetic order will vanish at Sr concentration around 2%. The Sr doping makes hole emerge in oxygen site and causes O^{-2} changing to O^{-1}. The spin ½ at oxygen site located between two Cu spins will induce a magnetic frustration due to competitions between ferromagnetic and antiferromagnetic exchange interactions.

Above 2% concentration, two-dimensional short-range magnetic order as SDW observed until partially coexist with superconductivity as shown in Fig. 1.12. At concentration about 12.5%, magnetic and charge structures in the form of spin and charge stripes show in a competition with superconductivity and make T_c with a dome structure suppressed. Meanwhile, the magnetism at what it is generally called pseudogap state is still unclear. The pseudogap region in phase diagram of LSCO is still unclear whether its region expands in a fixed range of concentration and coexist with other states for instance superconducting state. Even though the emergence temperature of pseudogap called as star temperature (T^*) seems to be universal

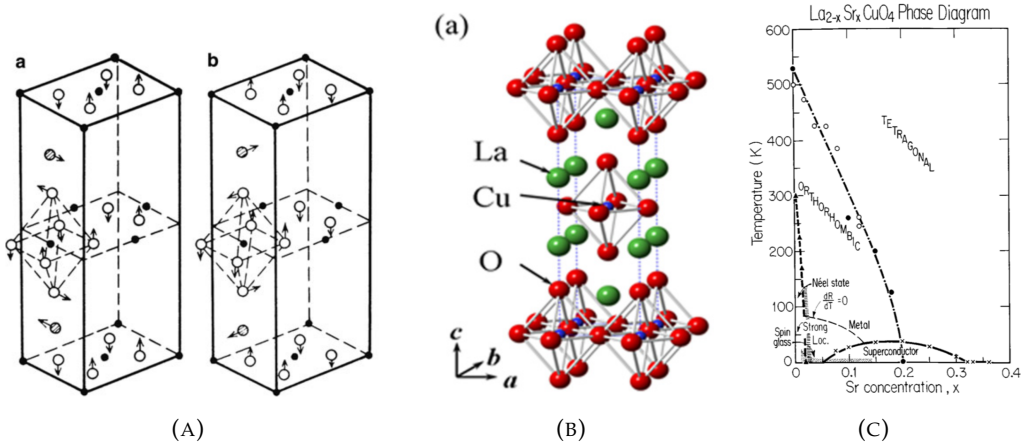

(A) (B) (C)

FIGURE 1.11: A. The tilting of octahedral structure in two domains of orthorhombic phase [164]. (B) a tetragonal structure of [71]. (C) Structural transitions temperature in earlier phase diagram of LSCO [90]

from various different experimental techniques. A recent resonant soft X-ray scattering spectroscopy in LSCO revealed that CDW short-range order exists from above T_c to coexistence with superconductivity state until 18% Sr-doping concentration and partially transform into CDW stripe close to the superconducting T_c [222]. Another suggested temperature due to magnetic order formation occurred in normal state of LSCO is magnetic temperature called $T_{\mathbf{mag}}$ as shown in Fig 1.12. This temperature is the onset temperature of orbital-current order with two different direction of magnetic moments in each unit cell observed by neutron stattering [14]. This sugested temperature is also a debatable issue in line with other intepretations from different measurements.

The superconducting state starts emerging at 5% Sr concentration, and T_c increases with the concentration ranging up to around 16.2% called underdoped regime and reaches the highest T_c around 38 K. The concentration at which T_c has a maximum value is called optimaldoped. Above optimaldoped temperature, T_c monotonically decreases, and superconductivity totally vanishes at Sr concentration about 27%. This range concentration is called overdoped regime. At highly overdoped regime, electrons is generally assumed exhibiting Fermi liquid behavior (or normal metal), however a μSR experiment indicates the presence of ferromagnetism at low temperature as shown in Fig 1.12 [192].

1.4 Pseudogap State in $La_{2-x}Sr_xCuO_4$

Superconductivity is generally understood as the instability of the normal state [150]. In the conventional superconductor, the normal state is a metal state, and the superconductivity phase transitions are induced by the instability of conduction electrons in Fermi surface due to the pairing mechanism. On contrary, the normal state

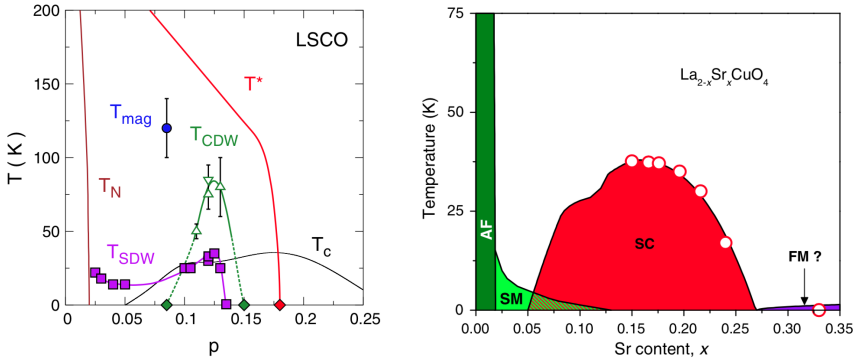

(A) (B)

FIGURE 1.12: (A). The phase diagram of LSCO as a function of temperature and doping concentration, the blue filled circle is the proposed temperature $T_{\mathbf{mag}}$ of orbital current orders, $T_{\mathbf{CDW}}$ is temperature at which CDW observed [192]. The right figure shows the onset of ferromagnetism emerging at highly overdoped regime detected by μSR [40]

of cuprate-based superconductor material is not normal metal and has not completely understood. In the cuprate-based superconductor, the normal state preforms anisotropic gaps in charge and spins excitation [110]. The charge-gap is the lowest excitation energy from the ground state of n particle number to ground state of the (n$\pm$1) particles number. In ARPES experiment, charge gap is generated by photoelectric effect at which an electron will be released from the closest state from Fermi energy, or state crossing Fermi energy. Meanwhile spin-gap is the lowest excitation energy from the ground state of n-particle to the lowest-lying n-particle excited state with spins of the particles rearranged in comparison with the spins of the particles in the ground state. It there has been not consensus on whether the pseudogap and superconducting are the same or different gaps. For two-gap model supported by ARPES, Raman-spectroscopy and STM experiments, the pseudogap and superconducting gap are different gap since pseudogap shown the dependence on doping concentration [74]. The above normal state of underdoped regime, the fluctuation of CDW is also observed [38]. Even though, the emergence of PDW from experimental interpretation has recently driven the possibility of the same detected physical object between CDW and PDW in pseudogap state [149]. Different experimental techniques have been carried out to study pseudogap in LSCO material, and mostly shown deviations from normal metal behavior.

Fig. 1.13 (left panel) shows NMR results from Ohsugi et al. [151]. From the figure, Knight shift shows temperature dependence and decrease without a peculiarity when passing T_c. The Knight shift that is proportional to spin susceptibility describes the interaction of nuclear and electronic spins via the Fermi contact (isotropic) and dipole-dipole interaction (anisotropic). Since the fall of the Knight shift off below T_c is caused by the singlet formation of copper pairs with spin gap, the decline of Knight shift at pseudogap state at earlier observation is directly linked

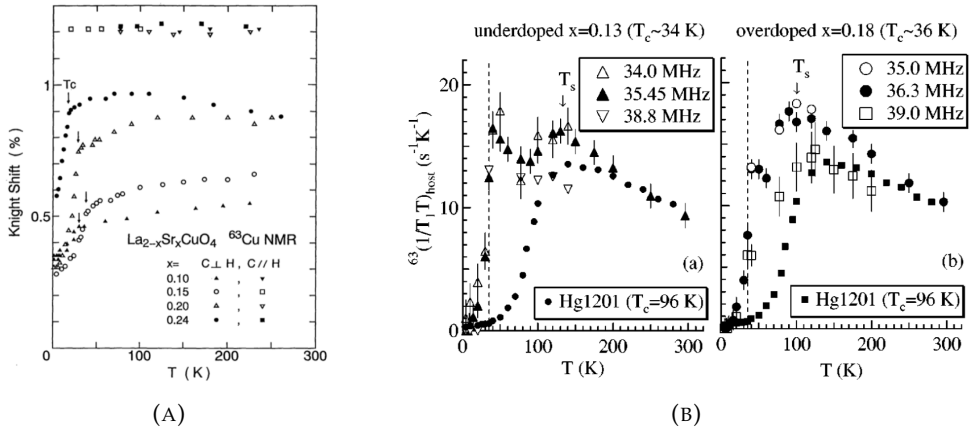

FIGURE 1.13: (A) a Knight shift shows a dependence on temperature above Tc [151]. (B) the invers of relaxation time temperature forms a dome structure indicating the spin gap formation, the second peak of 13% Sr concentration is discussed as gapless spin excitation [81].

to the spin-gap formation. However the decrease of the Knight shift shown unclear form between an exponential and power-law like still remains an antiferromagnet-singlet debate [146]. Another signature of the spin-gap formation in pseudogap is also indicated by the invers of relaxation time temperature $(1/T_1T)$ dependence of temperature from NMR experiments or do not obey Korringa law. The right panel of the Fig. 1.13, from a high temperature, shows that $1/T_1T$ representing the rate of energy exchange between the depolarization of nuclear moments and its environment (spin and lattice) to reach thermodynamically equilibrium almost linearly incline with the dropping of temperature addressed to antiferromagnetic fluctuation, until a maximum value, with a moderately broaden dome, $1/T_1T$ show monotonically decrease when temperature approach Zero. This behavior then is linked to the spin gap formation [81]. Even the decrease of invers T_1T can be interpreted in framework spin-gap as singlet formation of RVB state or ladder structure, the decrease can be also possibly interpreted in the framework of antiferromagnetic correlation [63].

Another NMR measurement carried out by Fujiyama et al. [58] on underdoped LSCO material with various Sr concentrations shows the presence of a spin excitation in pseudogap state and being addressed to spin-pseudogap formation. As shown in Fig 1.3.2, their $1/T_1T$ data changes with Currie-Weiss behavior when temperature decrease from high temperatures until certain temperatures indicated as T^*, the trend undergoes a change from Currie-Weiss behavior [58]. The trend also takes place on YBCO sample as shown by Matsumura et al. [129].

Anomalous behavior of the normal state of underdoped regime was also seen in resistivity and optical conductivity measurements. Resistivity in pseudogap state is usually fitted by two components that are a quadratic temperature representing Fermi liquid behavior due to electron-electron interaction and linear temperature describing unusual or unconventional term [198]. The presence of pseudogap state in resistivity measurements is marked by a change of the gradient of linear resistivity

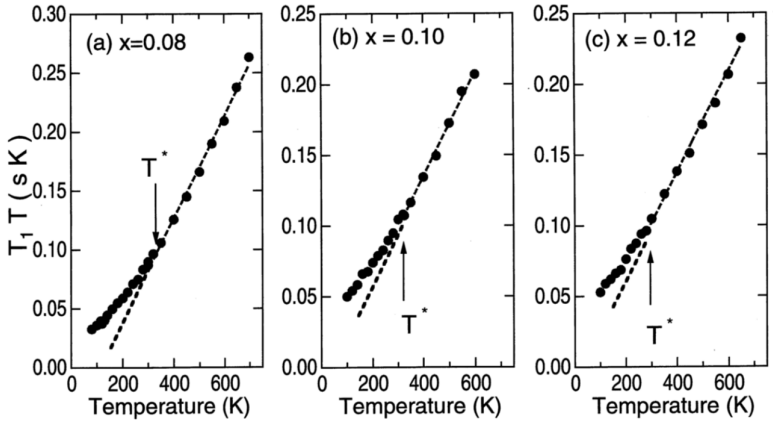

FIGURE 1.14: The invers of relaxation time temperature from NMR data undergoes a change from Curie-Weiss behavior indicating spin excitation [58].

with respect to temperature as shown by Nakamura and Uchida [148], see fig. 1. 4. 3. If we approach resistivity measurement with Drude model (or free electron gas model) depicted by an equation

$$\rho = \frac{m^*}{ne^2\tau} \tag{1.3}$$

with n is carrier density, m^* is effective mass of charge carrier and $1/\tau$ is scattering rate. Because the number of electron or Fermi surface cannot increase by the decreasing of temperature due to the constrain of Fermi-Dirac distribution, then the decrease of gradient of resistivity dependence of temperature as in fig 1. 4. 3 will be induced by either the decrease of scattering rate or the increase of effective mass. Assuming that effective mass is constant with temperature, the gradient change from linear resistivity should originate from the reducing of scattering rate. In line with spin gap formation suggested by NMR measurement, the change of gradient of resistivity with respect to temperature earlier was explained in line with the scattering electrons (holes) due to exchange interaction of the antiferromagnetic spin fluctuation. The change of gradient of the resistivity with respect to temperature as shown by [148, 12], only occurs in underdoped samples, oppositely the linear trend become a universal signature in overdoped regime [115].

There were two scenarios to explain the change of resistivity in line with spin fluctuation. In RVB theory, T^* marks the formation of singlet pairs in background of localized spin Cu atoms, and this formation make the scattering rate by spin fluctuation reduce. Other scenarios propose T^* as a crossover region from antiferromagnetic correlation from bad (strange) metal to a state at which the antiferromagnetic correlation becomes well-developed for instance the correlation length according to nearly antiferromagnetic Fermi liquid model [18]. While another interpreted T^* marking a fluctuating precursor of the order for example spin and charge stripes [96]. Scaling done by Nakamura and Uchida also shown the interesting fact on the

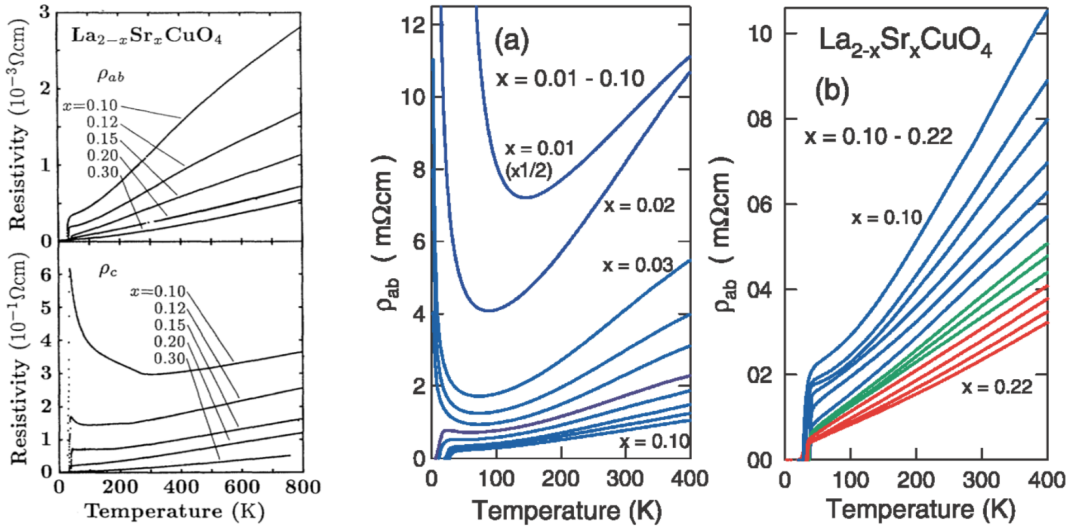

(A) (B)

FIGURE 1.15: The left picture (A) is resistivity data from Nakamura and Uchida [148], the data shows the change scattering rate due to pseudogap formation. The right picture (B) shows the a-b plane behavior as a function of hole-doped concentration and temperature [12].

difference of resistivity behavior for Sr concentration 10% in which localization of hole in c direction occurs in normal state of underdoped sample of LSCO. It is like in YBCO case [228], there are two different theoretical models which have been proposed to explain the anisotropic results of resistivity that are an interaction between metal electrons in background of spin fluctuation [171] and recombination holon-spinon from $t - j$ model with RVB state [145]. Meanwhile Ando *etal*. [12] clearly performed that localization of hole occurs in $a - b$ plane from sample with lightly under-doped concentration. These results also have earlier reported by Bernegie *etal*. [24].

The change of resistivity due to a scattering process was also shown from optical conductivity. The fig. 1.16 shows the data from an optical conductivity experiment conducted by Startseva *etal*. [194]. By using the Drude model to interpret the data, the result shows the suppression dependence of the scattering rate with respect to temperature in a low frequency range $\left(< 700\mathbf{cm}^{-1}\right)$, whereas at high temperature the scattering rate shown a temperature independence. The result of scattering rate from the optical conductivity is equivalent to the change of gradient of resistivity with respect to temperature from the resistivity measurement. The increasing of effective mass that is correspond to the suppression of the scattering rate in LSCO material with 13% and 14% Sr concentrations as shown in Fig. 1. 16. (c and d) clearly depicts the onset of charge-gap formation as shown in ARPES experiment.

The reduced scattering rate corresponding to the increase of mobility was also reported from Nernst effect experiment. The Nernst signal is approximately expressed

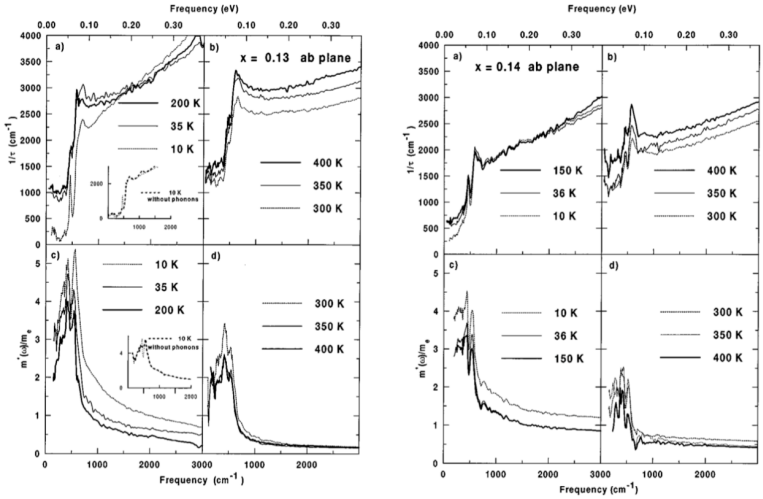

FIGURE 1.16: The optical conductivity data is fitted by the Drude model. The increasing of effective mass and the suppression of scattering confirm the result of the resistivity measurement. The increasing of effective mass shows a gap formation [194].

by [21, 22]

$$\frac{|v|}{T} \approx \frac{\pi^2 k_B^2 \mu}{3e\epsilon_F} \tag{1.4}$$

with v is Nernst coefficient, μ is mobility and ϵ_F is energy Fermi corresponding to electron (hole) density. It is not like in metal state where the Nernst signal is constant, the presence of pseudogap state makes the Nernst signal increases with temperature as shown in Fig. 1.17. The temperatures where Nernst coefficient starts inclining are consistent with T^* from resistivity measurements [12]. From Eq. (4), the increase of Nernst signal must come from both the decreasing of energy Fermi and the increasing of hole mobility that directly link to the falling of scattering rate. Since the Fermi energy is proportionally correspondent to the size of Fermi surface, then the change of Fermi energy then is linked to reconstruction of Fermi surface due to doping process where the doping process cause the formation hole and electron pockets relatively to the wide Fermi surface (circle shape) occurring in overdoped regime. The present of hole and electron pockets possibly inducing the formation SDW or CDW [198] due to the presence of nesting vector followed by reducing the Fermi pockets due to gap formation.

Fermi-surface reconstruction technically means that the Fermi surface represented in reciprocal lattice of copper-oxide plane is represented again in a new reciprocal lattice emerged in material for instance commensurate SDW/CDW. Fig. 1. 18. shows the mechanism of Fermi surface reconstruction due to the presence of antiferromagnetic order. The Fermi surface reconstruction is generated by doping process via the presence of identical hole/electron pockets in Fermi surface. The identical pockets in Fermi surface raise a vector that can translate from one point of Fermi

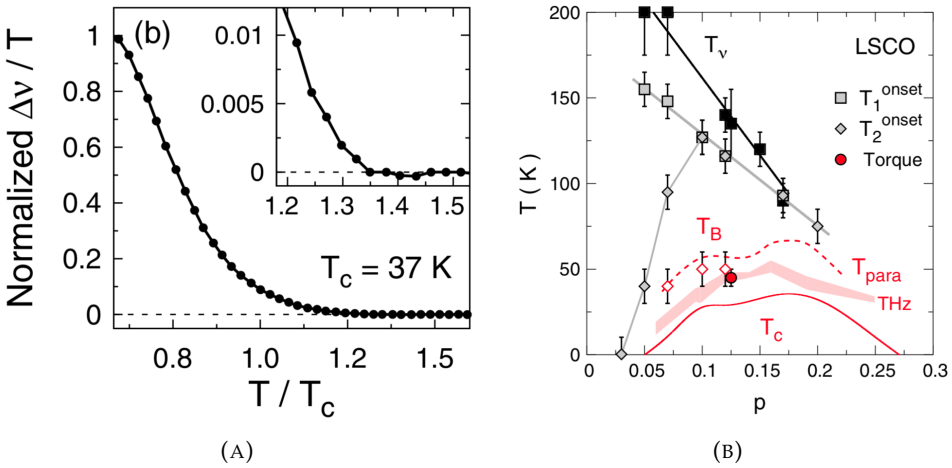

(A) (B)

FIGURE 1.17: The left panel, the Nernst signal for LSCO sample of 15% hole concentration, the signal changed by pseudogap formation. The right panel, the temperatures at which the Nernst signal changed as a function of hole doping concentration [40]

pockets to another point of Fermi pockets called Nesting vector. The points are called hot spots. Since a pattern with a vector in momentum space represents an order in real space, the presence of nesting vector potentially induces the formation SDW or CDW orders. This result then challenge the approach of the strong coupling limit with only hole as carriers. Other Fermi surface reconstruction models observed in transition from strange metal to pseudogap regions also possibly linked to formation of orbital current model [6], or PDW proposed to support the pseudogap state a precursor of superconductivity [42]. Doiron *etal*. [45] indicated the present of Fermi surface with small pockets in YBCO via quantum oscillation experiments. Whereas Laliberte *etal*. [105] reported the evolution of small pockets in YBCO and Eu-LSCO as a function of doping and temperature and addressed the phenomena to the stripe formation. There are some explanations on how Fermi pockets seen in applied magnetic treatment becomes disappears in zero-field ARPES measurement. Besides it is induced by applied magnetic field, the Fermi pockets possibly come from the interplay between CDW and superconductivity [5, 15].

From the specific heat measurement [131] as shown in fig. 1. 19, the ratio heat capacity to temperature of the underdoped LSCO with a various Sr concentrations shows a slight decrease when temperature goes down to T_c. According to RVB theory [113], the decrease is caused by the formation of singlets. This behavior is different from normal metal showing a constant value. Since the ratio is correspond to the Sommerfeld constant, and the Sommerfeld constant is proportional to density of state (DOS) in Fermi surface, then the result from specific heat measurement in which the DOS falls with temperature confirms the gap formation in Fermi surface. The specific measurement also does not thermodynamically indicate a phase transition from bad/strange metal to pseudogap states at T^* temperature because there is no either discontinuity or finite discontinuity in the change of ratio of heat capacity

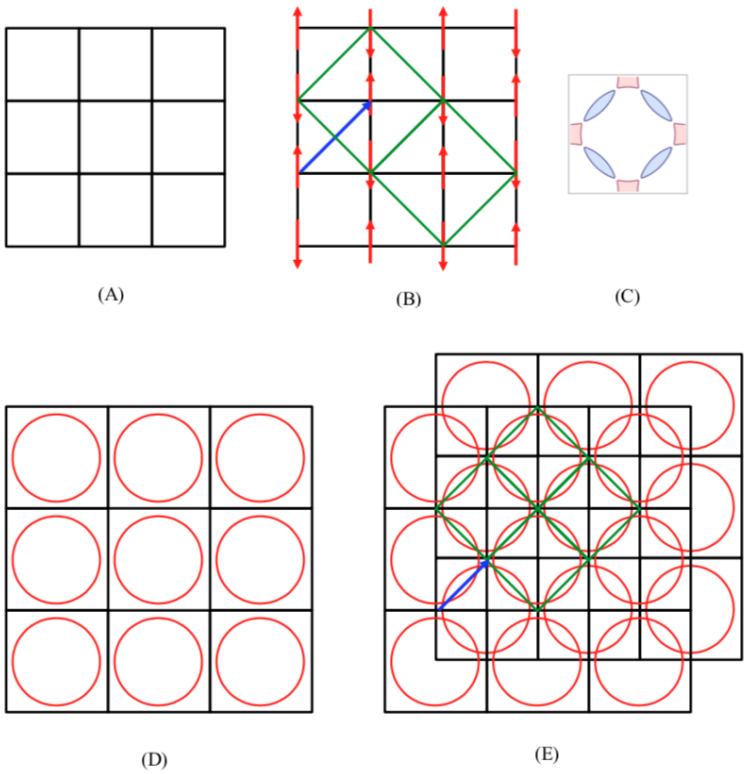

FIGURE 1.18: Fermi surface reconstruction due to the formation of SDW induced by the emergence of electron and hole pockets due to doping process. Panel (A) is the lattice of cooper-oxide plane, and panel (D) is reciprocal lattice of cooper-oxide plane together with two-dimensional Fermi surface with circle shape. Inside circle is occupied by hole and electron occupies the out side of circle. Panel (B) is a commensurate SDW formed on lattice of copper-oxide plane with green diamond being commensurate SDW crystal cell, and the blue arrow represents the vector of commensurate SDW lattice. Panel (E) is reciprocal lattice of SDW lattice with respect to reciprocal lattice of copper-oxide plane, and the green diamond is reciprocal lattice of commensurate SDW. The blue arrow is the reciprocal lattice vector of commensurate SDW. Panel (C), the light blue area is hole pocked formed by the intersection between two circles from panel (E), and outside area of intersection of four circles will form electron pocket.

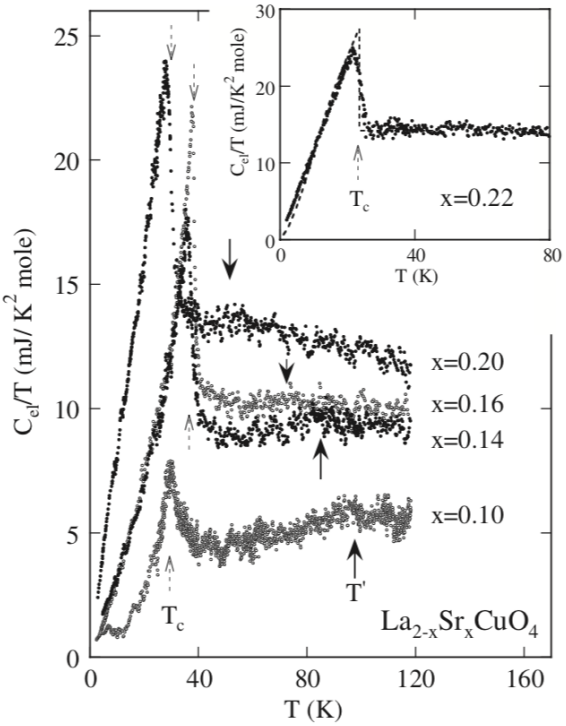

FIGURE 1.19: The ratio of heat capacity to temperature show a dependence on temperature above T_c indicating the change of DOS in Fermi surface [131]

to temperature indicating crossover phenomena instead of a phase transition. The condition of the ratio of the heat capacity to temperature being constant is basically only when temperature close to zero, with that, excluding phonon contribution from the electronic specific heat at a range of pseudogap temperatures is still getting much attention and being no consensus. Some experiments have confirmed the presence of symmetry braking at pseudogap state associated with the phase transition phenomena for instance charge-spin stripe or SDW-CDW breaking translational-rotational symmetry and circulating current loop breaking time-rotational symmetry, but the order parameter thermodynamically cannot categorize the first or the second order transitions at T^* temperature associated with pseudogap formation. The clear thermodynamic evidence for the phase transition with nematic phase transition associated with rotational symmetry breaking was only observed at YBCO via magnetic torque measurement [182].

The gap formation in the normal state of underdoped LSCO marking the presence of pseudogap state is clearly revealed by angle-resolved photoemission spectroscopy (ARPES). The gap value of the normal state is bigger than that of superconducting gap, and its symmetry shown a similarity with the superconducting gap. However, the gap structure exhibits the opening of nodal called Fermi arch depending on doping concentration. The quasiparticle coherence represented by the peak

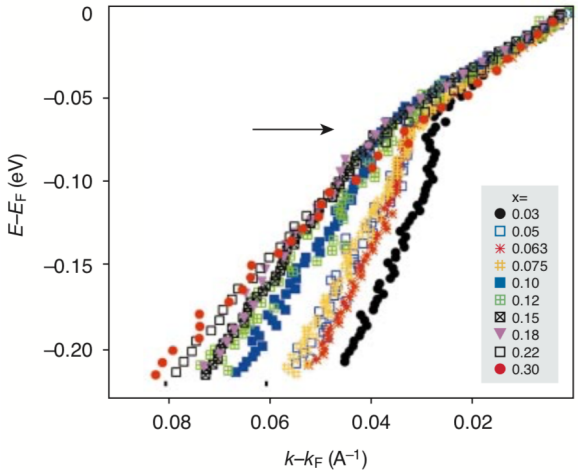

FIGURE 1.20: Dispersion curve (energy as a function of momentum) of LSCO with doping concentration. The black arrow shown universal kink in cuprate materials that can be caused by electron-boson interaction or electron-electron interactions [238].

of momentum dispersion curve (MDC) is well defined at Fermi arch or nodal region, but the quasiparticle is heavily scattered around antinodal region [43]. The MDC width that is proportional to the invers of mean-free path shown doping-concentration and temperature as well as Fermi angle dependence [67].The Fermi velocity at nodal region reveals nearly doping-independent and cuprate-type materials, but it shown strongly doping-dependence at high-energy velocity [238] as shown by Fig. 1. 20. There has been a debate on whether the universal kink at energy around 70 MeV is caused by electron-boson interaction or electron-electron interaction [156]. At Fermi surface of LSCO was also detected the shadow band with weaker spectral weight compared to the main band and performs both a certain symmetry with respect to the main band and Sr doping-concentration-dependence [69, 166].This shadow band has been linked to the Fermi pocket found by quantum oscillation experiment. However there is still a long debate on whether the Fermi pocket exists above the temperature of CDW and become a natural band feature even at high temperature [62], whether the Fermi pocket coexist with Fermi Arch or not [135], whether the Fermi pocket has structural, magnetic or electronic [69], and it is induced by applied magnetic field or not [166]. The left panel of fig 1.21 exhibits both the difference character of normal-state gap and the superconducting gap. Whereas the right panel of the fig. 1. 21 shows the Fermi arch in underdoped regime of LSCO increase with the rise of Sr concentration. It is still a debatable issue in both theoretical approaches and experimental interpretations not only on what is the connection between spin- and charge-gap observed in pseudogap state but also on whether the gaps in normal and superconducting states is the same or not [66].

The magnetism study from neutron scattering experiments on LSCO material in pseudogap state, as others cuprate material, shown a general pattern of dispersion

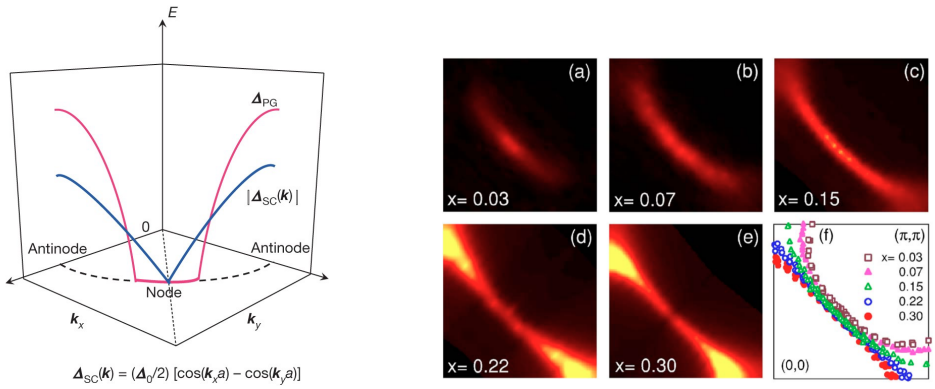

(A) (B)

FIGURE 1.21: The left panel, the different gap structure between normal and superconducting states, the pink line represents the gap at normal state with the opening of nodal point called as Fermi arch; the blue line shows the superconducting gap structure with smaller gap [92]. The right panel shows the Fermi arch in underdoped regime increase with Sr concentration [233]

curve of magnetic excitation known as hour-glass spectrum at which the deviation from antiferromagnetic wave vector decrease with the increase of energy and after reaching a minimum deviation, the deviation increases with energy [128]. The deviation from antiferromagnetic wave vector representing incommensurability in LSCO nonlinearly increases with Sr-doping concentration and saturate at 1/8 Sr-concentration [230]. The incommensurability of the spins structure can be linked to spin spiral and or SDW [201], and it can be interpreted in the framework of both weak-coupling approach with partial nesting of Fermi surface and strong-coupling approach with spin-charge separation [213]. Lee et al. [110], using inelastic neutron scattering techniques with range energy 2 meV $\leq \hbar \leq$ 12 meV, confirmed the spin excitation in LSCO material for 15%, 18% and 20% Sr concentrations. Even though the gap structure is not perfect like spin gap because the dynamic-magnetic susceptibility as a function of frequency is not completely zero at low frequency (energy), or it means that there is still a finite probability to find a spins structure to occupy a range of low energy spectrum, however the probability is small, the trend is decrease to zero. They called the founded gap-like structure as spin pseudogap. Fig 1. 22 shows that spin gap occurs at temperature 8 K due to singlet formation of copper pairs but the gap structure above T_c is not a perfect spin-gap structure. The figure also shows the spin-gap energy at superconducting state as approximately similar with spin pseudogap energy at 36 K and 45 K that is about 5 meV. This result suggests that spin singlet has formed at the pseudogap state indicated by the decreasing of intensity of incommensurate-magnetic order, and the gap structure may change due to phase fluctuation of superconductivity as pseudogap state. Whereas, from another inelastic neutron scattering in LSCO with 8.5% Sr concentration conducted

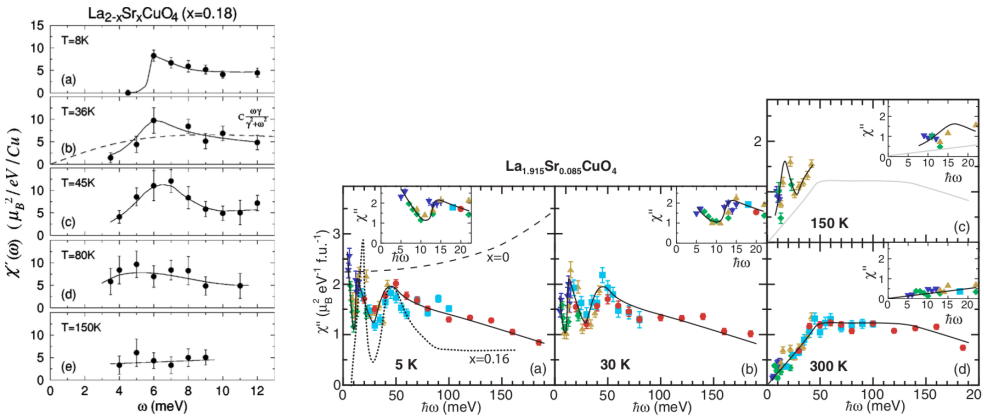

(A) (B)

FIGURE 1.22: The line shows a dependence of dynamic-magnetic susceptibility on frequency (energy), below Tc spin-gap clearly emerge as a singlet of copper pairs, above Tc, gap structure of spin excitation is not perfect spin gap called spin-pseudogap [110]. The dynamic magnetic susceptibility of LSC0 sample with 8.8% Sr concentration as a function of energy at various temperatures (5 K, 30 K, 150 K and 300 K) [118]

by Lipscombe *etal.*, [118], with much wider range of energy and a range of temperature 5 K < T < 300 K, the experiments did not see the spin gap or spin pseudogap, event though the spin excitation presents shown by peaks in dynamic spin susceptibility at higher energy and persists until 150 K shown in Fig. 1. 22. The absence of spin gap in underdoped regime of LSCO also respectively has reported by [83, 70, 111] for 7% Sr concentration, and [186] for 10% Sr concentration.

The presence of resonance in spin excitation marks the appearance of pseudogap. The energy range of which dynamic spin susceptibility changes is $E \geq 70$ meV [118] that is close to energy of charge-gap from ARPES experiment $2\Delta = 51$ meV at the same material (LSCO with 8.5% Sr concentration) [186]. Another inelastic neutron scattering shown a spin excitation that is like spin-wave excitation [130] where the dynamic susceptibility as a function of energy forms Gaussian or Lorentzian shapes. These results then challenge the idea of spin gap of singlet formation as single contribution of magnetism in pseudogap state from RVB theory. In another elastic neutron scattering experiment carried out by Drachuck *etal.* [46] in LSCO with 19.2% Sr concentration shows a commensurate magnetic order starts emerging at 120 K. As in fig 1. 23, when temperature decreases, the change of Neutron-diffraction density of the commensurate magnetic order shows the nodal gap (gapless excitation) below the commensurate magnetic order starting order from 140 K and closed to a temperature at which the incommensurate-magnetic order (SDW) is still founded. The gapless in spin excitation was also reported by Itoh *etal.* [81] occurred in LSCO with 13% Sr concentration from NMR experiment in which, after reaching the peak at 140 K,$1/T_1T$ decrease and turn up again to make the second peak still above T_c, see Fig 1. 23 Meanwhile, using a polarized neutron scattering in LSCO sample with

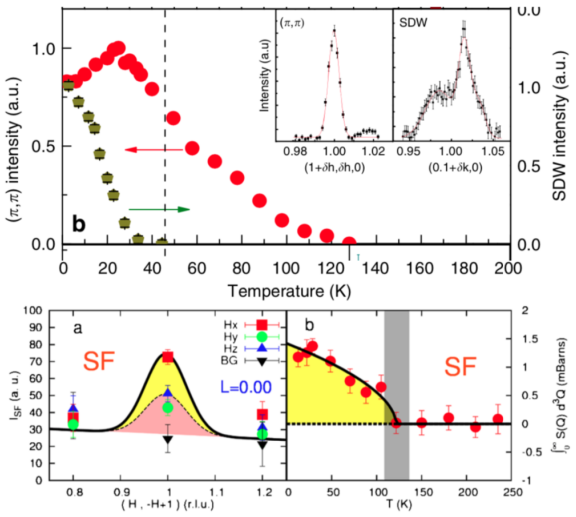

FIGURE 1.23: Above panel, red circles represent a dependence of neutron-diffraction intensity in a temperature range of commensurate-magnetic order observed in LSCO sample with 19.2% Sr concentration, while another pattern is for incommensurate-magnetic order (SDW) that vanish at around 30K. The peak represents the nodal gap in commensurate magnetic order [46]. Bottom panel (LSCO sample with 19.2% Sr concentration) shows the dependence of integrated magnetic intensity on temperature in LSCO sample in spin-flip channel [14]

8.5% Sr concentration, Baledent *etal*. [14], show the magnetic order with a staggered magnetic patter emerged in each unit cell at temperature around 120 K, they then proposed the presence of orbital-current magnetic order [207, 208, 210, 211], even though they provide another explanation scenario based on spin model in line with spin-orbit coupling. This temperature is the same as the temperature of commensurate magnetic order started to be observed in experiment Drachuck *etal*. [46].

Muon spin relaxation/rotation/resonance (μSR) as a sensitive tool to see the static and dynamic behaviors of internal magnetic field of ordered/disordered magnetic systems has been applied to study the magnetism of pseudogap of underdoped LSCO material. MacDouglass *etal*. [123] carrying out zero-field μSR experiment on single crystal LSCO with various Sr concentrations (13%, 19% and 30%) found only distributed internal magnetic field originating from nuclear dipoles sensed by muon spin, see Fig. 1. 4. 13 (left panel). And, the distribution-width of nuclear dipole fields just starts changing around temperature 175 K and addressed to the muon diffusion. The conclusion of muon diffusion is based on another μSR study on YBCO sample [191]. This result then confirmed the absence of exotic magnetic order for instance orbital current models [207, 208, 210, 211, 32] as a new phase. Meanwhile, Watanabe *etal*. [218] carried out zero- and longitudinal field μSR experiment, shows the presence of weak magnetism that induces a tiny changes from Gaussian distribution in polycrystalline LSCO with Sr concentrations (2.4%, 4%, 11.5% and 15%), see

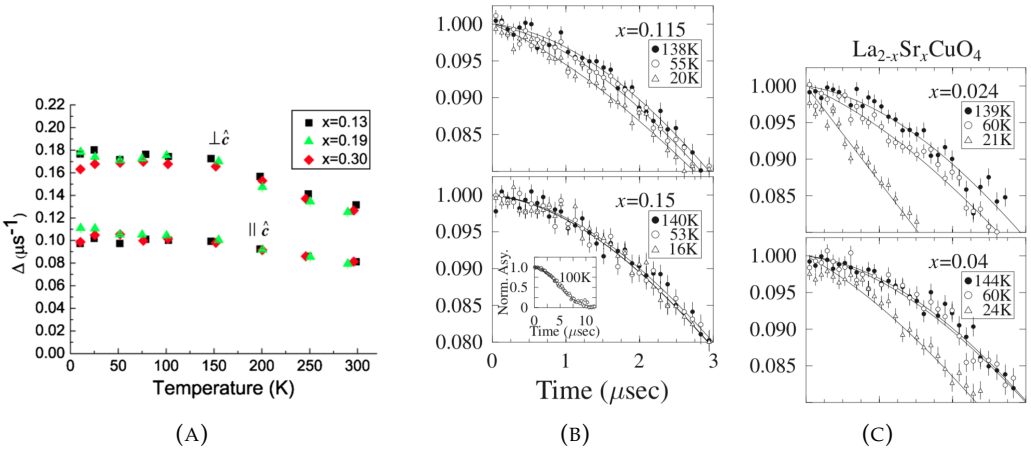

FIGURE 1.24: A. The left panel shows the widths of distribution field of nuclear dipole as a function of temperature [123]. The two right panels show the tiny changes of Gaussian-shape due to pseudogap formation [218].

Fig 1. 14.12 (right panel). In other recent μSR experiments in different cuprate materials, the similar detected weak magnetism has been addressed to the presence of slow dynamic internal magnetic field [153, 236]. Watanabe's result also indicates the spin-charge interplay in which the temperatures of relaxation rate start inclining is in good agreement with temperatures of which hole starts localized earlier found by [199, 11, 101] from the resistivity measurement of metal-to-insulator crossover (MIC) in the normal metal of LSCO under applied magnetic field. Localization temperatures in the pseudogap state located in area in which resistivity is governed by electron-electron interaction suggested by the resistivity dependence of quadratic temperature as presented in Fig 1. 4. 14 [218, 17]. An inelastic neutron scattering also identified Watanabe's result in which a large change of spin excitation through MIC in YBCO reported by Li *etal*. [117]. The tiny changes from Gaussian-shape was also reported by Panagopoulos *etal*. [155] in underdoped LSCO but spin correlations enter the μSR time windows at much lower temperatures than Watanabe's results. Using stretched exponential function to fit μSR time spectra, Panagopoulos fitting results shown fluctuating spins randomly freeze at low temperature and keep still exist until the superconducting state. The spin glass temperature shown the dependence on doping concentration and vanish on about 16% Sr doping concentration. Since the tiny changes from Gaussian-shape can be induced by static or dynamic relaxation, the further investigation is very important to reveal the behavior of static-dynamic magnetic internal field in line with the formation of pseudogap state. The investigation then cannot only discuss theoretical models underlying the magnetism of pseudogap state but also provide constraints for the proposed theoretical models.

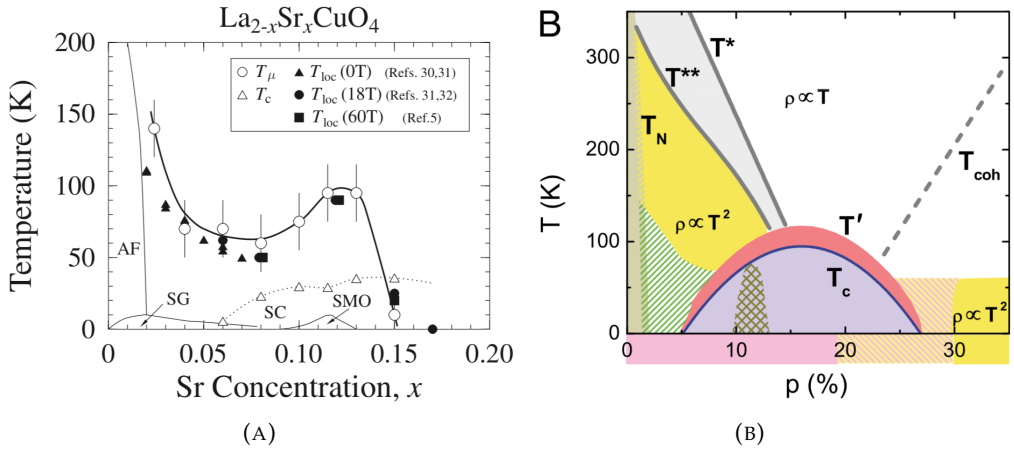

(A) (B)

FIGURE 1.25: Pane (A) black triangle-circle-square shown the temperatures where carriers start to localize in MIC experiments [199, 11, 101] reported earlier than temperatures of which the relaxation rate in μSR time spectra starting to monotonically increase [218]. Panel (B) represents the proposed general phase transition based on resistivity measurement. The T^* is temperature where the gradient of resistivity dependence of temperature start to decrease, T^{**} is temperature where the resistivity dependence of temperature returns to linear [17].

1.5 Theoretical Models on Pseudogap in Cuprate-based Superconductors

The proposed theoretical models underlying the emergence of pseudogap state are generally developed to understand the origin of superconductivity. Thus these models can be categorized based on how they proposed the mechanism of superconductivity. The first model based on Anderson's proposal about RVB state as the ground state of magnetic state of the system. According to RVB theory, charge and spin excitations experimentally observed at pseudogap state directly represent the singlet formation of RVB state with spin gap, and temperatures of singlet formations represent crossover phenomena. In RVB picture, electronic excitation was seen by ARPES experiments represent energy to break the singlet [113]. In the first version of RVB theory, there is no electron/hole Fermi surface since holon and spin may have different gaps, so to accommodate the electron/hole Fermi surface, another model proposed the coupled spinon-holon to create Fermion particle [91]. This alternative model is called Fractionalized Fermi liquid. The popular Hamiltonian based on strong-coupling approximation (U is relatively large compared to kinetic energy) of Hubbard model with RVB state is known as $t-j$ model. In RVB scenario, the superconducting gap and pseudogap are the same gap represented by the spin gap of singlet (one gap model).

Another one gap model proposed that the pseudogap state is superconducting state with phase fluctuation [48]. This model was inspired by Uemura law reporting the superfluid density is proportional to T_c. Since the superfluid density and

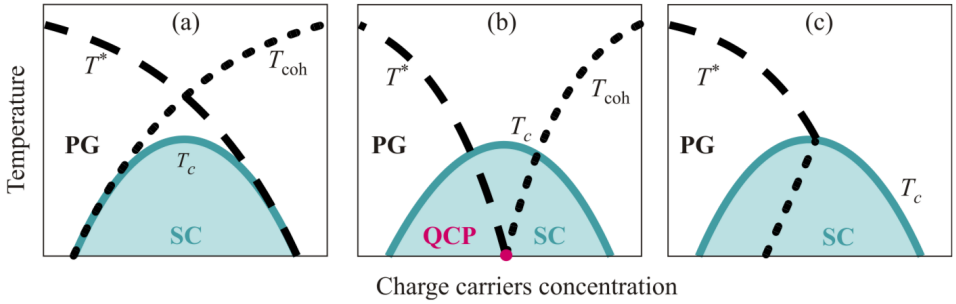

FIGURE 1.26: Schematic phase diagrams are based on different theoretical models. The first panel, pseudogap is as a precursor of superconductivity. The middle panel, pseudogap is induced by the presence of QCP. The right panel, pseudogap as competition among orders [102].

superconducting gap are almost balance and does not vanish at T_c, the Uemura law indicates superconducting gap still present above T_c [152]. In this model, pseudogap state was proposed as superconducting state without coherency because superconductivity emerges just in finite areas with different phase, and the phases fluctuate due to thermal energy. While another interpretation inspired by the detection of PDW in vortex state has theoretically suggested the pseudogap state as PDW without phase coherence [34].

The left panel of Fig. 1. 26 represents the schematic diagram for above two models. Temperature T^* describes the singlet RVB or cooper pair formation, whereas coherence temperature $T_{\mathbf{coh}}$ figures out the superconducting phase becoming coherence or represents temperature of coherent mobile holon in RVB picture. Whereas, according to model proposed by Emery *etal*. [49], T^* temperature describes the crossover phenomena when the inhomogeneous electron gas in the form of stripe or 1-dimensional electron gas and antiferromagnetic correlation with insulating state occurred. It is different from RVB characteristic temperature, in the model of Emery et al. there are two characteristic temperatures related to pseudogap state. Besides T^* marking the stripes are well defined, the second characteristic temperature called T_2^* that is lower than T^* marks the formation of spin gap at spin stripe coinciding with the phase fluctuation of superconductivity state as shown by Fig. 1. 27 The two above models view pseudogap as a precursor state before undergoing a real phase transition to superconducting state. These models are facing challenges from experimental results such as ARPES experiment suggest the two gaps coexist and compete each other [66], and neutron scattering which sees spin gap, resonance spin excitations and spin wave-like in pseudogap state.

In another new version of the RVB theory which adopts pseudogap as phase fluctuation of superconducting state, spinons may move in the same direction and attract each other by magnetic interaction similar like attraction force between two

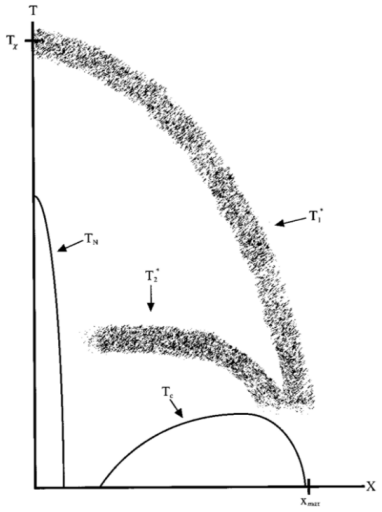

FIGURE 1.27: Schematic phase diagram was proposed by Emery *etal*. [49] due to pseudogap state. T_2^* marks the formation of spin gap at insulating-antiferromagnetic area.

currents flowing in the same direction. Whereas holons will automatically form periodic arrangement corresponding to spinons motion even though the long order of spinon-holon state as PDW will be destroyed by the phase fluctuation [112]. The momentum of spinon-holon state as cooper pair will not be zero like in BCS theory and the mechanism pairing in this model called Amperean pairing [112]. One has proposed the PDW is a state which underlies all states of cuprate phase diagram [112].

The second theoretical models approach the pseudogap as a precursor of orders due to the presence of quantum critical point (QCP) induced by doping. The QCP are suggested by [177, 189, 209, 30] based on experimental interpretations from resistivity, neutron scattering and Hall effect [26, 127, 227]. The idea was started from localization phenomena in metal−to−insulator crossover (MIC) shown by resistivity measurement in underdoped LSCO [26]. To explain the resistivity dependence on temperature in MIC, Castellani *etal*. [31] argued that, besides dynamical stripe, critical fluctuation near QCP might be responsible for localization phenomena in LSCO. Moreover, from a resistivity measurement carried out by Daou *etal*. in material Nd−LSCO [44], they found the resistivity at the suspected Sr concentration as QCP, the linear resistivity is persistent until close to zero under applied magnetic field, whereas for Sr concentration just below QCP, the resistivity show MIC associating with Fermi surface Reconstructions. The result is a normal signature of QCP [120]. Later, Michon *etal*. also reported the divergence of the electronic effective mass and specific heat at doping concentration as a signature of QCP at which the characteristic temperature (T^*) of pseudogap state end [136]. Above zero temperature, the QCP will open, and quantum fluctuation will influence the physical observable driven by Heisenberg uncertainty. The QCP locates around the optimaldoped

and overdoped regimes representing a quantum phase transition between ordered and disordered states at zero temperature. Later a μSR experiment also suggests that MIC linked to magnetic quantum critical point in YBCO and LSCO [193].

The middle panel of fig. 1. 26 represents scenario for theoretical model based on QCP. Disordered systems include two areas, the area of below short dashed line is a disordered system underlying Fermi liquid behavior at which quantum fluctuation weakly effects on the excitation of the ground state, whereas the area between short and long dashed lines is disordered system which is responsible for Non-Fermi liquid behavior [187]. At the second disordered system, the physical properties at high temperature are strongly affected by the quantum fluctuation [187]. Meanwhile, an area below the long dashed line is an ordered state. The quantum fluctuation induced by the QCP will take place on electronic observables affected by doping process for instance spin, charge, orbital and lattice. In the cuprate-based superconductor, quantum criticality was earlier believed relating to the instability of antiferromagnetic order, thus spin will be physical observable that experience quantum fluctuation. However, the identified orders of CDW [38], SDW [155, 100, 214], magnetic order state [14] charge and spin stripes around 12.5% Sr doping, rotational symmetry breaking that provide the possibility of orbital order at pseudogap state, indicating he interplay of spin, charge orbital and lattice due to QCP [173].

In spin-fermion model approaching the middle scheme from metal state, the quantum criticality will induce the fluctuation of antiferromagnetic exchange interaction among spins of the itinerant electrons located in vicinity of intersection between antiferromagnetic-reciprocal lattice and reciprocal lattice. This magnetic scattering process due to spin fluctuation will underlie pseudogap phenomena for instance the change of resistivity behavior and electrons become gapped when the magnetic interaction promote the formation of the onset of SDW [162]. Meanwhile Sokol and Pines [189] proposed that spin wave or a collective magnetic excitation in the background of SDW fluctuation is spin-gap. The temperature marking the spin-gap formation in spin-fermion model for example nearly antiferromagnetic Fermi liquid (NAFL) model is given by Figure 1. 28.

Besides approaching pseudogap from metal state (overdoped doping), other approaches to pseudogap in framework of QCP start from non-doped antiferromagnetic state and consider how the increase of hole-doped changes the magnetic and electronic structures of copper oxide plane. In this approach, the mostly electron localized due to antiferromagnetic, and Fermi surface consists of separated hole pockets [175, 36, 184].

Another quantum criticality is related with CDW order. In this scheme, quantum criticality will induce charge fluctuation, and Coulomb interaction among the fluctuated charge of electron located in vicinity of intersection between CDW$-$ reciprocal lattice and reciprocal lattice will be responsible for pseudogap phenomena. The instability of $d-$orbital of Cu due to quantum criticality also possibly

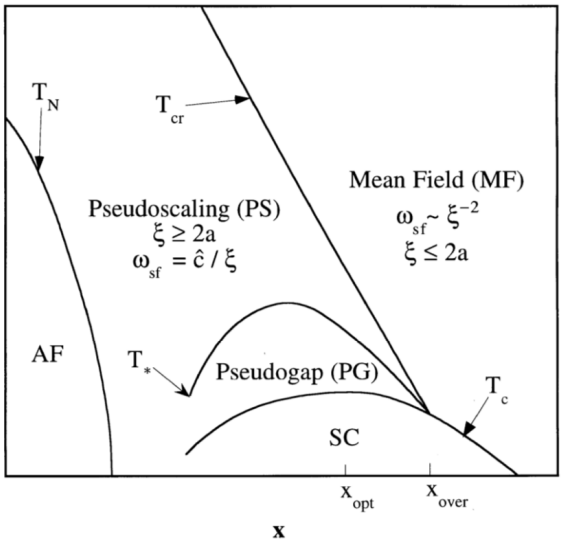

FIGURE 1.28: The phase diagram in NAFL model, T^* is the formation temperature of spin gap [162].

induces the change of orbital arrangement or nematicity behavior shown by emergence of anisotropic in resistivity [227, 182] and magnetic torque experiments [182]. In cuprate Beside SDW and CDW instabilities, other type instabilities proposed for cuprate- based superconductor are currents circulating each plaquette known as $d-$density wave [131] and currents flow among two oxygen planar and copper know as intra unit cell magnetic order [38] as shown in Fig. 1. 5. 4. The two last models have become another debatable issue, since pseudogap is proposed as a new phase and not crossover phenomena.

The right panel of Fig. 1.5.1 represents the phase diagram for emergence of pseudogap phenomena without considering the presence of quantum critical points. Is it different from the emergence of CDW in quantum critical point scheme due to the quantum instability induced by doping via electron-phonon interaction, CDW in the third scenario can be generated by either Fermi surface nesting due to electrons screening to phonon [50] or a competition of antiferromagnetic and coulomb interactions generating spin-charge separation [235]. These order states are in competition with superconductivity. The competition between superconducting state based on BCS theory and CDW induced by spin-phonon interaction has been developed for V_3Si [23].

1.6 Electronic Structure of $La_{2-x}Sr_xCuO_4$ (LSCO)

The cooper-oxide plane is believed being responsible for both the cuprate's magnetism and conducting behavior of which the superconductivity emerge, so the electronic structure of LSCO is generally understood from octahedral shape of Cu in the environment of six-oxygen. The same distance of 2-minus of 6-oxygen ion

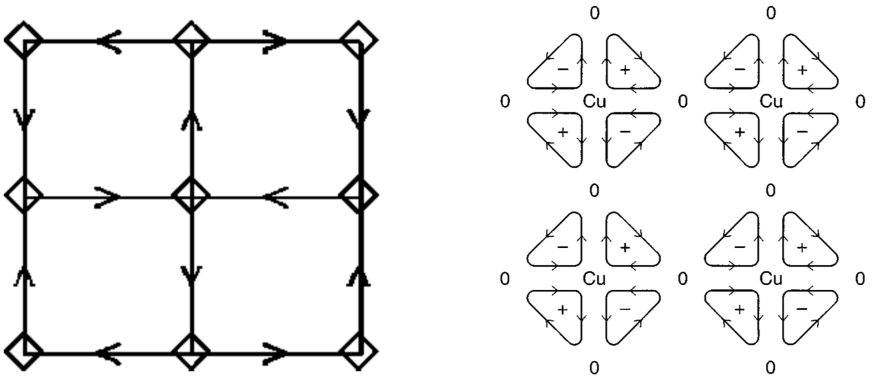

(A) (B)

FIGURE 1.29: Pane (A) The left panel, the model of currents flows among every four Cu atoms (d-density wave) [32], and magnetic moments form antiferromagnetic-like order. The right panel, the model of currents flow among 2 oxygen planar and Cu atom, and staggered moment in every unit cell preserve translational lattice symmetry [207].

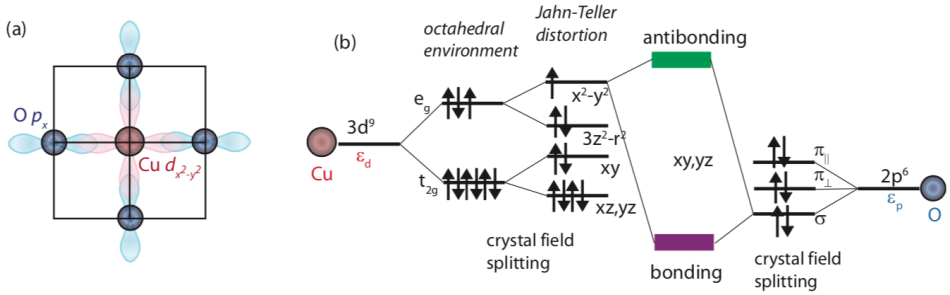

FIGURE 1.30: The panel (a) represents a schematic model of Cu and O orbitals governing the electronic structure of CuO2 plaquette. The panel (b) is a diagram of the energy splitting of d-orbital due crystal field and Jahn-Teller effect, and the hybridization between Cu$-d_{x^2-y^2}$ and O$-p_{x,y}$ orbitals [212].

from Cu ion makes the crystal field of oxygen ions split the degenerate $5d-$orbital Cu ion consisting 9 electron become 2 levels. And, the stretching of apical oxygen in $c-$direction will make the ground state of $d-$orbital energy become lower and split $d-$orbital become 4 level knows as Jahn$-$Teller effect. The $p-$ orbitals energy also splits due to the crystal field at which the $p-$orbital in sigma$-$configuration with respect to Cu ions will have the lowest energy or strong coulomb interaction followed by parallel and perpendicular phi$-$configuration respectively. In the tight$-$binding model, the Cu$-d_{x^2-y^2}$ and O$-p_{x,y}$ orbitals will hybridize to make bonding and anti$-$bonding states in which a single particle in anti$-$bonding state will across Fermi energy and predicts the parent compound of La_2CuO_4 must be metal, this mechanism is modeled by Fig. 2. 1 [212]. The last possible arrangement of $d-$ and $p-$orbital will produce non-bonding as show in Fig. 2. 2.

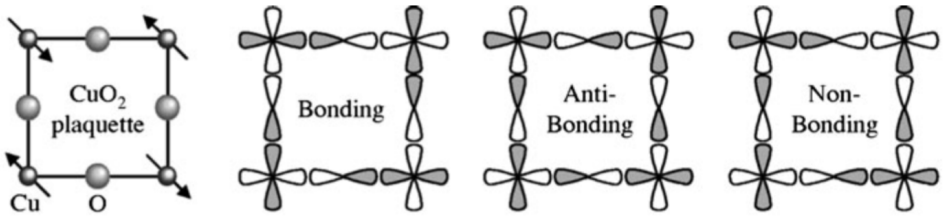

FIGURE 1.31: The orbital ordering (the sign orbital wave function) correspond to bonding, anti-bonding and non-bonding states [164].

There are two models to understand the insulating behavior of LSCO that are weak− and strong−coupling models. In a strong−coupling limit, the strong onsite Coulomb interaction in Cu$-d_{x^2-y^2}$ orbital occupying the Fermi level is commonly believed being responsible generating the antiferromagnetic insulating behavior [113], whereas another believed the antiferromagnetic originates from nesting of the Fermi surface induce the charge-gap known as Slater-insulator [89, 1]. The latter is when the Coulomb repulsion is small compared to kinetic hopping energy. The two previous approaches are partially supported by DFT calculation producing antiferromagnetic-insulator band with [220, 41] or without including Hubbard potential [197, 195, 106]. In effective model, strong- and weak-coupling approaches mostly assume the cuprate physics is governed by one band / component model. Meanwhile in two-phase or two-component model suggests that electron Cu$-d_{x^2-y^2}$ orbital will be in insulating state for instance caused by the interaction of the electron with negative ions lattice as polaron, and Fermi energy or chemical potential is pinned to the vicinity of polaron state [61], whereas hole at $p-$orbital oxygen sites will produce conducting state where Fermi surface will be determined by the interaction between magnetic-insulating background and conducting electrons.

The model of doping state in LSCO material also is debatable issue. In the beginning development of RVB theory for cuprate−material with one-band model supported by ARPES measurements [185, 7, 43, 221], the antibonding state is mostly dominated by $d-$orbital character and bonding state is dominated by $p-$orbital. When hole is introduced to copper−oxide plane, according to P. W. Anderson, the hole will take place in Cu site and make Cu^{2+} become Cu^{3+}. But, since the experiment results clarified that the hole takes place in O site, one−band model is still persistent by introducing the Zhang−Rice singlet. Another model like $d-p$ model, assumes that there is no singlet coupling between Cu and O spins, but this model proposes the hybridization of upper Hubbard band and $p-$orbital will provide the hopping mechanism between O and Cu sites accompanied by magnetic interaction between spin hole and antiferromagnetic background of localized Cu spins [47]. In Mott insulating picture, the onsite Coulomb interaction parameterized by Hubbard value (U) will split anti-bonding state into the upper Hubbard band (UHB) and lower Hubbard band (LHB) as shown in Fig. 2. 3. The Hubbard value will compete with the energy to transfer electron from ion oxygen to Cu metal as charge transfer

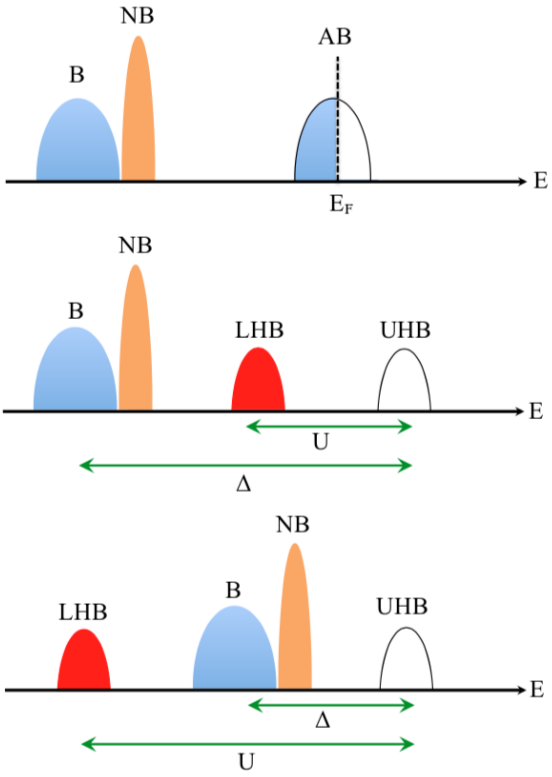

FIGURE 1.32: Density of state (DOS) for Cooper-oxide plane without the consideration of the onsite Coulomb interaction (top panel), DOS charge transfer gap is bigger than Hubbard potential (middle panel). Hubbard potential is bigger than charge transfer gap (Bottom panel).

gap (Δ) in governing electron transport in LCO, see panel (a) of Fig. 2. 3. The charge transfer gap is determined by the difference of $p-$ and $d-$orbital energies. When Hubbard potential (U) is smaller than charge transfer gap (Δ), the charge transport will be governed by Mott−Hubbard model as shown by the middle schematic of fig. 2.3. Whereas, when Hubbard potential is bigger than charge transfer gap (Δ), the charge transport will follow charge−transfer (CT) regime, see the bottom schematic of fig. 2.3.

There are two proposals on how the Fermi energy emerges with doping process. According to first mechanism, the Fermi energy is still pinned in between charge transfer gap and the doping process will shift the UHB and bonding state to occupy energy Fermi. Meanwhile, in the second possible mechanism, Fermi energy will be shifted into valence state, and the UHB state will be transferred to Fermi energy.

The studies of electronic structure of LSCO by using first principle calculations also provide different results. From Physics point of view with an extended-hole model represented by Bloch wavefunction, the Sr-doping process will introduce hole in the Cooper-oxide plane [234, 132, 161]. Whereas from chemist viewpoint using localized-hole model represented by molecular orbital, the hole will prefer take place around the hybridization between P_z and d_{z^2} orbitals [160, 159]. The different picture

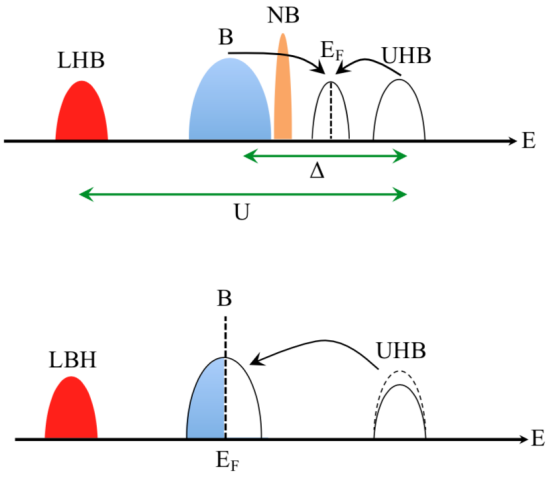

FIGURE 1.33: The reconstruction of Fermi level due to the doping process, the above panel is when the Fermi energy is pinned between bonding and UHB states, while The bottom panel represents the shiftiness of Fermi energy to bonding state due to the doping process.

then induces the different physics mechanism underlying superconductivity.

1.7 λ-$(BETS)_2 GaCl_4$

λ-$(BETS)_2 GaCl_4$, where BETS is bis(ethylenedithio)tetrasenafulvalene), is an organic conductor which exhibits superconductivity below 5.5 K. This material is quasi-two-dimensional system consisting of BETS molecules stacking along a-direction and $GaCl_4^{-1}$ tetrahedral counter anion layers as shown by Fig. 1.34. The two layers are decomposed by a triclinic unit cell with space group $P\bar{1}$ [3]. The BETS molecules donate electric charge and $GaCl_4$ accepts the electric charge [37]. Since two BETS molecules transfer one electron to the acceptor ($GaCl_4$), so there is 1/2 hole per BETS molecule, or HUMO band will be 3/4 filled [72]. The electron transport between donor (BETS) molecular takes place via $\pi - \pi$ interaction, whereas $GaCl_4^{-1}$ with a closed cell forms insulating layers [139].

There are four BETS molecules in unit cell which make four bands present near to Fermi surface. Overlapping wavefunction of I* and II as well as II* and I BETS molecules with large transfer integral due to the shortest distance between two BETS molecules ($\sim$ 1.2 Å), see Fig.1.34, will result dimers, so the electronic structure of this material can be also approached by two-band model. Two bands crossing Fermi energy form an open and a closed Fermi (Fermi pockets) surfaces as shown by Fig. 1.36 [200]. The calculation suggests the size of the closed Fermi surface occupies 28% of Brillouin zone which is proportional to hole density, however the Shubnikov-de Haas experiment estimates each pocket is only 16% of the Brillouin zone [137]. The formation of two Fermi surfaces can be understood by folded Brillouin zone from a

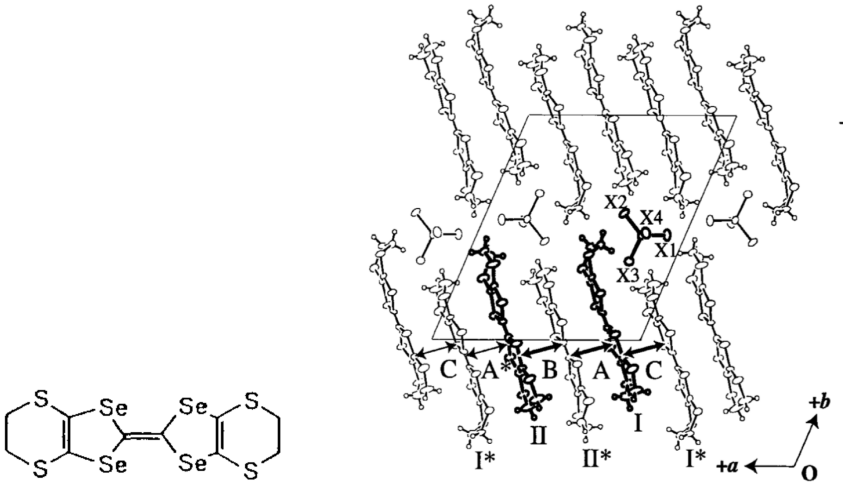

(A) (B)

FIGURE 1.34: The left panel (A) is the chemical structure of BETS molecule decomposed by S, Se, C and H elements [97]. The right panel (B) is Crystal structure of λ-$(BETS)_2GaCl_4$ [200]

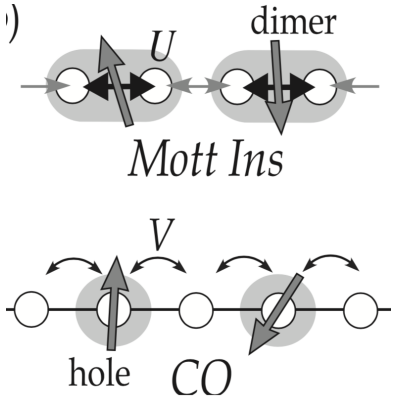

FIGURE 1.35: Schematic mechanism of MOTT insulating and charge order state at λ-$(BETS)_2GaCl_4$ [72]

unit cell of single dimer (or a partial filled BETS molecule) into a unit crystal with 2 dimers (or two partial-filled BETS molecules), and disconnection points between two Fermi surfaces caused by intermolecular interaction inducing the molecular orbital mixing [172]. The phase diagram as a function of both pressure or bandwidth (donor molecules) and temperature suggest delocalization increases with the enhancement of bandwidth indicating the antiferromagnetic state at low bandwidth may be underlined by microscopic Mott-Hubbard model with Hubbard potential (U) at each dimer as shown Fig. 1.35. Furthermore, the potential Coulomb (V) between BETS molecules can be included in order to understand the charge order state in this material [72], see Fig. 135.

λ-$(BETS)_2GaCl_4$ is type-II superconductor with lower critical field H_{c1} being 8(1) G for applied field perpendicular to conducting layer [181] where the polar

angle dependence of interlayer resistance shown vortex dynamics for all direction [232]. The heat capacity measurement below T_c temperature shown T^2 dependence of electronic component which indicates the presence of nodal in superconducting gap [77]. However there is no consensus about the symmetry-type of superconducting gap. NMR experiment shown cubic temperature dependence of spin-lattice relaxation rate $1/T_1$ below T_c without coherence peak indicating d-symmetry of superconducting gap [98]. The ^{13}C NMR measurement also observed the enhancement of the spin-lattice relaxation divided by temperature $1/T_1T$ with the decrease of temperature starting from 10K which indicates the fluctuation of SDW plays role in pairing mechanism [98]. The d-wave superconductivity was earlier proposed by heat capacity experiment at low-temperature [77], but magnetic-field-angle-resolved heat capacity later observed twofold and fourfold-type anisotropy superconducting gap that may not be simply interpreted in the scheme of d-type superconducting gap [76]. The observed anisotropy SC gap was then proposed to be caused by the mix of anisotropy of Fermi surface (low-symmetry λ-type lattice) and antiferromagnetic spin fluctuation [76]. Whereas transverse field μSR experiment shown the superconducting gap symmetry can be well plotted by either mixing s- and d-wave SC gaps or h-wave SC gap represented by hyperbolic tangent function [179]. Since the mixing s- and d-wave SC gap in upper limit of background error give dominant s-type superconducting gap and vanishes nodal in the SC gap, resulting anisotropy d-like SC gap without nodal, author then proposed h-symmetry SC gap which have narrower nodal line and flatter part of maximum gaps [179]. The h-type SC gap was proposed to be underlined by anisotropy of spin fluctuations which may originate from the presence of triangular and squared sublattice on conducting layers [179]. Furthermore paired electrons due to spin fluctuation in different sublattices were then suggested to entangle each other to create exotic paired electrons state at higher dimension [179]. Unconventional superconducting state of λ-$(BETS)_2GaCl_4$ was also indicated by the measurement of time-resolved reflectivity changes which show the amplitude of coherent phonon does not experience an anomaly around the superconducting transition [147].

The magnetism of metal electron in λ-$(BETS)_2GaCl_4$ did not perform Korringa low where $1/T_1T$ from NMR experiments will be temperature independent indicating this material is not simple metal. The NMR study observed the growth of antiferromagnetic correlation in the form of Curie-Weiss dependence of $1/TT_1$ when temperature decrease and reach a maximum correlation around 50 K, and after decreasing below 50 K, the $1/TT_1$ increases again below 10 K which is suggested to be underlined by the development of SDW state, see Fig. 1.37. [98]. Above 150 K, the $1/TT_1$ is mainly contributed by electric-gradient fluctuations which originate from molecular dynamics [99]. While ZF-μSR experiment with time window between neutron- and NMR-spectroscopic only saw the local static fields within a temperature range between 1.5 K and 63 K shown by the temperature-independence of μSR

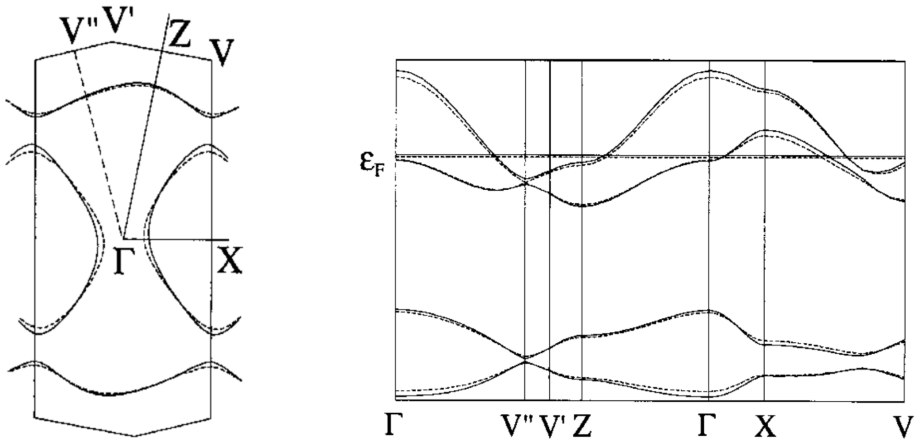

(A) (B)

FIGURE 1.36: The left panel (A) show the band structure of λ-$(BETS)_2 GaCl_4$ from tight-binding model, and The right panel [200] (B) is Fermi surface of λ-$(BETS)_2 GaCl_4$ which cross the Fermi energy [200]

time spectra as shown in Fig. 1.38 [180]. The fitting results using stretched exponential function did not observe time reversal symmetry breaking associating with presence of spontaneous magnetism, and stretching parameter was found smaller than 1 indicating the non-homogeneity fluctuation rate. Even though suggested dynamic behavior from stretched exponential function cannot be supported by temperature independence of μSR time spectra. The initial relaxation of μSR time spectra is between Gaussian- and Lorentzian-shape indicated the dense and static randomly alignment of nuclear moments cannot be single contribution of internal fields on muon sites. Furthermore, the highly anisotropy of Gaussian local fields due to low-symmetry crystal structure of λ-$(BETS)_2 GaCl_4$ does not change the initial Gaussian-character according to a previous theoretical report, and only changing the relaxation rate as well as the shape and location of minimum dip of isotropic Gaussian field [51].

1.8 Previous models of internal field for intermediate relaxation between Gaussian- and Lorentzian-character

Initial intermediate μSR time spectra reflects properties of local random fields experienced by polarized muon spins. In general, intermediate relaxation can originate from the coexistence of dynamic and static fields on muon site or purely dynamic- or static-field effects respectively.

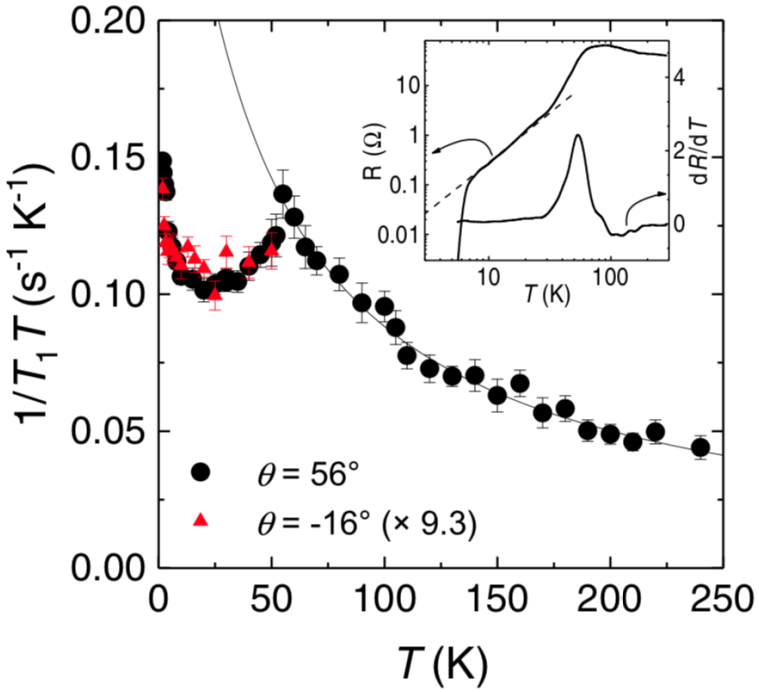

FIGURE 1.37: $1/T_1T$ as a function temperature for direction of applied field being perpendicular to the conducting plane [98]

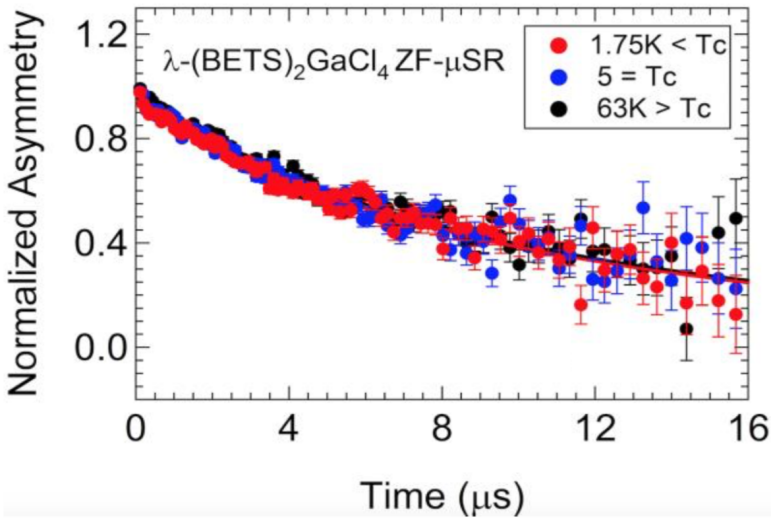

FIGURE 1.38: ZF-μSR time spectra of λ-$(BETS)_2\,GaCl_4$ at 3-different temperature [180]

1.8.1 The coexistence of dynamic and static fields

The magnetic field on each muon site can be decomposed into different contribution of magnetic field sources for example nuclear and electronic magnetic moments. Nuclear dipole moments are quasi static and temperature-independent in μSR time window, so when dynamic fields for example coming from electronic moments are too fast with respect to nuclear moment dynamics, we can separate electronic- and nuclear-moment variables likely Born-Oppenheimer approximation. The dense of static randomly alignment of nuclear magnetic moments will generate static Gaussian field on muon site [103], and muon spin relaxation function reflecting the average of projection of muon spins into initial muon spin direction with respect to Gaussian random fields will be represented by Gaussian Kubo-Toyabe functions [103]

$$P_{GKT}(t) = \frac{1}{3} + \frac{2}{3}\left(1 - \Delta^2 t^2\right) \exp\left(-\frac{\Delta^2 t^2}{2}\right). \tag{1.5}$$

Dynamic electronic moments will generate fluctuation of local fields on muon site. Assuming the dynamic fields evolve from the static Gaussian fields as initial condition, and the random field fluctuation obeys strong collision model, the muon spin depolarization function will be represented by a formula known as dynamic Gaussian Kubo-Toyabe function [68]. In a fast fluctuation regime, the dynamic lineshapes will experience narrowing effect following an exponential relaxation

$$D_{GKT}(t) = \exp(-\lambda t), \tag{1.6}$$

with $\lambda = 2\Delta_e^2/\nu$. Δ_e and ν are distribution width of electronic Gaussian field and field fluctuation rate, respectively. The muon spin relaxation function due to the presence of fast dynamic and static fields on muon site then can be approximated phenomenologically by

$$G(t) = \exp(-\lambda t)\, P_{GKT}(t). \tag{1.7}$$

In fast fluctuation limit, an applied external field will make muon spins see narrower distribution of internal field. For LF-experiment set up in constant temperature or the fluctuation rate $(\nu = 1/\tau_c)$ of field does not change, the applied external field B_0 $(\omega_0 = \gamma_\mu B_0)$ will change the relaxation rate (λ_{LF}) in Eq. 1.7, for LF-condition written as $G^{LF}(t) = \exp\left(-\lambda^{LF} t\right) P_{GKT}^{LF}(t; B_0)$, following a relation called Redfield function [68]

$$\lambda^{LF} = \frac{2\omega^2 \tau_c}{1 + \omega_0^2 \tau_c^2}. \tag{1.8}$$

The redfield function is a lorentzian function with half width at half maximum (HWHM) equal to $\left(\tau_c \gamma_\mu\right)^{-1}$.

The Eq. 1.7 has been applied to approach μSR time spectra of some doped cuprate-based high temperature superconductors to investigate magnetic transition from the evolution of copper spins state in temperature [218, 191, 192]. And, the

redfield function is used to justify whether the relaxation rate in Eq. 1.7 represents the dynamic or static parameters of the internal field. But, the redfield function only represents dynamic Gaussian-type distribution of local field, so it is not generally applicable to differentiate static or dynamic internal fields.

1.8.2 Dynamic local field

Eq. 1.6 represents the random local fields fluctuate with the same fluctuation rate or single fluctuation rate. When internal fields fluctuate with different fluctuation rates, muon spin relaxation function will be represented by stretched exponential function [84, 29, 154].

$$G(t) = \exp(-\lambda t)^{\beta}. \tag{1.9}$$

with $0 < \beta < 1$. Writing a distribution of fluctuation rate as $P(\lambda)$, the Eq. (1.9) can be described by

$$G(t) = \int_0^{\infty} P(\lambda) \exp(-\lambda t) = \exp(-\lambda t)^{\beta}. \tag{1.10}$$

The stretched exponential well approaches μSR time spectra of spin glass system with stretched parameter value tending to be $1/2$ [163], and it has been usually used to study the homogeneity or the uniformity of the sample. Furthermore the stretched exponential can also approache intermediate μSR time spectra in between Gaussian- and Lorentzian-shape with stretching parameter value $1 < \beta < 2$ before going to a condition $0 < \beta < 1$ as reported in previous studies[155, 57, 169]. However the dependence of β and λ parameters for $1 < \beta < 2$ in temperature has not had any established physical interpretation.

1.8.3 Static local field

The intermediate static line shapes can be also obtained from modifying Gaussian and Lorentzian Kubo-Toyabe function in the form [39, 204]

$$P_{SKT}(t) = \frac{1}{3} + \frac{2}{3}\left(1 - (\lambda t)^{\beta}\right) \exp\left(-\frac{(\lambda t)^{\beta}}{\beta}\right). \tag{1.11}$$

This function have both intermediate initial lineshape and a dip in between Gaussian and Lorentzian Kubo-Toyabe functions, and its tail also saturates at the same location as both functions. In general, there has been no any acceptable proof that show a specific condition of random magnetic dipole moments to generate intermediate distribution character of local field associated with stretched Kubo-Toyabe function. Random dipole magnetic moments in between dilute and dense concentration has been proposed to underlay the intermediate distribution character of local field [204], but it has not been still generally accepted.

1.9 Problems and Purposes

1.9.1 Problems

The μSR time spectra of $La_{2-x}Sr_xCuO_4$ and λ-$(BETS)_2\,GaCl_4$ shown intermediate relaxation in between Gaussian and Lorentzian-shapes. In the $La_{2-x}Sr_xCuO_4$ (x=2.4%) case, the changes from Gaussian to Lorentzian relaxations takes place when temperature decrease close to a transition temperature associated with spin glass or SDW states. While the intermediate character of relaxation in λ-$(BETS)_2\,GaCl_4$ exhibited temperature-independent which indicates muon spins only sense static random field, and the random local field is weak indicated by the absence of a Kubo-Toyabe dip.

A key issue to apply μSR in order to understand electronic properties is how to choose appropriate functions to analyze μSR time spectra. The intermediate relaxation may be approached by different functions where it may have different origin as shown in 1.8, so it will work under specific circumstances. Attributed assumptions make some functions for instance both a product of exponential and Gaussian Kubo-Toyabe functions and a stretched exponential/Kubo-Toyabe function may be not appropriate to be used to reveal real features of static and dynamic properties of electronic state. Furthermore there is no appropriate general analysis function existing until now.

1.9.2 Purposes

1. Develop analysis functions of μSR time spectra in case of that the muon depolarizes in random static magnetic fields which have intermediate states in between the Gaussian and Lorentzian distributions.

2. Deliver responses of the intermediate analysis function against applied magnetic fields along the initial muon-spin polarization and dynamic fluctuations of internal fields at the muon site.

3. Approach the μSR time spectra of $La_{2-x}Sr_xCuO_4$ and λ-$(BETS)_2\,GaCl_4$ with developed functions and discuss the origin of the intermediate state.

Chapter 2

μSR Technique

2.1 Muon Properties and Principles of μSR

In a μSR experiment, polarized muons are implanted in to material, and internal magnetic field at muon site will depolarize the muon spins. The internal field at muon site generally is a magnetic vector of summation of all contributed magnetic field that is

$$\vec{B}_{\mathbf{tot}} = \vec{B}_0 + \vec{B}_{\mathbf{dip}} + \vec{B}_{\mathbf{hyper}} + \vec{B}_{\mathbf{RKKY}} + \vec{B}_{\mathbf{dia}}, \tag{2.1}$$

with $\vec{B}_0$ is an applied external field, $\vec{B}_{\mathbf{dip}}$ is dipole field from electronic or magnetic moments, $\vec{B}_{\mathbf{hyper}}$ is the transferred hyperfine field due to the presence of spin density at muon site,$\vec{B}_{\mathbf{RKKY}}$ is the transferred hyperfine field due to a coupling between muon and electronic spins mediated by conduction electron, and $\vec{B}_{\mathbf{dia}}$ is diamagnetic field coming from screening current at superconducting state. The polarized muons are naturally governed by the parity-violating weak interaction theoretically predicted by Lee and Yang [114], and Wu *etal*. [226] experimentally confirmed the hypothesis by Lee and Yang observing the asymmetric beta decay of ^{60}Co nuclei. spin-polarized The first non-conservation of parity takes place in the decay of pion into muon and antineutrino.

$$\pi \rightarrow \mu\bar{\nu} \tag{2.2}$$

The parity of meson that included pion is -1, since muon as lepton particle and antineutrino have the same parity $(+1)$, then the parity of left and right sides of Eq. (2.2) will be different. This non$-$conservative parity makes muons become polarized along the muon momentum axis [64]. The second non$-$conservation of parity is in the decay of muon

$$\pi \rightarrow e\nu\bar{\nu} \tag{2.3}$$

Since the parity of electron/positron and muon $(+/-)$ is the same, and the parity of neutrino and antineutrino are $+1$ and -1 respectively, then the parity between two sides of Eq. (2.3) will be also different. The second non$-$conservative of parity causes electrons be emitted anisotropically about the muon polarization axis [64].

TABLE 2.1: The properties of muon, μ_B is the Bohr magneton

Property	**Value**
Mass (m)	1.8835×10^{-28} KG
Charge (q)	$+1.602\times 10^{-19}$ C
Spin (S)	$1/2$
Magnetic Moment(μ)	0.004 $\mu_{\mathbf{B}}$
Gyromagnetic ratio (τ)	8.51616×10^4 rad s^{-1} G^{-1}
Mean life time (τ)	2.197 μs

Garwin *etal*. [60] then performed that the translational momentum of positrons from the decay of muon is prefentially along the direction of polarized-muons and being considered as first muon-spin relaxation experiments. In the two above decay processes must obey the conservation of baryon and lepton numbers.

Muons are categorized as charges leptons and have the same family as electrons with lifetime being 2.2 μs. The matter (π^+) and antimatter (π^-) of muons belong to positive and negative electron charges, and their mass is 200 times heavier than electron mass make their gyromagnetic ratio exceed other source of probes such as electron and neutron and become very sensitive to magnetic fields. The table 2. 2. 1 summary the properties of muons.

Muons at a μSR experiment are resulted by pions decay. The pions is created by high energy accelerated protons which collide a graphite and produce spin$-$zero pions where the collision obeys the charge conservation as

$$\begin{aligned} p + p &\rightarrow p + n + \pi^+ \\ p + n &\rightarrow p + p + \pi^- \end{aligned} \tag{2.4}$$

The pions will decay into muon and neutrino, and because the pions are spinless and the spin and linear momentum of neutrinos are antiparallel, so at a rest frame, according to the conservation of linear and angular momenta, the momentum of muon and neutrino will be same but with opposite direction. To deliver muons to targeted sample, dipole and quadrupole magnets are applied to control muons. During interacting with electric fields, only muon momentum changed since muon spin does not couple to electric fields. Inside targeted material, the muons will experience scattering process, generate ionization and capture and release electron in interval time between $10^{-10}-10^{-9}$, and finally diffuse or tunnel in local electronic potential and localize at muon sites. During this thermalization process, muons will be still almost 100% polarized.

Muons will undergo decay into positron, electron-neutrino and muon-antineutrino following a reaction:

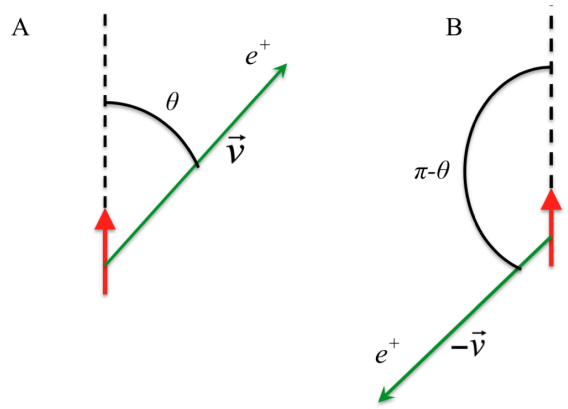

FIGURE 2.1: The illustration of the parity violation in the decay of a muon.

$$\mu^+ \rightarrow e^+ + v_e + \bar{v}_\mu \tag{2.5}$$

The angular probability to find positron in any direction at angle θ and energy ϵ is proportional to due to the second no-conservation of parity in the decay of muons

$$W(\epsilon, \theta) \propto 1 + a(\epsilon) \cos\theta \tag{2.6}$$

The illustration of broken parity symmetry is given by following picture. The red vector represents the muon spin, and e^+ is a positron with velocity $\bar{v}$. Spin is an "axial" vector, so it does not change under parity $\vec{S} \rightarrow -\vec{S}$, while the velocity is a "polar" vector, so it will change under parity action $\vec{v} \rightarrow -\vec{v}$. The panel B of Fig. 2. 5 is the process the decay of a positive muon under parity causing the angular probability will be

$$W(\epsilon, \theta) \propto 1 + a(\epsilon) \cos(\pi - \theta) = 1 - a(\epsilon) \cos(\theta) \neq 1 + a(\epsilon) \cos(\theta) \tag{2.7}$$

with $a(\epsilon)$ is the asymmetry parameter. Fig. 2. 6 shows the distribution function of energy and asymmetry parameter as a function of energy.

The μSR experiment experiment can be done with or without applied external fields, and detectors will monitor the time evolution of muon spins. To monitor the time evolution of muon spin relaxating in dynamic/static internal magnetic field, the forward and backward detectors are installed to record the number of positrons as a function of angle and time. In material, due to the internal field, the $\cos\theta$ in Eq. (2.7) will be time-dependent known as muon spin depolarization function. The number of positron as a function of time in the forward and backward detectors will depend on muon depolarization function and the decay rate following a relation $N_{\mathbf{F,B}} = N_0 \exp(-t/\tau_\mu)[1 \pm a_0 P_z(t)]$, so the muon depolarization function can be extracted from above equation:

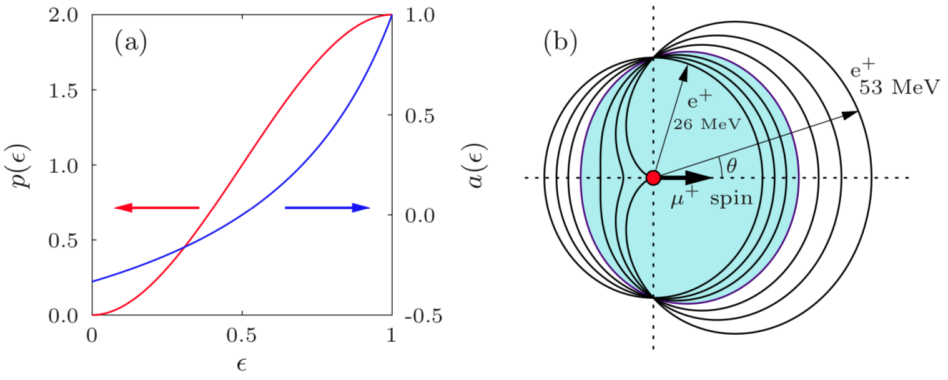

FIGURE 2.2: The probability function of energy (left panel). Asymmetry parameter as function of energy (right panel)[224].

$$a_0 P_z(t) = \frac{N_{\mathbf{F}}(t) - N_{\mathbf{B}}(t)}{N_{\mathbf{F}}(t) - N_{\mathbf{B}}(t)}, \tag{2.8}$$

with $P_z(t)$ is muon depolarization function or muon polarization/relaxation function.

2.1.1 Experimental setups

μSR experimental setup consists of the muon beamline, a detector system (spectrometer) to detect coming muon and or its correlated positron, the presence of applied field to conduct Knight-shift experiment and to perform Vortex behavior in superconducting state, and a sample place with temperature arranger. The muon beamlines can be sent into a sample in the from of a continuous- and pulsed-beams. In the case of continuous beamline, the detection of coming muon by the first spectrometer and the correlated positron by the second spectrometer are called an event, and the process of events counting is arranged in a such away so only one event in μSR time window. The forward- and backward-detector to detect the positrons are located around 2 cm from the sample. The time resolution for the continuous beamline originate from the limitation of detector and electronics in order of 50 ps, so the continuous beam can detect internal fields up to 600 MHz associating with the period of Larmor precession around 1 ns. In μSR experiment with pulsed beamlines, the time resolution in the same order as the Gaussian pulse width of muons with HWHM 80 ns, and the distance between muon pulse is 20 ms. The number of muons in every pulse of beam are the order of thousand muons, and the muons number enhance the probability of muons experiencing longer lifetime. It make a time window of pulsed muon beamlines expand more than 20μs.

The are two-type of μSR measurement geometries that are zero-field (ZF) or Longitudinal-field (LF) techniques and transverse-field (TF) technique. In ZF-experiment, there is no external field applied to sample, so implanted muons only depolarized in internal field of the sample. The direction of muon spins is anti-parallel to muon

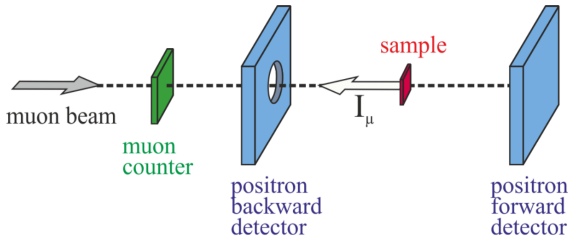

FIGURE 2.3: The schematic illustration of ZF μSR geometry. The forward- and backward-detector located around 2 cm from the sample. [231]

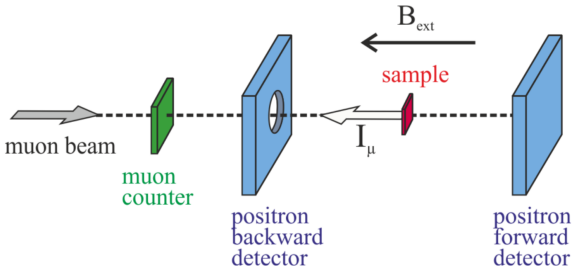

FIGURE 2.4: The schematic illustration of LF μSR geometry. $\vec{B}_{ext}$ is an applied field [231]

beam direction as shown by Fig. 2.7. The LF-experiment is designed to differentiate whether the internal fields on muon site is dynamic or static specially when the dip-of static lineshapes do not present in μSR time window. An external field is applied in a direction which parallel to muom beam direction and anti-parallel with respect to initial muon direction as shown by Fig. 2.8. The applied field will enhance the contribution of static field components which is parallel to muon beam line, and the applied field which is 10 bigger than the static distribution width will decouple the internal fields whereas, with the same applied field, the fast fluctuation fields will not almost affect the static lineshapes.

2.2 Muon Depolarization Function (Analysis Function)

In classical picture via Larmor precession and field distribution approach, a muon spin depolarization function is the average of time evolution of cosine between muon spin direction at any time and initial muon spin direction or before precession. The analysis functions are unique functions representing how the electronic and nuclear magnetic moments distributed in space and or evolve in time. For single magnetic field sensed by muon ensemble, this function is mathematically expressed as the projection of muon spin with respect to the initial direction of muon spin. The physics mechanism of relaxation muon in the internal magnetic field can be approached classically or quantum way. According to a classical electromagnetic theory, when a magnetic moment $(\vec{\mu})$ presents in the magnetic field, it will rotate

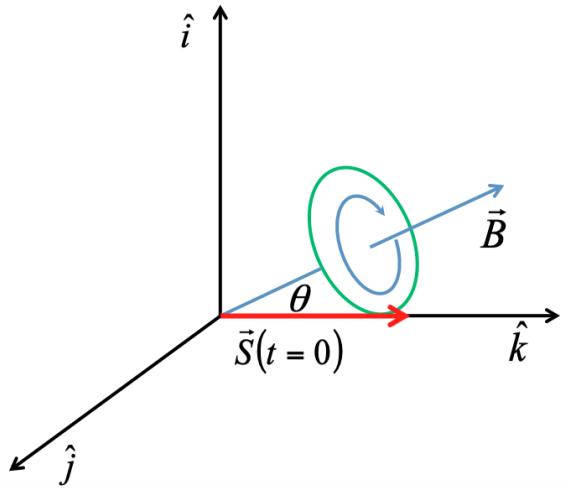

FIGURE 2.5: The schematic of Larmor precession with initial direction of polarized muon in $z-$direction.

about an axis that is parallel to the direction of magnetic field $\left(\vec{B}\right)$ known as Larmor precession, see Fig. 2. 7.

The torque of the rotation $(\vec{\tau})$ simply expressed as

$$\vec{\tau} = \vec{\mu} \times \vec{B} \rightarrow \frac{d\vec{S}}{dt} = \gamma_\mu \vec{S} \times \vec{B} \tag{2.9}$$

Since muon spin depolarization function for muon ensemble in single magnetic field defined as

$$P_z(t) = \frac{\vec{S}(t) \cdot \vec{S}(t=0)}{\left|\vec{S}(t=0)\right|^2} \tag{2.10}$$

so it is obtained the muon depolarization function:

$$P_z(t) = \cos^2\theta + \sin^2\theta \cos\omega t \tag{2.11}$$

$$= \frac{B_z^2}{B^2} + \frac{B_x^2 + B_y^2}{B^2} \cos\omega t \tag{2.12}$$

with $\omega = \gamma_\mu B$ is the angular momentum of muon precision.

From quantum mechanic, a muon polarization function is the average value of the operator of Pauli spin as a function time in a direction with respect to the axis of observation for instance in $z-$direction. In Heisenberg picture where dynamic operator is time-dependent and the wave function is time-independent, the muon polarization function is represented by

$$\left\langle \hat{\sigma}_z(t) \right\rangle = \mathbf{Tr}\left\{\hat{\rho} \cdot \hat{\sigma}_z(t)\right\}, \tag{2.13}$$

with $\hat{\rho}$ is the density operator of system and $\hat{\sigma}_z(t) = \exp\left(i\hat{H}t/\hbar\right)\hat{\sigma}_z \exp\left(-i\hat{H}t/\hbar\right)$. Since the probability to find muon spin in z$-$direction will be ½, and the product of

eigen state of spin muon in the magnetic field will be $\hat{\sigma}_z(t)$, Eq. (16) can be rewritten as

$$\left\langle \hat{\sigma}_z(t) \right\rangle = \mathbf{Tr}\left\{\hat{\sigma}_z(t) \cdot \hat{\sigma}_z(t)\right\} = \frac{1}{2}\sum_{m,n} \left| \langle m| \hat{\sigma}_z |n\rangle \right|^2 \cos\left(\omega_{m,n} t\right), \tag{2.14}$$

with m and n represent the eigenstates of Hamiltonian of muon spin in the magnetic field. The Hamiltonian for muon in the magnetic field in spherical polar coordinate can be expressed by

$$\hat{H} = -\vec{\mu} \cdot \vec{B} = \begin{bmatrix} \cos\theta & \sin\theta \exp\left(-i\phi\right) \\ \sin\theta \exp\left(i\phi\right) & \cos\theta \end{bmatrix} \tag{2.15}$$

The eigenstates from the solution of time-independent Schrödinger equation with respect to Hamiltonian in Eq. (2.15) is

$$\begin{aligned} |E_+\rangle &= \sin\left(\frac{\theta}{2}\right) \exp\left(-\frac{\phi}{2}\right) |\uparrow\rangle - \cos\left(\frac{\theta}{2}\right) \exp\left(\frac{\phi}{2}\right) |\downarrow\rangle \\ |E_-\rangle &= \cos\left(\frac{\theta}{2}\right) \exp\left(-\frac{\phi}{2}\right) |\uparrow\rangle + \sin\left(\frac{\theta}{2}\right) \exp\left(\frac{\phi}{2}\right) |\downarrow\rangle \end{aligned} \tag{2.16}$$

Putting Eq. (2.16) into Equation (2.14), it obtained

$$P_z(t) = \left\langle \hat{\sigma}_z(t) \right\rangle = \cos^2\theta + \sin^2\theta \cos\omega t \tag{2.17}$$

Chapter 3

A Model of Field Distribution for Intermediate Relaxation of μSR Time Spectra

3.1 Field distribution and relaxation function under coexistence of Gaussian and Lorentzian

3.1.1 Conversion between 3D and 1D magnetic field distributions

We start from showing how the 1D and 3D distributions of magnetic fields can be related when the field direction is random (namely, isotropic). First, we define the probability of finding a site with the magnetic field $\vec{B} = \left(B_x, B_y, B_z\right)$ as $\rho_3\left(\vec{B}\right) d^3\vec{B}$ (see Fig.1). If the field distribution is isotropic with $\rho_3\left(\vec{B}\right)$ having no dependence on the direction, we may write $\rho_3\left(\vec{B}\right) d^3\vec{B} = \rho_3\left(B\right) B^2\, dB\, \left(\cos\theta\right)\, d\phi$, where B is the size of the local field. We also define the distribution of the field size as $\rho_R\, dB$, then $\rho_R\left(B\right) = 4\pi B^2 \rho_3\left(B\right)$. The distribution of the field component in one direction, for example B_z, is given by $\rho_1\left(B_z\right)\, dB_z$. In the cylindrical coordinate $\left(B_z, B_\rho, \phi\right)$, we get by projection

$$\rho_1\left(B_z\right) = \int_0^\infty \rho_3\left(B\right) 2\pi B_\rho dB_\rho \tag{3.1}$$

where $B^2 = B_2^2 + B_\rho^2$ and the integration is done keeping B_z constant. Using $BdB = B_\rho\, dB_\rho$,

$$\rho_1\left(B_z\right) = \int_{B_z}^\infty \rho_3\left(B\right) 2\pi B\, dB. \tag{3.2}$$

It follows,

$$\frac{d\rho_1\left(B_z\right)}{dB_z} = -2\pi B_z \rho_3\left(B_z\right). \tag{3.3}$$

As the expression of the variable does not matter, we rewrite Eq. (3.1) as

$$\rho_3\left(B\right) = -\frac{1}{2\pi B}\frac{\rho_1\left(B\right)}{dB} \tag{3.4}$$

and

$$\rho_R(B) = -2B\frac{d\rho_1(B)}{dB}. \tag{3.5}$$

We set two distributions of B, Gaussian and Lorentzian. Each distribution is characterized by Δ or a as the width of the distribution. For Gaussian, we get

$$\rho_{1,G}(B) = \frac{\gamma_\mu}{\sqrt{2\pi}\Delta}\exp\left(-\frac{\gamma_\mu^2 B^2}{2\Delta^2}\right), \tag{3.6a}$$

$$\rho_{3,G}(B) = \frac{\gamma_\mu^3}{(2\pi)^{3/2}\Delta^3}\exp\left(-\frac{\gamma_\mu^2 B^2}{2\Delta^2}\right), \tag{3.6b}$$

$$\rho_{R,G}(B) = \frac{\sqrt[2]{\gamma}_\mu^3}{\sqrt{\pi}\Delta^3}B^2\exp\left(-\frac{\gamma_\mu^2 B^2}{2\Delta^2}\right). \tag{3.6c}$$

For the Lorentzian case,

$$\rho_{1,L}(B) = \frac{\gamma}{\pi}\frac{a}{\left(a^2+\gamma_\mu^2 B^2\right)}, \tag{3.7a}$$

$$\rho_{3,L}(B) = \frac{\gamma_\mu^3}{\pi^3}\frac{a^2}{\left(a^2+\gamma_\mu^2 B^2\right)^2}, \tag{3.7b}$$

$$\rho_{R,L}(B) = \frac{4\gamma_\mu^3}{\pi}\frac{aB^2}{\left(a^2+\gamma_\mu^2 B^2\right)^2}. \tag{3.7c}$$

3.1.2 3D convolution of the static magnetic field distribution

First, we describe the distribution $\rho_{GL}(B)$ as the convolution of the Gaussian and Lorentzian fields. For the distribution of the summed field component in one direction, we can use 1D convolution,

$$\begin{aligned}\rho_{1,GL}(B) &= \int \rho_{1,G}(B-B_1)\,\rho_{1,L}(B_1)\,dB_1 \\ &= \frac{a\gamma_\mu^2}{\sqrt{2}\pi^{3/2}\Delta}\int \frac{\exp\left(-\frac{\gamma_\mu^2(B-B_1)^2}{2\Delta^2}\right)}{\left(a^2+\gamma_\mu^2 B^2\right)}\,dB_1.\end{aligned} \tag{3.8}$$

To obtain the 3D distribution $\rho_3\left(\vec{B}\right)$ of the vector summed field, we need 3D convolution. The convolution should be done by varying one of the fields, $\vec{B}_1$, while the other field is automatically determined. This leads to that $\vec{B}_2 = \vec{B} - \vec{B}_1$. The probability of having $\vec{B}_1$ and $\vec{B}_2$ at the same time is $\rho_{3,G}\left(\vec{B}_2\right)\rho_{3,L}\left(\vec{B}_1\right)$. This probability should be integrated for all possible $\vec{B}_1$ to find the probability of having field $\vec{B}$. Thus,

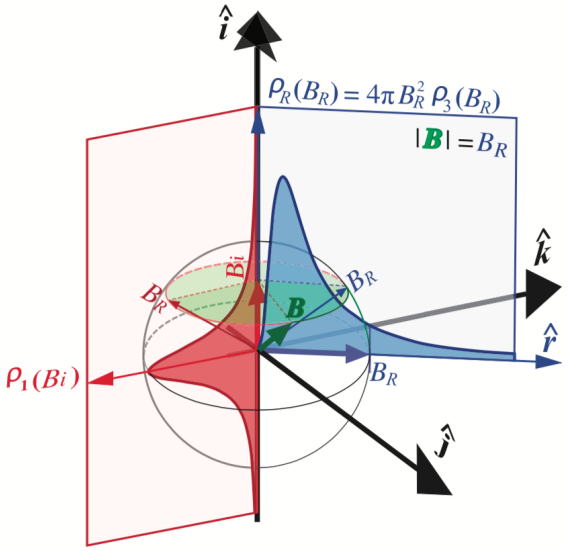

FIGURE 3.1: Relation between the 3D field distribution, $\rho_3\left(\vec{B}\right)$ and its distribution projection in one dimension, $\rho_1(B_i)$. We also define the field size distribution, $\rho_R(B)$. They are normalized so that $\int_{-\infty}^{\infty} \rho_1(B_i)\, dB_i = 1$, $4\pi \int_0^{\infty} \rho_3(B)\, B^2\, dB = 1$, and $\int_0^{\infty} \rho_R(B)\, dB = 1$

.

$$\begin{aligned}
\rho_{3,GL}\left(\vec{B}\right) &= \int \rho_{3,G}\left(\vec{B}_2\right) \rho_{3,GL}\left(\vec{B}_1\right) d^3\vec{B}_1 \\
&= \int\int \rho_{3,G}(B_2)\, \rho_{3,GL}(B_1)\, B_1^2\, dB_1\, d(\cos\theta_1) \\
&= \frac{a\gamma_\mu^6}{2^{3/2}\pi^{7/2}} \int\int \frac{\exp\left(-\frac{\gamma_\mu^2 B_2^2}{2\Delta^2}\right)}{\left(a^2+\gamma_\mu^2 B_1^2\right)^2} B_1^2 dB_1.
\end{aligned} \tag{3.9}$$

where $B_2^2 = B^2 + B_1^2 - 2B_1 B\cos\theta_1$. The integration over $\cos\theta_1$ can be done analytically and this gives

$$\begin{aligned}
\rho_{3,GL}(B) &= \frac{\sqrt{2}a\gamma_\mu^4}{\pi^{3/2}\Delta} \int_0^{\infty} \frac{\left[BB_1 \exp\left(-\frac{\gamma_\mu^2 (B+B_1)^2}{2\Delta^2}\right) - \exp\left(-\frac{\gamma_\mu^2 (B-B_1)^2}{2\Delta^2}\right)\right]}{\left(a^2+\gamma_\mu^2 B_1^2\right)^2} dB_1 \\
&= \frac{\sqrt{2}a\gamma_\mu^4}{\pi^{3/2}\Delta} \int_{-\infty}^{\infty} \frac{BB_1 \exp\left(-\frac{\gamma_\mu^2 \left(B-B_1^2\right)}{2\Delta^2}\right)}{\left(a^2+\gamma_\mu^2 B_1^2\right)^2} dB_1.
\end{aligned} \tag{3.10}$$

Next, we show another derivation of the 3D convolution form. When two independent distributions contribute, the projected sum of fields is represented by the 1D convolution,

$$\rho_{1,GL}(B) = \int_{-\infty}^{\infty} \rho_{1,G}(B - B_1)\,\rho_{1,L}(B_1)\; dB_1. \tag{3.11}$$

As the sum of field distribution is also isotropic, using the relation Eq.(4.9), we get

$$\begin{aligned} \rho_{R,GL}(B) &= -2B\frac{d\rho_{1,GL}(B)}{dB} \\ &= \int (-2B)\,\frac{d\rho_{1,G}(B - B_1)}{dB}\rho_{1,GL}(B_1)\; dB_1. \end{aligned} \tag{3.12}$$

It can be shown that this lead to the same form as Eq.(4.14). However, instead, we here derive another form, applying the Fourier transform to obtain the relaxation function.

$$\rho_{R,GL}(B) = \int (-2(B - B_1) - 2B_1)\,\frac{(d\rho_{1,G}(B - B_1))}{dB}\rho_{1,L}(B_1)\; dB_1 \tag{3.13}$$

from the relations, $-2(B - B_1)\,\frac{d\rho_{1,G}(B-B_1)}{dB} = \rho_{R,G}(B - B_1)$ and $\frac{d\rho_{1,G}(B-B_1)}{dB} = -\frac{d\rho_{1,G}(B-B_1)}{dB_1}$,

$$\begin{aligned} \rho_{R,GL}(B) = \int_{-\infty}^{\infty} \rho_{R,G}(B - B_1)\,\rho_{1,L}(B_1)\; dB_1 + \int_{-\infty}^{\infty} \rho_{1,G}(B - B_1)\,\rho_{R,L}(B_1)\; dB_1 \\ - 2\int_{-\infty}^{\infty} \rho_{1,G}(B - B_1)\,\rho_{1,L}(B_1)\; dB_1. \end{aligned} \tag{3.14}$$

As the above handling is purely mathematical, we should note that ρ_R's are defined even in negative B range by Eq.(4.9) and $\rho_R(-B) = \rho_R(B)$ as $\rho_1(B)$'s are assumed symmetric.

3.1.3 Muon spin relaxation function under isotropic field distribution

Now, let's discuss muon spin in referring to internal-field distribution $\rho_R(B)$. Hence, muons have a polarization-axis as ensemble, and the polarization can be depolarized (relaxed) in time due to the spin-precession around the internal field, because each muon will sense a different magnetic field at the specific position of the muon. For simplicity, let's describe in a semi-classical manner. An example of muon-spin-precession is schematically illustrated in Fig. 3.1. Taking the quantum axis to be in the direction of the muon polarization at $t = 0$, θ and ϕ are the polar and azimuthal angles of B at the muon site, respectively. The B distributes randomly in the angle referring to the quantum-axis. Its field strength is described by the 3D distribution $\rho_3(B)$ (or the size distribution $\rho_R(B)$). The muon spin precesses around B with the Larmor precession frequency,ω_μ, where $\omega_\mu = \gamma_\mu B$. By taking ensemble, the component vertical to the initial polarization is canceled out because of the symmetry and only the spin polarization parallel to the initial spin remains,

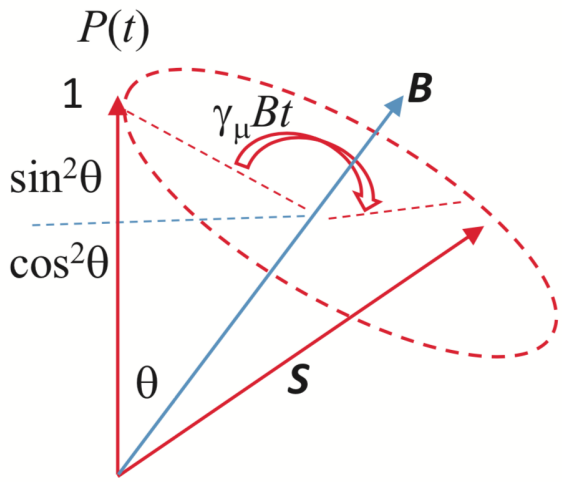

FIGURE 3.2: The spin rotation in zero-field. Decomposition of the muon polarization into the spin-conserving part, $\cos^2\theta$, and and the spin-precession part, $\sin^2\theta$, are given. The precession part rotates around the internal magnetic field $\vec{B}$ with Larmor frequency of $\gamma_\mu B$

.

$$\begin{aligned} P(t) &= \int\int\int \left(\cos^2\theta + \sin^2\theta \cos\left(\gamma_\mu B t\right)\right) \rho_3(B)\, d^3\vec{B} \\ &= \int dB \int \left(\cos^2\theta + \sin^2\theta \cos\left(\gamma_\mu B t\right)\right) \rho_3(B) \frac{1}{2}\rho_R(B). \end{aligned} \tag{3.15}$$

In the case of an isotropic field distribution, $\rho_R(B)$ is independent of θ, so the we can take an integral over $\cos\theta$, resulting in

$$P(t) = \frac{1}{3} + \frac{2}{3}\int_0^\infty \cos\left(\gamma_\mu B t\right) \rho_R(B)\, dB = \frac{1}{3} + \frac{2}{3} P_{osc}(t) \tag{3.16}$$

The P_{osc} is the oscilation component of the muon−spin relaxation. We here define two Fourier transform, one in the range 0 to ∞ and the other in the range $-\infty$ to ∞ as follows,

$$\begin{aligned} \hat{\rho}^+ &= \int_0^\infty \cos\left(\gamma_\mu B t\right) \rho(B)\, dB \\ \hat{\rho}(t) &= \int_{-\infty}^\infty \cos\left(\gamma_\mu B t\right) \rho(B)\, dB. \end{aligned} \tag{3.17}$$

For symmetric distribution $\rho(B)$, $\hat{\rho}(t) = 2\hat{\sigma}^+(t)$.

Now, we set $P_{osc}(t) = \hat{\sigma}^+_{R,GL}$, where the field distribution is given as the convolution Eq.(3.14).

$$\begin{aligned}\hat{\rho}^{+}_{R,GL}(t) &= \frac{1}{2}\hat{\sigma}_{R,GL}(t) \\ &= \frac{1}{2}\int_{-\infty}^{\infty}\cos\left(\gamma_\mu Bt\right)\rho_{R,GL}(B)\,dB \\ &= \frac{1}{2}\int_{-\infty}^{\infty}\cos\left(\gamma_\mu Bt\right)\left[\int_{-\infty}^{\infty}\rho_{\rho R,G}(B-B_1)\,\rho_{1,L}(B_1)\,dB_1\right]dB \\ &\quad \frac{1}{2}\int_{-\infty}^{\infty}\cos\left(\gamma_\mu Bt\right)\left[\int_{-\infty}^{\infty}\rho_{1,G}(B-B_1)\,\rho_{R,L}(B_1)\,dB_1\right]dB \\ &\quad \int_{-\infty}^{\infty}\cos\left(\gamma_\mu Bt\right)\left[\int_{-\infty}^{\infty}\rho_{1},G(B-B_1)\,\rho_{1,L}(B_1)\,dB_1\right]dB\end{aligned} \tag{3.18}$$

Using the well-known principles of the Fourier transform of functions f and g, additive principle $\left(\widehat{f+g}\right)=\hat{f}+\hat{g}$ and convolution principle $\left(\widehat{f\star g}\right)=\hat{f}\times\hat{g}$, where $f\star g$ means convolution,

$$\begin{aligned}\hat{\rho}^{+}_{R,GL} &= \frac{1}{2}\int_{-\infty}^{\infty}\cos\left(\gamma_\mu Bt\right)\rho_{R,G}(B)\,dB\int_{-\infty}^{\infty}\cos\left(\gamma_\mu Bt\right)\rho_{1,L}(B)\,dB \\ &\quad \frac{1}{2}\int_{-\infty}^{\infty}\cos\left(\gamma_\mu Bt\right)\rho_{1,G}(B)\,dB\int_{-\infty}^{\infty}\cos\left(\gamma_\mu Bt\right)\rho_{R,L}(B)\,dB \\ &\quad \frac{1}{2}\int_{-\infty}^{\infty}\cos\left(\gamma_\mu Bt\right)\rho_{1,G}(B)\,dB\int_{-\infty}^{\infty}\cos\left(\gamma_\mu Bt\right)\rho_{1,L}(B)\,dB \\ &= \frac{1}{2}\hat{\rho}_{R,G}(t)\,\hat{\rho}_{1,L}(t)+\frac{1}{2}\hat{\rho}_{1,G}(t)\,\hat{\rho}_{R,L}(t)-\frac{1}{2}\hat{\rho}_{1,G}(t)\,\hat{\rho}_{1,L}(t) \\ &= \hat{\rho}^{+}_{R,G}(t)\,\hat{\rho}_{1,L}(t)+\hat{\rho}_{1,G}(t)\,\hat{\rho}^{+}_{R,L}(t)-\hat{\rho}_{1,G}(t)\,\hat{\rho}_{1,L}(t)\end{aligned} \tag{3.19}$$

Note that the relation is applicable as far as the two distributions are independent and both isotropic. In a special case when the two distributions are Gaussian and Lorentzian, their Fourier counterparts are well-known including those for 3D distributions [68, 104, 103],

$$\hat{\rho}_{1,G}(t) = \exp\left(-\frac{\Delta^2t^2}{2}\right) \tag{3.20a}$$

$$\hat{\rho}^{+}_{R,G}(t) = \left(1-\Delta^2t^2\right)\exp\left(-\frac{\Delta^2t^2}{2}\right) \tag{3.20b}$$

$$\hat{\rho}_{1,L}(t) = \exp\left(-at\right) \tag{3.20c}$$

$$\hat{\rho}^{+}_{R,L}(t) = (1-at)\exp\left(-at\right). \tag{3.20d}$$

We get

$$\hat{\rho}^{+}_{R,GL}(t) = \left(1-\Delta^2t^2-at\right)\exp\left(-\frac{\Delta^2t^2}{2}\right)\exp\left(-at\right) \tag{3.21}$$

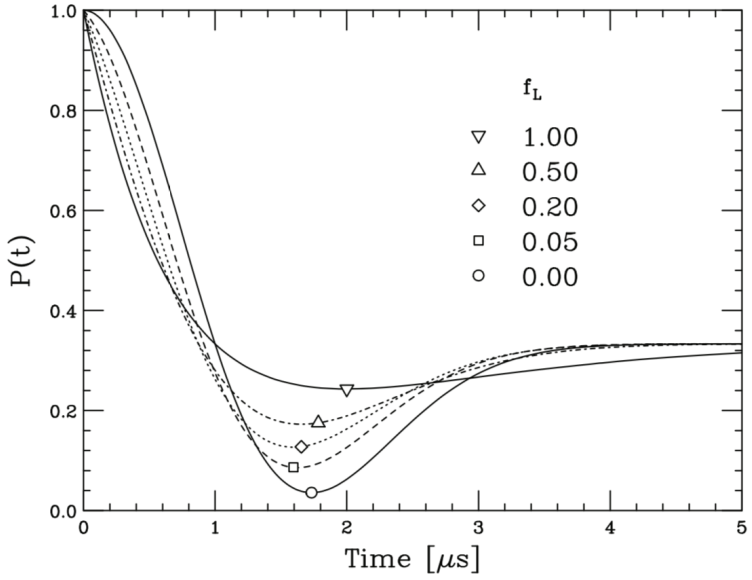

FIGURE 3.3: Simulation of Eq.(4.26) with different mixing ratio of Lorentzian and Gaussian, f_L=0, 0.05, 0.2, 0.5, and 1, while keeping $\sqrt{\Delta^2 + a^2} = 1\mu s^{-1}$. The locations of the minimum are also shown by open marks.

as the oscillation part. Thus, the relaxation function under random directional field distribution is

$$P_{GLKT}(t) = \frac{1}{3} + \frac{2}{3}\left(1 - \Delta^2 t^2 - at\right)\exp\left(-\frac{\Delta^2 t^2}{2}\right)\exp\left(-at\right) \tag{3.22}$$

This is the correct extension form of the Kubo-Toyabe relaxation function [104, 103] for the convoluted distribution of Gaussian and Lorentzian. The function becomes Gaussian Kubo- Toyabe if $a = 0$ and Kubo−Toyabe if Δ. The same function unction was mentioned in [124, 121] although no detail derivations were shown there.

The behavior of Eq.(3.22) is graphically shown in Fig. 4.3 by changing the fraction of Lorentzian source contribution $f_L = a^2/\left(\Delta^2 + a^2\right)$ while keeping $\sqrt{\Delta^2 + a^2} = 1\mu s^{-1}$. One of the most characteristic features of the relaxation function is the dip. The location of the minimum of the dip can be found by taking the derivative of $P_{GLKT}(t)$ and solving the cubic equation

$$\Delta^4 t^3 + 2a\Delta^2 t^2 + \left(a^2 - 3\Delta^2\right)t^2 - 2a = 0. \tag{3.23}$$

Using Cardano's method, we get as the solution

$$t_{min} = \frac{2}{3}\left[\sqrt{b^2 + 9}\cos\left(\phi/3\right) - b\right]/\Delta, \tag{3.24}$$

where $b = a/\Delta$, and $\phi\left(0 \sim \frac{\pi}{2}\right)$ is chosen so that $\tan\phi = \sqrt{\left(1 + 9/b^2\right)^3 - 1}$. In here, the Gaussian and Lorentzian distributions have the minimum dip in their shape at

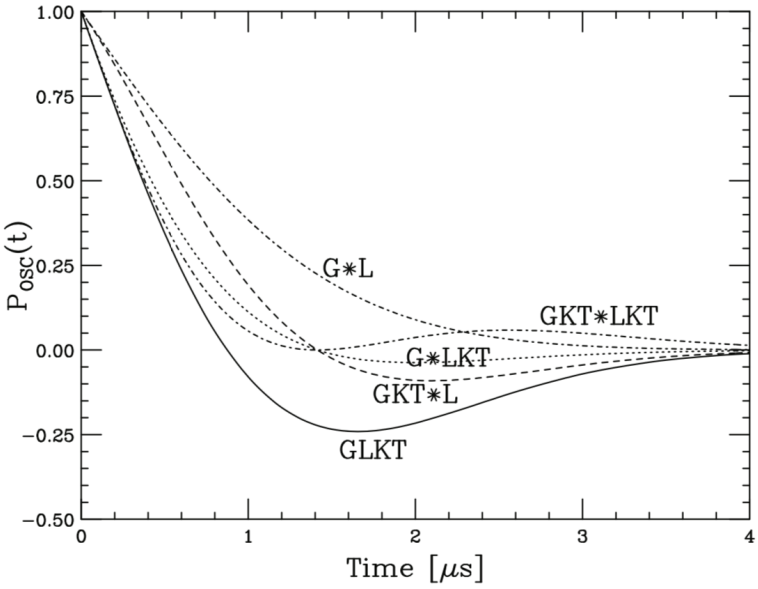

FIGURE 3.4: Comparison of the oscillating part of the relaxation function of Eq.(3.22) with other functions given as products of the relaxation functions of Gaussian- and Lorentzian-origin with $\Delta = 0.707\mu s^{-1}$ and $a = 0.707\mu s^{-1}$, respectively. G: Gaussian, GKT: Gaussian Kubo-Toyabe, L: Lorentzian, LKT: Lorentzian Kubo-Toyabe, and GLKT: extended Kubo-Toyabe function [Eq. (3.22)]for the convolution of Gaussian and Lorentzian. G*L: $\exp\left(-\frac{\Delta^2 t^2}{2} - at\right)$, GKT*L: $(1-\Delta^2 t^2)\exp\left(-\frac{\Delta^2 t^2}{2} - at\right)$, G*LKT: $(1-at)\exp\left(-\frac{\Delta^2 t^2}{2} - at\right)$, GKT*LKT: $(1-\Delta^2 t^2)\,(1-at)\exp\left(-\frac{\Delta^2 t^2}{2} - at\right)$, and GLKT: $(1-\Delta^2 t^2 - at)$

$t_{min} = \sqrt{3}/\Delta$ and $2/a$, respectively.

3.2 Comparison with other relaxation functions

There have been used several different relaxation functions in an attempt to fit the μSR time spectrum in the cross-over regime. Typical trials were to approximate the relaxation as a product of functions of Gaussian and Lorentzian origin. The dip described in Eq.(3.22) can be compared with several different combinations of the product in Fig. 3.4. Unfortunately, it is obvious that no other function form is successful in reproducing the correct form.

We tested how the SKT function, Eq.(1.11), can be compared to the exact form. Since there is no equation known relating α and λ to Δ and a, α and λ were just chosen, making the functions the best matched. Figure 3.5 shows a reasonable match as seen for the case of $f_L = 0.05$. Table 3.1 shows the fitted α and λ parameters for several mixing ratios. The root- mean-square (RMS) deviation from the exact function is also shown. The stretched function parameters seem to reasonably approximate

TABLE 3.1: Parameters of Eq. (3.22) given by a fit to Eq. (1.11). The f_L is the mixing ratio of the Lorentzian source. The RMS is the root-mean-square discrepancy between the two functions.

Source distribution, $P_{GLKT}(t)$			Stretched Kubo-Toyabe, $P_{SKT}(t)$		
f_L	Δ	a	α_S	λ_S	RMS
0.00	1.0000	0.0000	2.0000	1.0000	0.0000
0.25	0.8660	0.5000	1.4933	1.1791	0.0083
0.50	0.7071	0.7071	1.3146	1.1748	0.0080
0.75	0.5000	0.8660	1.1638	1.1178	0.0059
1.00	0.0000	1.0000	1.0000	1.0000	0.0000

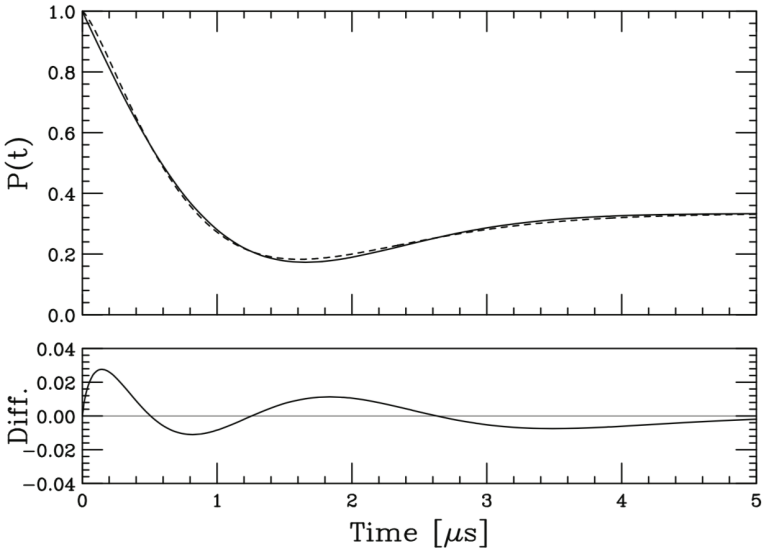

FIGURE 3.5: Top: Comparison of the exact relaxation function Eq.(4.26) (solid line), and Eq.(4.4) (dashed line) for $f_L = 0.5$ with $\sqrt{\Delta^2 + a^2} = 1\mu s^{-1}$. Bottom: Difference between Eq.(4.4) and Eq.(4.26). The best fit was made with $\alpha = 1.315$ and $\lambda = 1.175\mu s^{-1}$

the exact function within the RMS deviation $\sim 1\%$. However, some differences are evident such as the slower decrease in $P_{SKT}(t)$ at time zero. Note that the physics basis of the SKT function is vague compared to the exact form.

3.3 Responses of the intermediate analysis function against external parameters

3.3.1 Responses to magnetic fields

The μSR experiment in the zero-field condition is the unique and strong advantage to use the muon which has the self-polarization along of its initial spin direction. In addition to this, responses of the μSR time spectrum in magnetic fields applied from outside to materials are also important to investigate dynamic and static properties of local fields at the muon site [68, 205]. In order to investigate dynamic properties

of local fields at the muon site, the magnetic field is applied along the same direction of the initial muon-spin polarization. We call this applied magnetic field as the longitudinal field (LF). Accordingly, we also created the general formation to describe the magnetic field dependence of our developed intermediate analysis function.

In order to describe the LF dependence of the μSR time spectrum, we need to add is LF with the amount of B_0 along the quantum axis which is the same with the initial muon- spin polarization. Since it was not so easy to write down the LF dependence following the same detail manner from the concept drawn in Fig. 1, we used a different way to derive the final equation. That is to use the Kubo formula with the Fourier transform of the field distribution [103].

$$\begin{aligned} P_z\left(t, B_0\right) = 1 - 2t\left(\frac{d}{dt}\left[Q\left(t\right)\right]\right)\frac{\cos\omega_0 t}{\left(\omega_0 t\right)^2} + \frac{2}{\omega_0^2}\lim_{t\to 0}\left(\frac{\frac{d}{dt}\left[Q\left(t\right)\right]}{t}\right) \\ + 2\int_0^t \frac{\sin\omega_0\tau}{\omega_0^3\tau}\frac{d}{d\tau}\left(\frac{\frac{d}{d\tau}\left[Q\left(\tau\right)\right]}{\tau}\right)d\tau. \end{aligned} \tag{3.25}$$

Here, $\omega_0 = \gamma_\mu B_0$. The $Q\left(t\right)$ is a Fourier transform of the convoluted distribution between Gaussian and Lorentzian. Referencing Eq.(4.26), $Q\left(t\right)$ is given as follows.

$$Q\left(t\right) = \exp\left(-at - \frac{\Delta^2 t^2}{2}\right) \tag{3.26}$$

Simply calculate this equation, we reach to the required equation to draw the LF dependence of the muon-spin polarization, $P_{LFGLKT}\left(t, B_0\right)$, as;

$$\begin{aligned} P_{LFGLKT}\left(t\right) = 1 &- \frac{a}{\omega_0}\left(J_1\left(\omega_0 t\right)\exp\left(-at - \frac{\Delta^2 t^2}{2}\right)\right) \\ &- \frac{2\Delta^2}{\omega_0^2}\left(1 - \exp\left(-at - \frac{\Delta^2 t^2}{2}\right)\cos\left(\omega_0 t\right)\right) \\ &- \frac{a^2}{\omega_0^2}\left(J_0\left(\omega_0 t\right)\exp\left(-at - \frac{\Delta^2 t^2}{2}\right) - 1\right) \\ &- \left[1 + \left(\frac{a^2 - 3\Delta^2}{\omega_0^2}\right)\right] a\int_0^t J_0\left(\omega_0\tau\right)\exp\left(-a\tau - \frac{\Delta^2\tau^2}{2}\right)d\tau \\ &- \left(\frac{a^2\Delta^2}{\omega_0^2} - \frac{2\Delta^4}{\omega_0^3}\right)\int_0^t \sin\left(\omega_0\tau\right)\exp\left(-a\tau - \frac{\Delta^2\tau^2}{2}\right)d\tau \\ &- \frac{a\Delta^2}{\omega_0^2}\int_0^t \cos\left(\omega_0\tau\right)\exp\left(-a\tau - \frac{\Delta^2\tau^2}{2}\right)d\tau. \end{aligned} \tag{3.27}$$

in here, J_0 and J_1 are the 0^{th} and 1^{st} order spherical Bessel functions, respectively. Other expressions are the same with those used in the previous sections. Figure 3.6 shows the schematic drawing of Eq.(3.27) in the case of $\Delta = a0.707\mu\text{ssec}^1$ with changing LF.

The LF dependence of the time spectrum with increasing LF described by Eq.(3.27)

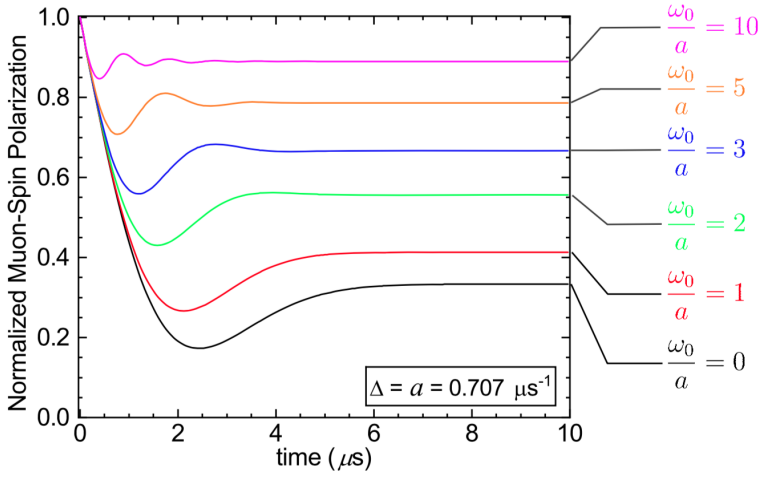

FIGURE 3.6: Eq.(4.31) against variable longitudinal fields with $\Delta = a = 0.707\mu\text{sec}^1$. In the case of $\frac{\omega_0}{a} \gg 10$, the time spectrum is nearly decoupled from the internal field which has the intermediate distribution between Gaussian and Lorentzian.

has the similar characters to those of the Gaussian and Lorentzian functions [68, 205]. Those are 1) the dip in the time spectrum becomes smaller, *ii*) the so-called $\frac{1}{3}$-tail of the spectrum goes up and *iii*) the additional muon-spin precession around LF with the small amplitude appears in the earlier time region, and *iv*) the time spectrum becomes almost decoupled from local fields and locked along by LF keeping the initial muon-spin polarization in the case of $\frac{\omega_0}{a} \gg 10$.

3.3.2 Responses to dynamic local fields

In many cases, we need to discuss dynamic effects on the μSR time spectrum. Changes in local fields at the muon site in time are caused by magnetic transitions [203, 27, 87, 80, 216, 237, 141, 157, 8], molecular dynamics [25], ion/spin diffusions and muon motions [144, 79, 219, 196, 126, 165, 86]. If those dynamic changes in local fields happen within the μSR time window (10^{-6}-10^{-11} sec), the μSR time spectrum is affected and shows different behavior from the static scenario which was given in previous sections.

Accordingly, we describe the dynamic effect on the basis of Eq.(3.22). In order to do this, we need to set some assumptions on the dynamic effect following the well established ways to take into account the dynamic motion of the muon [68]. Those are *i*) local fields at the muon site do not change in time, *ii*) the muon is hopping in local fields, *iii*) the muon's motion can be described as the Markov process with the hopping frequency of υ on the basis of the strong-collision model, *iv*) the hopping frequency is within the μSR characteristic time window.

What happen on the muon in those dynamic conditions is as follows. When the muon is trapped at one position at time t, the muon sees static local fields distributed at the muon position and shows the Larmor precession motion. The muon does not

hop during a short time t' after t and depolarizes its spin polarization following Eq.(3.22). Just after the muon hops to a next place after t', the muon starts to see different local fields and depolarizes again around those different local fields following Eq.(3.22) with the different initial condition from that given at t. After the hopping process is repeated within the μSR observation time which is typically up to around 20μsec in the case of the use of a pulsed muon [143], the final μSR time spectrum, P_{DGLKT}, can be described as the total sum of those hopping procedure as follows;

$$P_{DGLKT}(t,v) = \exp(-vt)\left[P_{GLKT}(t) + v\int_0^t P_{GLKT}(t-t_1)\,P_{GLKT}(t_1)\,dt_1 + v^2\int_{t_2}^t\int_0^{t_2} P_{GLKT}(t-t_2)\,P_{GLKT}(t_2-t_1)\,P_{GLKT}(t_1)\,dt_2\,d_1 + \cdots\right] \tag{3.28}$$

The Eq.(39) is summarized as follows.

$$P_{DGLKT}(t,v) = \exp(-vt)\,P_{GLKT}(t) + v\int_0^t \exp\left(-v\left(t-t'\right)\right)P_{GLKT}\left(t-t'\right) P_{DGLKT}\left(t',v\right)\,dt' \tag{3.29}$$

Here, $\exp(-v(t-t'))$ is the correlation function of the muon's hopping motion on the basis of the strongly collision model [68]. The inverse of v is related to the dynamic muon-spin depolarization rate. This equation has to be solved self-consistently because the right hand term includes the same depolarization term.

Figure 3.7 shows a schematic picture of Eq.(3.29) simulated by changing v to be 0, 0.2, 0.5, 1, 2, 5, 10, 20, 50, 100, 200 and 500 MHz. Δ and a were set to be some convenient values in order to make simulated time spectra to be easy to see within the experimental time region of μSR up to around 10 μsec. The overall picture of the response of the μSR time spectrum is different from that described by Eq.(3.22) (Fig. 3.7(a) [68]) especially when the ratio $\frac{a}{\Delta}$ become large. The $\frac{1}{3}$-tail starts to relax first when the value of v increases from the zero value. With increasing the value of v, the dip disappears and the $\frac{1}{3}$-tail can no longer be observed. The time spectrum tends to show no motional narrowing effect for the higher values of $\frac{a}{\Delta}$. This is because of the non-negligible LKT component in Eq.(3.29) which is well known not to show the motional narrowing effect [55, 116, 188].

3.4 Comparison with μSR data

3.4.1 Muon-spin depolarization by distributed static local fields

Candidate materials to which Eq.(3.22) may be applied are organic molecules, especially organic molecular superconductors. The general tendency of the crystal

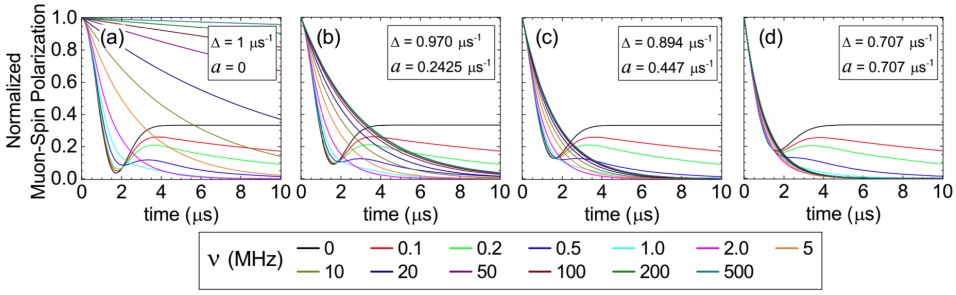

FIGURE 3.7: Schematic picture of Eq.(3.29) against variable v to be 0, 0.2, 0.5, 1, 2, 5, 10, 20, 50, 100, 200 and 500 MHz. (a) The pure Gaussian case [68], (b) $\frac{a}{\Delta} = \frac{1}{4}$, (b) $\frac{a}{\Delta} = \frac{1}{2}$ and (b) $\frac{a}{\Delta} = 1$. In the case of $v \gg 1$ MHz, the time spectrum no longer has the so-called $\frac{1}{3}$-tail.

structure of those kinds of organic systems shows low-dimensional and anisotropic states. In addition, atomic components of those organic systems contain only light elements that do not have large natural abundance of nuclear magnetic moments, like C and O. Those conditions can realize non uniform and dilute spin conditions.

As an example, the intermediate μSR time spectrum was reported in the paramagnetic state of the low dimensional organic superconductor, λ-$(BETS)_2GaCl_4$ with (BETS=$(CH_2)_2S_2Se_2S_2(CH_2)_2$) [180]. The λ-$(BETS)_2GaCl_4$ shows the superconducting state below about 5.3 K and does not have any clear localized magnetic moment [77, 99, 180]. μSR time spectrum showed the intermediate shape and was independent of temperature in the paramagnetic state [180]. We can technically analyze this intermediate μSR time spectrum by using Eq.(1.9). However, this method is hard to be appropriate because almost no localized electronic magnetic moment is expected in this system. From the view point of μSR, the nuclear dipole field is well recognized to be time independent due to the higher frequency of the μSR characteristic time window which is much faster than dynamic fluctuations of nuclear dipoles [68]. Accordingly, Eq.(3.22) should be appropriate to analyze time spectra obtained from the μSR measurement on λ-$(BETS)_2GaCl_4$

We applied Eq.(3.22) to intermediate μSR time spectra measured in λ-$(BETS)_2GaCl_4$. Figure 8 is the best fit results done by using Eq.(3.22). The time spectrum was measured at 1 K, 10 K, 20 K, and 50 K in which the system is in the paramagnetic state and the μSR time spectrum did not show the temperature dependence at all. The fitting results seem to be well successful with value of a and Δ to be 0.10(1) μsec^{-1} and 0.14(1)μsec^{-1}, respectively. This results indicates that the distribution of local fields at the muon site coming from surrounding nuclear dipoles deviates from Gaussian and becomes to be the intermediate shape. Since λ-$(BETS)_2GaCl_4$ has the anisotropic low-dimensional crystal structure, there are some spatial regions where the density of nuclear dipoles is largely different. In such a case, some muons which stop near the high- and low-density areas feel stronger and weaker local fields, respectively. This condition makes the field distribution wider and deforms the Gaussian shape.

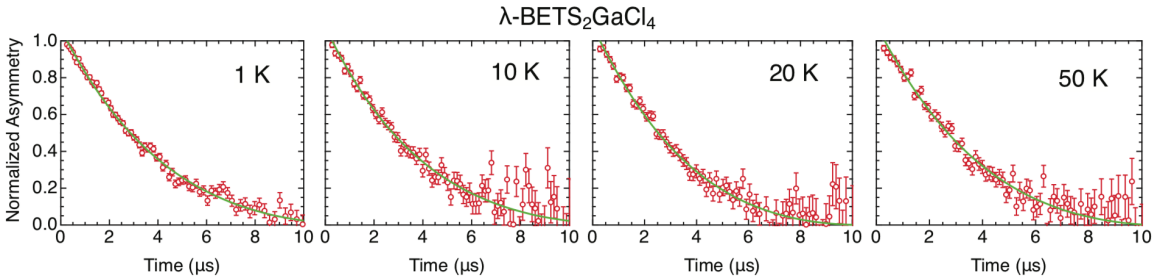

FIGURE 3.8: Time spectra measured on λ-$(BETS)_2GaCl_4$ at 1 K, 10 K, 20 K and 50 K [180]. Green solid lines indicates the best fit result by using using Eq.(4.26).

However, the deformation from the Gaussian shape due to non homogeneity of nuclear dipole will possibly occur if there are more than one muon site per unit cell. Thus, muon stopping site on this material should be investigated.

The highly anisotropic low-dimensional crystal structure will result field anisotropy on muon site, and, for layer structure, the second moment of Gaussian field from dense nuclear dipoles will take a form $\Delta_i^2 = \Delta_j^2 \neq \Delta_k^2$. The anisotropy in Gaussian field was reported will change both the relaxation rate and dip shape of isotropic Gaussian Kubo-Toyabe function, but it still persists the initial character of Gaussian relaxation [51]. Since the Gaussian field anisotropy cannot produce observed intermediate lineshapes, we propose Lorentzian field component should be contributed by the low abundance of isotope nuclear dipoles. The Lorentzian field from this dilute static randomly alignment of nuclear dipoles will convolute with Gaussian field originating from high abundance of nuclear dipole isotope to form intermediate lineshapes in between Gaussian- and Lorentzian-shape. The effect of isotopes on the change of Gaussian relaxation has been observed in $PrPt_4Ge_{12}$ [124]. Table 3.2 and 3.3 listed element isotopes of λ-$(BETS)_2GaCl_4$ have magnetic dipole moments. We expected internal field from each low abundance of isotopes (Se, S, H and C) will produce Lorentzian field, and the Lorentzian field from different low abundance isotopes will convolute each other and remain Lorentzian. So did high abundance isotopes. The Gaussian field from each high abundance isotopes (Ga, Cl and C) as shown by table 3.2 will convolute each other, and the result of the convolution will remain Gaussian.

3.4.2 Muon-spin depolarization by fluctuating dynamic local fields

In addition to the static regime, the dynamic regime due to the appearance of fluctuating dynamic local fields also causes changes in the μSR time spectrum deforming its shape from Gaussian to the intermediate one as the function of the temperature. An example showing this case was obtained on the La−based high-T_c oxide, $La_{2-x}Sr_xCuO_4$ with x of 0.024. In this Sr-doping regime, the system was underdoped of carriers and showed the magnetic transition around 10 K. Besides, the μSR time

TABLE 3.2: Low abundance of elements isotopes with nuclear dipole moments which is expected will contribute to Lorentzian field on muon site

Element	Abundance (%)	μ(nm)
$^{77}_{34}$Se	7.6	+0.535
$^{33}_{16}$S	0.76	+0.644
$^{2}_{1}$H	0.02	+0.857
$^{13}_{16}$C	1.1	+0.702

TABLE 3.3: High abundance of elements isotopes with nuclear dipole moments will contribute to Gaussian field on muon site

Element	Abundance (%)	μ(nm)
$^{69}_{31}$Ga	60.11	+2.017
$^{69}_{31}$Ga	39.89	+2.562
$^{35}_{17}$Cl	76	+0.822
$^{37}_{17}$Cl	24	+0.684
$^{1}_{1}$H	99.98	+2.793

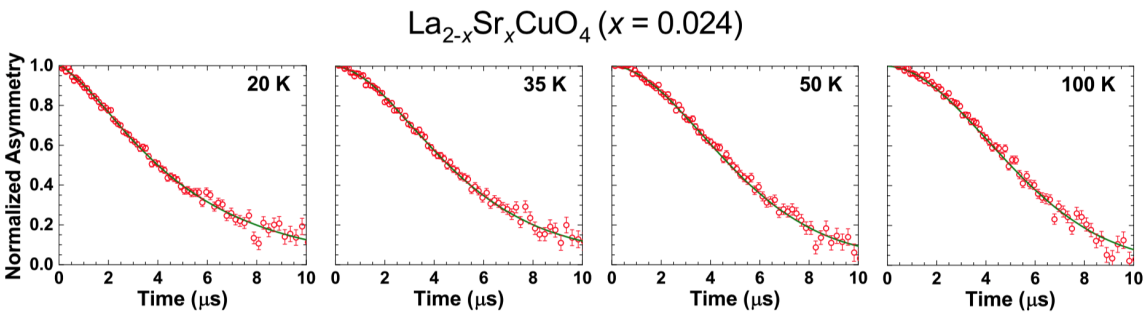

FIGURE 3.9: Analysis results of time spectra measured in $La_{2-x}Sr_xCuO_4$ for x=0.024 at various temperatures. Solid lines in the figure indicate the best−fit results by using Eq.(3.29).

spectrum was found to start to divert from Gaussian below 100 K, forming the intermediate shape [218, 217]. Our previous study on this system used Eq.(1.7) in order to discuss changes in the time spectrum on the basis of the appearance of effects of fluctuating dynamic local fields coming from surround electronic spins. Although the fitting of time spectra seemed to be good, the possibility of the trading-off effect between λ and Δ could not be removed from the results and discussions. The similar behavior of the μSR time spectrum in the paramagnetic state was also reported in other high$-T_c$ oxides [155, 190, 191], so that the origin of this change in the μSR time spectrum in the paramagnetic state has been argued to be intrinsic to understand the mechanism of the high-T_c superconductivity [210, 53, 229]. However, neither static nor dynamic properties of local magnetic fields which causes tiny changes in the μSR time spectrum has been clear due to the lack of the appropriate intermediate analysis function which can describe the time spectrum between Gaussian and Lorentzian ones. Following this situation, we applied Eq.(3.29) to μSR time spectra measured in $La_{2-x}Sr_xCuO_4$ for x=0.024 and tried to reveal the dynamic and static properties of local fields at the muon site. In this case, we can recognize the fluctuating internal field at the muon site as the relative motion against the muon within the scheme of Eq.(3.29).

Figure 3.9 shows the fitting results of some of μSR time spectra observed at about 20 K, 35 K, 50 K and 100 K in $La_{2-x}Sr_xCuO_4$ for x=0.024. Below 20 K, the temperature was too close to the magnetic transition temperature and the time spectrum becomes nearly the simple Exponential type reflecting that the fluctuating internal field from surrounding electrons became mandatory. As can be seen, the fitting results were successful proving that Eq.(3.23) well worked to describe the intermediate state of local fields including fluctuating dynamic components.

Figure 3.10 displays temperature dependences of Δ (left), a (middle) and v (right), respectively. The present analysis by using Eq.(3.29) demonstrates independent properties of each parameter. One new finding was that both Δ and v increased below around 100 K at where the μSR time spectrum started to deviate from the

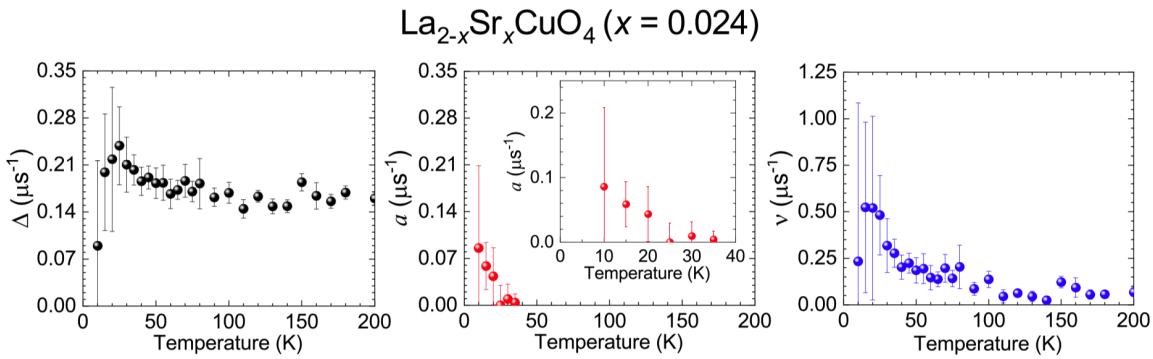

FIGURE 3.10: Temperature dependence of Δ (left), a (middle) and υ (right) obtained by the application of Eq.(3.29), respectively. Changes in Δ was different from that obtained by applying the phenomenological function of Eq.(1.7). [218]

Gaussian shape while a still keeps to be almost nothing down to around 20 K. Especially, the temperature dependence of Δ was different from that obtained in our previous results [218]. Therefore, we can finalize that changes below about 100 K in the time spectrum observed in $La_{2-x}Sr_xCuO_4$ for x=0.024 is not due to the trading-off effect between Δ and λ but due to increase of both the width of the static Gaussian distribution and fluctuating internal fields at the muon site.

Chapter 4

An approximation of the 3-dimensional Voigt Distribution to Analyze μSR Time Spectra

4.1 Introduction

Analyzing μSR time spectra can access the information of the magnetic environment of material via Larmor precession experienced by implanted muons. From field distribution approach, any material containing densely packed random static dipole magnetic moments will generate Gaussian distributed random direction fields on muon site, and the fields make the μSR time spectra perform Gaussian Kubo-Toyabe relaxation [103]. In an opposite density, interactions between localized muon spins and dilute randomly static dipole moments will show Lorentzian Kubo-Toyabe relaxation [205]. However static relaxations of μSR time spectra in some materials [108, 124] rise from not only Gaussian-distribution but also the Lorentzian-distribution in a form of convolution know as Voigt function. The presence of static Voigt-distributed internal fields had been proposed to be underlied by either the change of the nature nuclear magnetic-moments for instance the effect of isotopes [108] or the presence of low-concentration randomly static-electronic magnetic moments [124].

The initial Voigt μSR time spectra may originate from the static Gaussian fields modified by either static- or dynamic-Lorentzian relaxations [190] for a temperature interval at which thermal fluctuation plays role in magnetic dipole-moment dynamics. The two-cause can be differentiated from relations between dynamic and static parameters of internal fields in Longitudinal-field μSR experiments described by Redfield function [192]. In the former case, the dynamic fields change only the tail and dip of static lineshapes when the ratio of fluctuation rate with respect to the distribution width of static fields is less than 5 [122], and the change of initial lineshapes is created by the change of the distribution-type of static internal fields from Gaussian-type. We have shown that this scenario have well approached the μSR time spectra of $La_{2-x}Sr_xCuO_4$ ($x = 0.024$). whereas the dynamic paramater will modify the static Gaussian Kubo-Toyabe line shapes at all time interval in the latter case.

The μSR depolarization function in zero-field (ZF) due to the isotropic Voigt distribution function can be obtained analytically even the one- and three-dimensional Voigt function can be calculated only by numerical methods. This is caused by cosine Fourier transform naturally presents in the average value of ensemble Larmor precession

$$P_{KT}^{ZF} = \frac{1}{3} + \frac{2}{3}\int_0^\infty \rho(B)\cos\left(\gamma_\mu B t\right) B^2\, dB, \tag{4.1}$$

with $\rho\left(B\right)$ is a distribution function of internal fields and γ_μ is the gyromagnetic ratio of muon. Furthermore the μSR depolarization function in LF-condition due to the 3-dimensional isotropic Voigt distribution can only be performed analytically by a Kubo's formula working with Fourier transform of 1-dimensional distribution function [103]

$$\begin{aligned} P_{KT}^{LF}\left(t, B_0\right) = 1 - 2t\left(\frac{d}{dt}\left[Q\left(t\right)\right]\right)\frac{\cos\omega_0 t}{\left(\omega_0 t\right)^2} + \frac{2}{\omega_0^2}\lim_{t\to 0}\left(\frac{\frac{d}{dt}\left[Q\left(t\right)\right]}{t}\right) \\ + 2\int_0^t \frac{\sin\omega_0\tau}{\omega_0^3\tau}\frac{d}{d\tau}\left(\frac{\frac{d}{d\tau}\left[Q\left(\tau\right)\right]}{\tau}\right) d\tau, \end{aligned} \tag{4.2}$$

with $\omega_0 = \gamma_\mu B_0$ and $Q\left(t\right)$ is a Fourier transform of the 1-dimensional Voigt distribution function. The lineshapes of the Voigt Kubo-Toyabe in early time show an intermediate state between the Gaussian- and Lorentzian-relaxation, and the lineshapes exhibit a slight different in both shape and location of the dip as the time goes occurred in the ZF- and LF-conditions.

Besides Kubo's formula, another possible way to analytically calculate the average Larmor precession experienced by static muons in Voigt random fields is by approaching the Voigt distribution especially in LF-condition. Since the asymptotic functions of the Voigt function are the Gaussian- and the Lorentzian-function, the Voigt function can be approached by deconvoluting it in the form of an addition of the independent both functions with a weighting factor known as the pseudo-Voigt function [223, 178, 119, 75].

$$\rho_{G\leftrightarrow L}\left(B; a, \Delta\right) \approx n\left(a, \Delta\right)\rho_G\left(B, \Delta\right) + \left(1 - n\left(a, \Delta\right)\right)\rho_L\left(B; a\right), \tag{4.3}$$

with a and Δ are the parameters relating to the Gaussian and Lorentzian distribution widths. In one-dimensional Voigt function, the profile computation of pseudo-Voigt function to fit experimental data has an advantage in time consuming compared to Voigt-based function, but the accuracy of the pseudo-Voigt function vary among different approaches to the weighting factor with accuracy up to 1% [94]. Whereas the 3-dimensional pseudo-Voigt function and its potential practical application to fit the μSR data has never been studied, even though this scheme may provide a simple profile computation to handle more complex-type of the internal-field distribution for instance anisotropic case.

4.1.1 The 3-dimensional Voigt function of internal fields on muon site

In 3-dimensional Voigt function, the probability of stationary muons to experience the internal field $\vec{B}$ or $P\left(\vec{B}\right)$ will be a summation of all products of selecting randomly internal field according to the Gaussian probability distribution function $P\left(\vec{B_1}\right)$ and the Lorentzian probably distribution function $P\left(\vec{B_2}\right)$ with a condition $\vec{B} = \vec{B_1} + \vec{B_2}$ or

$$P\left(\vec{B} = \vec{B}_1 + \vec{B}_2\right) = \sum_{\vec{B}=\vec{B}_1+\vec{B}_2} P\left(\vec{B}_1\right) P\left(\vec{B}_2\right). \tag{4.4}$$

The definition of Eq. (5.4) for internal fields continuously distributed may be illustrated by Fig. (5.1) where the probability of muon selecting the internal field $\vec{B}$ is

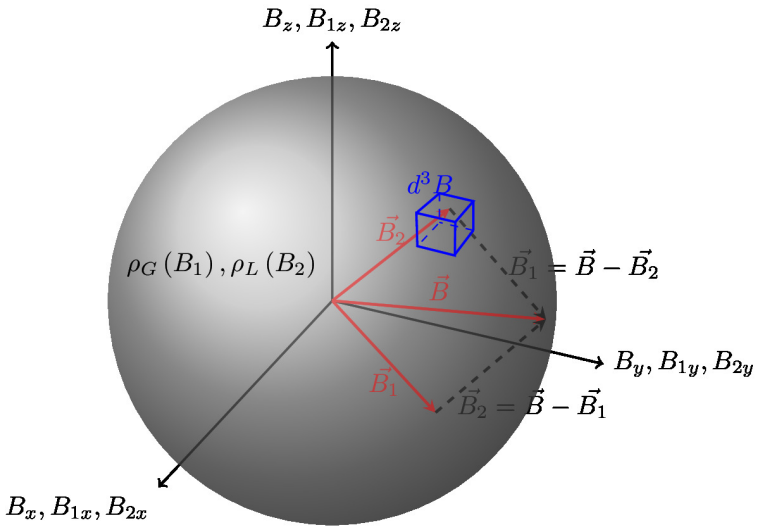

FIGURE 4.1: Probability to select internal field $\vec{B}$ according to a summation of the Gaussian $\vec{B_1}$ and Lorentzian $\vec{B_2}$ continuous random variables

obtained from an integration with respect to all possible values of $\vec{B} = \vec{B_1} + \vec{B_2}$ with the density probabilities for fields $\vec{B_1}$ and $\vec{B_2}$ represented by $\rho_G\left(\vec{B_1}\right)$ and $\rho_L\left(\vec{B_2}\right)$. So, the 3-dimensional Voigt $\rho_{G\leftrightarrow L}(B)$ defined by the convolution of the Gaussian $\rho_G(B_1)$ and the Lorentzian $\rho_L(B_2)$ distribution functions in continuous random variables as

$$\begin{aligned}
\rho_{G\leftrightarrow L}\left(\vec{B}\right) &= \left(\rho_G \circledast \rho_L\right)\left(\vec{B}\right) \\
&= \int_V \rho_G\left(\vec{B} - \vec{B}_2\right) \rho_L\left(\vec{B}_2\right) d^3B \\
&= \int_V \rho_G\left(\vec{B}_1\right) \rho_L\left(\vec{B} - \vec{B}_1\right) d^3B.
\end{aligned} \tag{4.5}$$

For an isotropic case, the 3-dimensional Gaussian and Lorentzian distribution are given by

$$\rho_G(B;a) = \frac{\gamma_\mu^3}{(2\pi)^{\frac{3}{2}}\Delta^3}\exp\left(-\frac{\gamma_\mu^2 B^2}{2\Delta^2}\right); \begin{cases} B^2 = B_x^2 + B_y^2 + B_z^2 \\ \Delta^2 = \Delta_x^2 = \Delta_y^2 = \Delta_z^2 \end{cases} \tag{4.6a}$$

$$\rho_L(B;a) = \frac{\gamma_\mu^3}{\pi^2}\frac{a}{\left(a^2+\gamma_\mu^2 B^2\right)^2}; \begin{cases} B^2 = B_x^2 + B_y^2 + B_z^2 \\ a^2 = a_x^2 = a_y^2 = a_z^2, \end{cases} \tag{4.6b}$$

so, the 3-dimensional isotropic Voigt distribution of the internal field B on muon sites defined as

$$\begin{aligned}\rho_{G\leftrightarrow L}(B;a,\Delta) &= \frac{a\gamma_\mu^6}{\Delta^3 2^{\frac{3}{2}}\pi^{\frac{7}{2}}}\int_0^\infty\int_0^{2\pi}\int_0^\pi \frac{\exp\left(-\frac{\gamma_\mu^2 B_1^2}{2\Delta^2}\right)B_1^2\sin\theta\,d\theta\,d\phi\,dB_1}{\left(a^2+\gamma_\mu^2\left|\vec{B}-\vec{B}_1\right|^2\right)^2} \\ &= \frac{2^{\frac{1}{2}}a\gamma_\mu^2}{\Delta^3\pi^{\frac{5}{2}}}\int_0^\infty \frac{\exp\left(-\frac{\gamma_\mu^2 B_1^2}{2\Delta^2}\right)B_1^2\,dB_1}{\left(\frac{a^2}{\gamma_\mu^2}+(B+B_1)^2\right)\left(\frac{a^2}{\gamma_\mu^2}+(B-B_1)^2\right)}\end{aligned} \tag{4.7a}$$

or

$$= \frac{a\gamma_\mu^4}{\Delta 2^{\frac{1}{2}}\pi^{\frac{5}{2}}}\int_0^\infty \left(\frac{\exp\left(-\frac{\gamma_\mu^2(B-B_2)^2}{2\Delta^2}\right)-\exp\left(\frac{\gamma_\mu^2(B-B_2)^2}{2\Delta^2}\right)}{\left(a^2+\gamma_\mu^2 B_2^2\right)^2}\right)\frac{B_2\,dB_2}{B}. \tag{4.7b}$$

The Gaussian and Lorentzian distributions in Eqs. (4.7a) and (4.7b) is normalized, so the Voigt distribution will also be normalized. The peak of 3-dimensional isotropic Voigt function ($B=0$) can be calculated analytically, and we obtained

$$\rho_{G\leftrightarrow L}(0;a,\Delta) = \frac{\gamma_\mu^3}{\Delta^3 2^{\frac{3}{2}}\pi^{\frac{3}{2}}}\left[\left(1-\Phi\left(\frac{a}{\sqrt{2}\Delta}\right)\right)\exp\left(-\frac{\gamma_\mu^2 B_2^2}{2\Delta^2}\right)\left(1+\frac{a^2}{\Delta^2}\right)-\frac{a\sqrt{2}}{\sqrt{\pi}\Delta}\right], \tag{4.8}$$

with $\Phi\left(\frac{a}{\sqrt{2}\Delta}\right)$ is an error function. Therefore the distribution of its orthogonal components, B_i, given by $\rho_{G\leftrightarrow L}(B_i) = (\rho_G \circledast \rho_L)(B_i)$

$$\rho_{G\leftrightarrow L}(B_i) = \frac{\gamma_\mu^2 a}{\sqrt{2}\pi^{\frac{3}{2}}}\int_{-\infty}^{+\infty}\frac{\exp\left(-\frac{\gamma_\mu^2(B_i-B_{2i})^2}{2\Delta^2}\right)}{a^2+\gamma_\mu^2 B_{2i}^2}\,dB_{2i} \tag{4.9a}$$

$$= \frac{\gamma_\mu^2 a}{\sqrt{2}\pi^{\frac{3}{2}}}\int_{-\infty}^{+\infty}\frac{\exp\left(-\frac{\gamma_\mu^2 B_{1i}^2}{2\Delta^2}\right)}{a^2+\gamma_\mu^2(B_i-B_{1i})^2}\,dB_{1i}. \tag{4.9b}$$

4.1.2 The half width at half maximum (HWHM) of the 3-dimensional Voigt function

The Voigt function in Eq. (4.6a) can be written in a dimensionless form as

$$\rho_{G\leftrightarrow L}(b,c) = c\int_0^\infty \frac{\exp\left(-y^2\right) y^2\, dy}{\left(c^2+(b+y)^2\right)\left(c^2+(b-y)^2\right)} \tag{4.10}$$

with $y = \frac{\gamma_\mu B_2}{\sqrt{2}\Delta}$, $c^2 = \frac{a^2}{2\Delta^2}$, and $b = \frac{\gamma_\mu B}{\sqrt{2}\Delta}$. Defining the HWHM of the dimensionless Voigt function as b_{HWHM}, there is an exact relation between the HWHM of Gaussian distribution $\zeta_G = \frac{\sqrt{2}\Delta\sqrt{\ln 2}}{\gamma_\mu}$ and the HWHM of the Voigt distribution $\zeta_{G\leftrightarrow L}$

$$\zeta_{G\leftrightarrow L} = \frac{\sqrt{\ln 2} b_{HWHM}}{\zeta_G}. \tag{4.11}$$

The HWHM of 3-dimensional Voigt function in Eq. (4.10) can be approached with a superposition of the Gaussian- and Lorentzian-HWHM as its asymptotic values

$$\frac{a}{\gamma_\mu} = 0 \rightarrow \zeta_{G\leftrightarrow L} = \zeta_G = \frac{\sqrt{2}\Delta\sqrt{\ln 2}}{\gamma_\mu} \tag{4.12a}$$

$$\frac{\sqrt{2}\Delta}{\gamma_\mu} = 0 \rightarrow \zeta_{G\leftrightarrow L} = \zeta_L = \frac{a}{\gamma_\mu}\sqrt{\sqrt{2}-1}, \tag{4.12b}$$

then

$$\zeta_{G\leftrightarrow L} \approx \frac{a}{\gamma_\mu}\sqrt{\sqrt{2}-1} + \frac{\sqrt{2}\Delta}{\gamma_\mu}\sqrt{\ln 2}\exp\left(\sum_n k_n c^n\right), \tag{4.12c}$$

or

$$b_{HWHM} \approx c\sqrt{\sqrt{2}-1} + \sqrt{\ln 2}\exp\left(\sum_n k_n c^n\right).$$

$\zeta_{G\leftrightarrow L}$ is obtained numerically from a relation $\rho_{G\leftrightarrow L}(b_{HWHM}, c) = \frac{1}{2}\rho_{G\leftrightarrow L}(0,c)$ with the coefficient of determination $R^2 = 1$.

$$\begin{aligned}\zeta_{G\leftrightarrow L} \cong \frac{a}{\gamma_\mu}\sqrt{\sqrt{2}-1} + \frac{\sqrt{2}\Delta}{\gamma_\mu}\sqrt{\ln 2}\exp\big(&-0.368055c + 0.005253c^2 \\ &+0.007197c^3 - 0.000855c^4\big),\end{aligned} \tag{4.13}$$

4.2 An approximation to the 3-dimensional isotropic Voigt function

The one-dimensional Voigt distribution function is lying between the Gaussian and Lorentzian distribution functions when the three distributions have the same peak and the HWHM as proposed by Kielkopf [94] and analyzed by Liu *etal*.[119]. This condition directly occurred in the surface of 3-dimensional Voigt function for the isotropic case. To obtain the weighting factor, we used a property that the three distributions normalized to $\rho_{G\leftrightarrow L}\left(B=0;a,\Delta\right)$ since they have the same peak and HWHM as proposed by Di Rocco et. al [170]. The 3-dimensional isotropic Gaussian and Lorentzian distributions with the same peak and width as the 3-dimensional isotropic Voigt distribution must be

$$\rho_G\left(B;\zeta_{G\leftrightarrow L}\right)=\rho_{G\leftrightarrow L}\left(0;a,\Delta\right)\exp\left(-\frac{\ln 2B^2}{\zeta^2_{G\leftrightarrow L}}\right) \tag{4.14a}$$

$$\rho_L\left(B;\zeta_{G\leftrightarrow L}\right)=\frac{\rho_{G\leftrightarrow L}\left(0;a,\Delta\right)\zeta^3_{G\leftrightarrow L}}{\left(\sqrt{2}-1\right)^2}\frac{\zeta_{G\leftrightarrow L}}{\left(\frac{\zeta^2_{G\leftrightarrow L}}{\left(\sqrt{2}-1\right)}+B^2\right)^2}. \tag{4.14b}$$

Treating the right and left sides of Eq. (4.3) are the equal and integrating the both side with taking account Eqs. (4.13a) and (4.13b), it is obtained

$$n\left(a,\Delta\right)=\frac{\left(\ln 2\right)^{\frac{3}{2}}\left(\left(\sqrt{2}-1\right)^{\frac{3}{2}}-\zeta^3_{G\leftrightarrow L}\pi^2\rho_{G\leftrightarrow L}\left(0;a,\Delta\right)\right)}{\rho_{G\leftrightarrow L}\left(0;a,\Delta\right)\left(\left(\sqrt{2}-1\right)^{\frac{3}{2}}\zeta^3_{G\leftrightarrow L}\pi^{\frac{3}{2}}-\left(\ln 2\right)^{\frac{3}{2}}\zeta^3_{G\leftrightarrow L}\pi^2\right)}. \tag{4.15}$$

The weighting factor has less degree of freedom since coming from deconvoluting the Voigt distribution with constraining the peak and HWHM of the Gaussian and Lorentzian distributions.

The quality of the approximation function, defined as the discrepancy between the approximation- and exact-Voigt functions normalized to the the exact Voigt function $\left(\delta\rho_{G\leftrightarrow L}=\frac{\rho^{\text{approx.}}_{G\leftrightarrow L}-\rho^{\text{exact}}_{G\leftrightarrow L}}{\rho^{\text{exact}}_{G\leftrightarrow L}}\right)$, depends on the ratio of the width-parameter Lorentzian to Gaussian distributions $\left(\frac{a}{\sqrt{2}\Delta}\right)$ where the minimum accuracy takes place around $\frac{a}{\sqrt{2}\Delta}=1$ as shown in Fig. (4.2). This is different from one-dimensional case as reported by [15] which argued the quality of the approximated function is $\frac{a}{\sqrt{2}\Delta}$-independent. The accuracy reaches minimum values around 20% but localized around the tail of the distribution function, just below the HWHM as shown in Fig. [4.2]. The minimum accuracy increases almost five times than that of one-dimensional case as reported in [170] due to the dimension number of the distribution function. There is also a significant jump of the less-accuracy when the value of $\left(\frac{a}{\sqrt{2}\Delta}\right)$ toward to the chosen minimum boundary value 0.002.

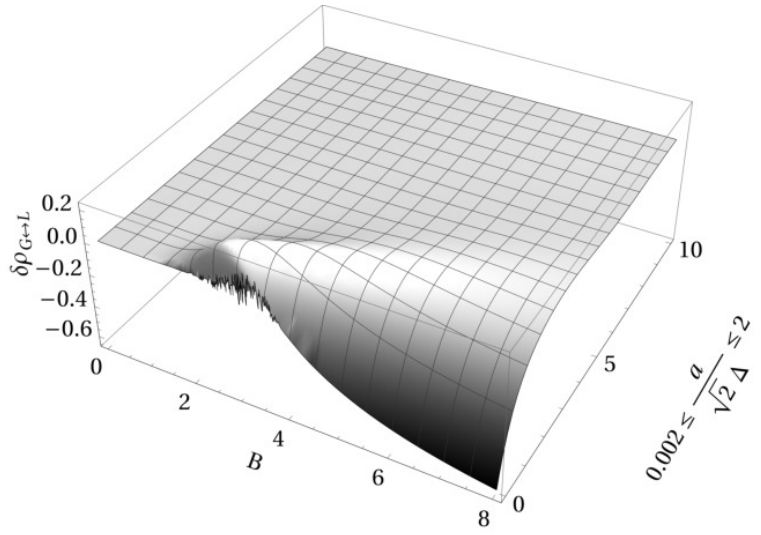

FIGURE 4.2: The quality of approximation of Voigt function compared to the exact one on a dependence of the Gaussian and Lorentzian width parameters

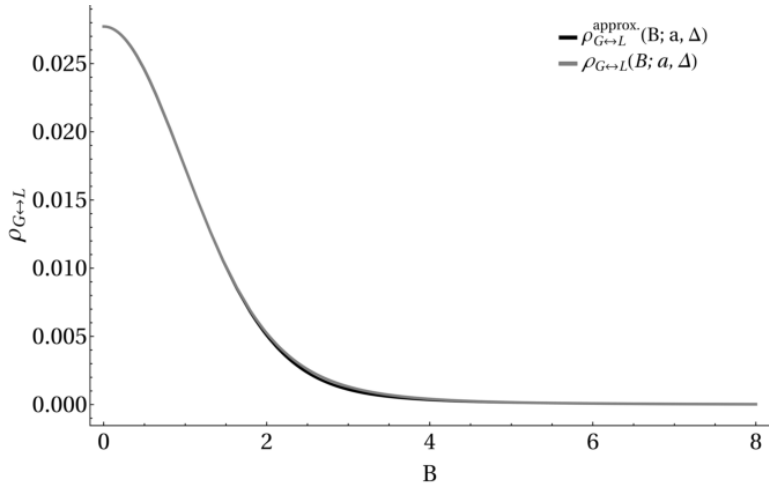

FIGURE 4.3: Plotting together the exact and the approximation Voigt functions. The deviation between two-function mostly occurred around the distribution tail

4.3 Static and dynamic relaxation functions

One of authors has considered the internal fields in our target material $La_{2-x}Sr_xCuO_4$ ($x = 0.024$) consisting of a dynamic component originating electronic magnetic moment and fluctuating fast compared to static Gaussian nuclear-dipole fields [218]. In this scheme, the dynamic- and static-fields variables can be separated into the direct product of $\exp(-\lambda t)\, G_{KT}(t;\Delta)$. The exponential function originates from the narrowing process due to a fast-field fluctuation where, in the scheme strong collision model, the relaxation rate can be written as $\lambda = \frac{2\Delta_e^2}{\nu}$, with ν is fluctuation rate and Δ_e is a parameter of the distribution width of static fields from electronic

magnetic moments. In this work, the change of initial lineshapes from Gaussian-shape is addressed to the change of distribution type of internal field on muon sites (Voigt distribution) as in [124, 109, 108], and field dynamics only modify the dip and tail of static Voigt relaxation. The muons then sense Voigt internal-field dynamics which may originate from muon diffusion or fluctuating fields. we consider two-state model and Markov process as well as the strong collision model with a single fluctuation rate in the form the second kind of Volterra integral equation

$$G\left(t,v\right)=\exp\left(-vt\right)P_{z}\left(t\right)+v\int_{0}^{t}\exp\left(-v\left(t-t'\right)\right)P_{z}\left(t-t'\right)G\left(t',v\right)\,dt', \quad (4.16)$$

with ν is either the field fluctuation rate or the muon diffusion rate, and $P_z\left(t\right)$ is the static approximated Voigt Kubo-Toyabe function.

In static random fields, the static muon spin depolarization function will be average Larmor precession $P_z(t)=\left\langle \cos^2\theta+\sin^2\theta\cos\gamma_\mu Bt\right\rangle_B$. Taking account the Eqs. (4.13a), (4.13b) and (4.14), it is obtained-approximated Voigt muon spin depolarization function in ZF-condition as

$$\begin{aligned}P_{\mu}^{ZF}\left(t\right)&=n\left(a,\Delta\right)\frac{\rho_{G\leftrightarrow L}\left(0;a,\Delta\right)\pi^{\frac{3}{2}}\zeta_{G\leftrightarrow L}^{3}}{\left(\ln 2\right)^{\frac{3}{2}}}\left(\frac{1}{3}+\frac{2}{3}\left(1-\frac{\gamma_{\mu}^{2}\zeta_{G\leftrightarrow L}^{2}t^{2}}{2\ln 2}\right)\exp\left(-\frac{\gamma_{\mu}^{2}\zeta_{G\leftrightarrow L}^{2}t^{2}}{4\ln 2}\right)\right)\\&+\left(1-n\left(a,\Delta\right)\right)\frac{\rho_{G\leftrightarrow L}\left(0;a,\Delta\right)\pi^{2}\zeta_{G\leftrightarrow L}^{3}}{\left(\sqrt{2}-1\right)^{\frac{3}{2}}}\left(\frac{1}{3}+\frac{2}{3}\left(1-\frac{\gamma_{\mu}\zeta_{G\leftrightarrow L}t}{\sqrt{\sqrt{2}-1}}\right)\exp\left(-\frac{\gamma_{\mu}\zeta_{G\leftrightarrow L}t}{\sqrt{\sqrt{2}-1}}\right)\right).\end{aligned} \quad (4.17)$$

The terms in front of round brackets are due to the Gaussian- and Lorentzian-distribution described by Eqs. (4.13a) and (4.13b) normalized to the peak of 3-dimensional isotropic Voigt distribution. The internal fields are parallel to in initial muon spin direction will contribute to a factor $\frac{1}{3}$. The weighting factor in ZF-condition in Eq. (4.14) does not change in LF-condition because the Gaussian and Lorentzian distributions are still normalized under LF-condition. We analytically calculate the average of Larmor precession in a longitudinal field B_0 due to the approximated-Voigt function,

and it holds that

$$P_{\mu}^{LF}(t) = n(a,\Delta)\frac{\rho_{G\leftrightarrow L}(0;a,\Delta)\,\pi^{\frac{3}{2}}\zeta_{G\leftrightarrow L}^{3}}{(\ln 2)^{\frac{3}{2}}}\left(1-\frac{\zeta_{G\leftrightarrow L}^{2}}{\ln 2 B_0^2}(1-\right.$$
$$\exp\left(-\frac{\gamma_{\mu}^{2}t^{2}\zeta_{G\leftrightarrow L}^{2}}{4\ln 2}\right)\cos\left(\gamma_{\mu}tB_0\right)\Big)+\frac{\zeta_{G\leftrightarrow L}^{4}\gamma_{\mu}}{2\ln^{2}2B_0^{3}}\int_0^{\tau}\exp\left(-\frac{\gamma_{\mu}^{2}\tau^{2}\zeta_{G\leftrightarrow L}^{2}}{4\ln 2}\right)$$
$$\sin\left(\gamma_{\mu}\tau B_0\right)\,d\tau\Big)+(1-n(a,\Delta))\frac{\rho_{G\leftrightarrow L}(0;a,\Delta)\,\pi^{2}\zeta_{G\leftrightarrow L}^{3}}{\left(\sqrt{2}-1\right)^{\frac{3}{2}}}(1-$$
$$\frac{\zeta_{G\leftrightarrow L}}{B_0\sqrt{\sqrt{2}-1}}J_1\left(\gamma_{\mu}B_0t\right)\exp\left(-\frac{\gamma_{\mu}\zeta_{G\leftrightarrow L}t}{\sqrt{\sqrt{2}-1}}\right)-\left(\frac{\zeta_{G\leftrightarrow L}}{B_0\sqrt{\sqrt{2}-1}}\right)^{2}$$
$$\left(J_0\left(\gamma_{\mu}B_0t\right)\exp\left(-\frac{\gamma_{\mu}\zeta_{G\leftrightarrow L}t}{\sqrt{\sqrt{2}-1}}\right)-1\right)-\left[1+\left(\frac{\zeta_{G\leftrightarrow L}}{B_0\sqrt{\sqrt{2}-1}}\right)^{2}\right]$$
$$\left.\frac{\gamma_{\mu}\zeta_{G\leftrightarrow L}}{\sqrt{\sqrt{2}-1}}\int_0^{\tau}J_0\left(\gamma_{\mu}B_0\tau\right)\exp\left(-\frac{\gamma_{\mu}\zeta_{G\leftrightarrow L}\tau}{\sqrt{\sqrt{2}-1}}\right)d\tau\right) \tag{4.18}$$

with J_1 and J_0 are the first and the zeroth order spherical bessel functions.

Figs (4.4), (4.5) and (4.6) shown the lineshapes corresponding to static muon spin depolarization function in ZF-condition $\left(\frac{\omega_0}{a}\right)=0$ and LF-condition$\left(\frac{\omega_0}{a}\right)>0$ with three-value of $\frac{a}{\sqrt{2}\Delta}$ (0.1, 1 and 5). We plotted the muon spin depolarization functions constructed from both the exact Voigt distribution (black line), see Eq. (4.26) and Eq. (4.31), and the approximation Voigt distribution of Eqs. (4.17) and (4.18) (gray line) simultaneously. The initial lineshapes and their saturate tail from the two-function overlap each other perfectly, and the the deviation only appears around the dip of lineshapes associating with the initial tail distribution as shown in Fig. (3). The deviation shows a dependence to applied field (B_0) especially at the internal-field component which parallel to the initial direction of muon spin.

The quality of approximated Voigt Kubo-Toyabe function normalized to the exact function in ZF-condition $\delta P_{\mu}^{ZF}(t)=\frac{P_{\mu}^{\text{approx.}}(t)-P_{\mu}^{\text{exact}}(t)}{P_{\mu}^{\text{exact}}(t)}$ depends the ratio of Gaussian- and Lorentzian-width parameters $\left(\frac{a}{\sqrt{2}\Delta}\right)$ and take place around the dip of the static relaxation associated with the distribution tail of internal fields. The minimum accuracy is up to 10% around the the boundary of our chosen interval $\left(\frac{a}{\sqrt{2}\Delta}\right)=1$. Whereas the accuracy of LF-condition $\delta P_{\mu}^{LF}(t;B_0)(t)=\frac{P_{\mu}^{\text{approx.}}(t;B_0)-P_{\mu}^{\text{exact}}(t;B_0)}{P_{\mu}^{\text{exact}}(t;B_0)}$ has the same behavior as ZF condition, but the applied field decreases the accuracy of fields which parallel to the initial muon direction as shown by Figs. [4.7] and [4.8].

4.4 Fitting results and Discussion

We compare the dynamic muon spin depolarization function with static function following of Eq. (4.17) to a static function based on an exact isotropic 3-dimensional

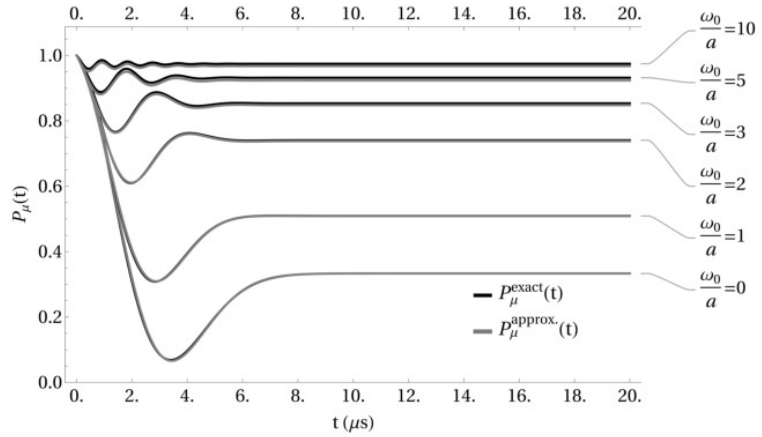

FIGURE 4.4: Muon spin depolarization functions due to static Voigt internal fields approached with mixing Gaussian and Lorentzian distributions of Eq. (4.18). The plotted function is for $\frac{a}{\sqrt{2}\Delta}$=0.1, and the $\frac{\omega_0}{a} = 0$ represent ZF-condition of Eq. (4.17)

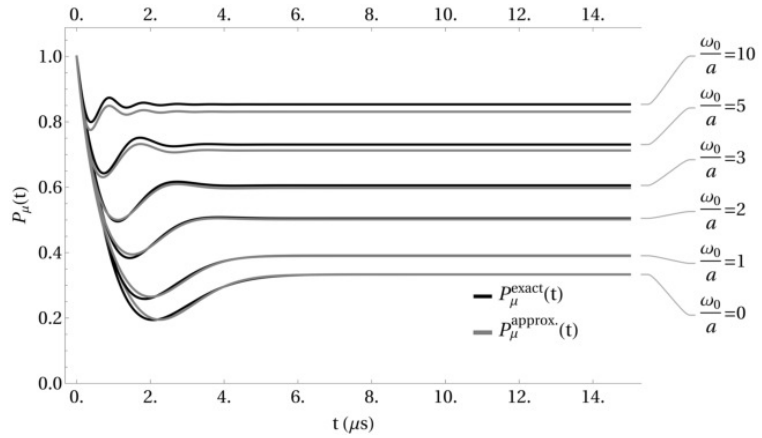

FIGURE 4.5: The muon spin depolarization function of LF-case of Eq. (4.18) $\left(\frac{\omega_0}{a} > 0\right)$ and ZF-case of Eq. (4.17) $\left(\frac{\omega_0}{a} = 0\right)$ when $\frac{a}{\sqrt{2}\Delta}$=1 corresponding to the least accuracy of the approximation

Voigt distribution. ZF μSR data in $La_{2-x}Sr_xCuO_4$ with 2.4% Sr are fitted by Eq. (4.16) with two static functions based on exact Voigt function (blue line) and approximated Voigt function (red line). Presenting the solid curves which fit to the Eq. (4.16) at the same figures, the two-lineshapes overlap each other at all temperature ranges except at 10K as shown in Fig. (4.10). The Gaussian and Loretzian distribution width parameters (Δ and a) as well as the fluctuation rate from fitting results perfectly match each other in the size reference of represented data symbols except temperature below 30K as shown in Figs. (4.11), (4.12) and (4.13). The Gaussian and Lorentzian distribution width parameters of the internal fields (Δ and a) obtained by the exact and approximation Voigt functions under 30 K has a maximum discrepancy around 0.02 μs^{-1} corresponding to 0.4 G when $\frac{a}{\sqrt{2}\Delta} = 0.09$. Whereas deviations in fluctuation parameter (ν) increases with the enhancement of Lorentzian distribution width

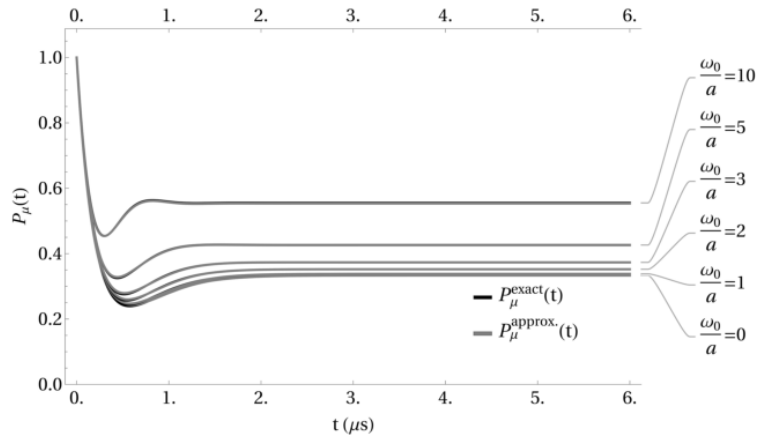

FIGURE 4.6: The muon spin depolarization function of LF-case of Eq. (4.18) $\left(\frac{\omega_0}{a} > 0\right)$ and ZF-case of (4.17) $\left(\frac{\omega_0}{a} = 0\right)$ when $\frac{a}{\sqrt{2}\Delta}$=5

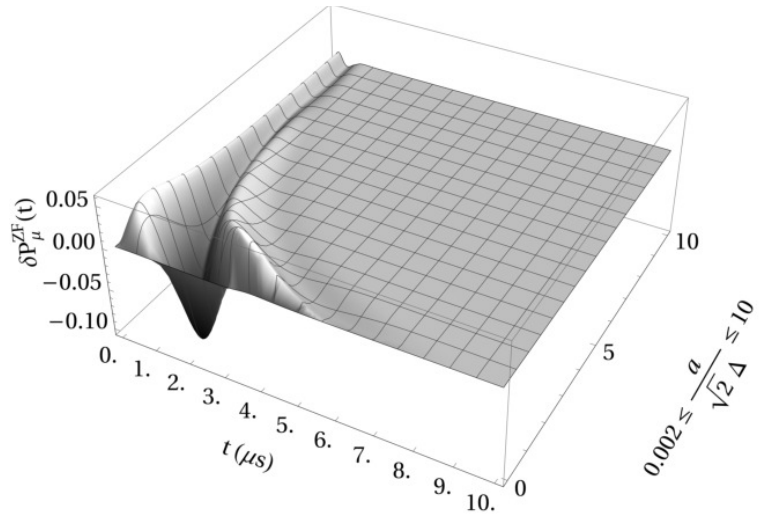

FIGURE 4.7: The quality of muon spin depolarization function from approaching Voigt distribution compared to exact Voigt distribution in the ZF-field condition as a function of $\frac{a}{\sqrt{2}\Delta}$

parameter (a) reflect the characteristic of the strong collison model where the the gradient of initial-relaxation linehapes will be taken account after each fluctuation [116]. The maximum deviation of fluctuation rate due to the exact and appromation Voigt function at the same temperature reaches around 0.06 μs^{-1} correspond to 1.2 G. The standard error of 3-fitted parameter based the approximated Voigt distribution is less than that of coming from the exact Voigt distribution reflects a strong correlation of the Gaussian and Lorentzian distribution-width parameters (a and Δ) in the approximation of Voigt function as shown in Fig. (4.2).

The initial μSR spectra of our sample show Gaussian Kubo-Toyabe relaxation from 200K, see Fig. (4.9), to 30 K as presented in Fig. (4.12) indicated by the temperature independence of Lorentzian distribution width parameter (a) which constantly tend to zero within the temperature interval from 30 K to 200K. These data describe

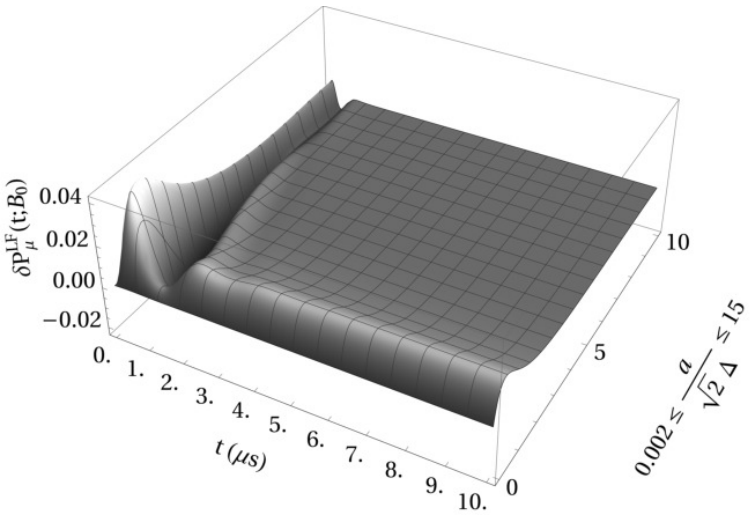

FIGURE 4.8: The quality of muon spin depolarization function from approaching Voigt distribution compared to the analysis function from the exact Voigt distribution in the LF-field condition with ratio $\frac{\omega_0}{a} = 3$. The contribution of "decoupling" field enhances with the increase of applied field ω_0 to compensate the decrease of contribution of B_x and B_y components.

the internal fields on muon site are dominated by the static Cu nuclear dipole moments above 30K. The Gaussian distribution width parameter (Δ) fluctuates at an interval temperature at which the contribution of Lorentzian distribution tend to stable describing the lattice dynamics since the Gaussian width parameter Δ only depends on the position of nuclear dipole moments [68].

The Lorentzian-distribution width parameter (a) shows a strong temperature-dependence below 30 K indicating the change of initial Gaussian lineshapes caused by the change of distribution type of internal fields on muon sites. This static origin also suggests dynamic component of internal fields has not been in fast fluctuation regime, so it constrains us from doing a separation of dynamic and static variables in the form of a direct product between Lorentzian exponential and Static Gaussian Kubo-Toyabe function as done in [216]. Furthermore the dynamic of Voigt internal field of Eq. (4.16) proposes the presence of a coupling between the nuclear dipole moments and the static Lorentzian fields instead of representing a muon-diffusion in the background of static Voigt random fields from low-temperature consideration.

The observed static Lorentzian field on muon site indicated the presence of dilute static randomly alignment of dipole moments. Quasistatic nuclear dipoles of dilute stable isotopes such as $^{87}_{38}$Sr and $^{17}_{8}$O with abundance 7% and 0.04 % respectively can be ignored since the observed Lorentzian fields shown temperature independent. The fluctuation rate of intermediate internal field ν presented in Fig. 4.13 is not in fast relaxation limit indicating the Lorentzian field may not originate from the fluctuation of order states such as SDW and orbital order fluctuations because electronic dipole moment is 3 order bigger than nuclear dipole moments.

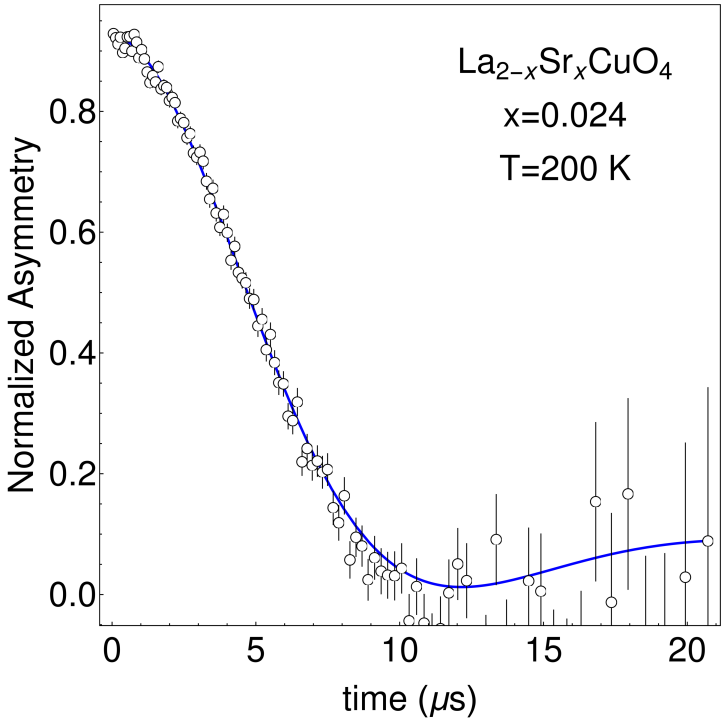

FIGURE 4.9: μSR spectra of ZF data $La_{2-x}Sr_xCuO_4$ with 2.4% Sr at 200K. The two dynamic analysis function of Eq. (4.16) with static functions based on the Voigt and the approximation Voigt distributions approach μSR data with the same lineshapes at all time interval. The dynamic and static fitted parameters from two-functions give almost the same values as presented by Figs. (4.11), (4.12), and (4.13)

Neutron scattering has observed spin glass or a short range SDW at around 20 K in this material [214]. The SDW state was also observed by μSR and NMR at lower temperature around 10 K [155]. There are two possible magnetic ground states in copper oxide plane that are RVB state and antiferromagnetism which probably underlie relations between observed SDW and the lorentzian fields. In antiferromagnetism model, the localized doped-hole in oxygen site will induce a competition between ferromagnetic interaction (copper and oxygen electron spins) and antiferromagnetic interaction (copper electron spins) and make a frustration among copper spins. The competition then will take SDW state as magnetic ground state [2]. In $La_{1.976}Sr_{0.024}CuO_4$, 2.4% holes at oxygen site will be localized at low temperature, and those dilute electronic dipoles potentially induce Lorentzian field when they freeze. We propose Copper spins at temperatures close to observed spin glass state is still frustration, and their dynamics have not entered μSR time window. Furthermore, electronic dipoles at oxygen site freeze earlier than those of copper sites before both transforming into SDW state. In RVB state, copper spins will be in a superposition of all possible singlets, and singlet excitation results quasiparticle spinon with respect to RVB ground state [174]. While doped-hole will induce holon quasiparticle in the form of zhang-rice singlet, and, in Fermi liquid star model, holon and

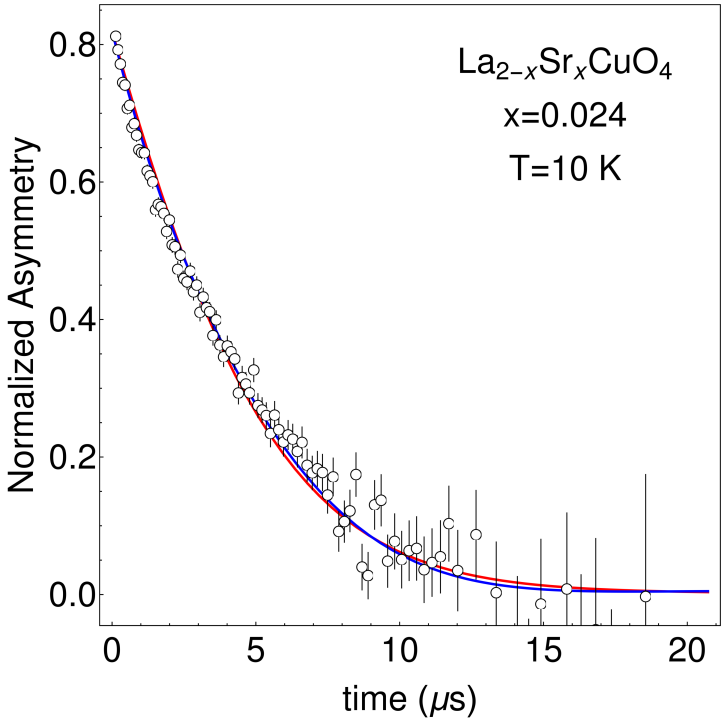

FIGURE 4.10: μSR spectra of ZF data $La_{2-x}Sr_xCuO_4$ with 2.4% Sr at 10K. The dynamic analysis function of Eq. (4.16) with the static function developed from the approximation Voigt function (red line) approaches the data with $\frac{a}{\sqrt{2}\Delta} = 0.52$ with accuracy around 5-10% of Fig. (4.7). Whereas the dynamic analysis function with the static function described by the exact Voigt distribution approached the same data with $\frac{a}{\sqrt{2}\Delta} = 0.68$

spinon are allowed to couple in order to presence of hole quasiparticle [174]. We assumed singlet formation is stable at low temperature, and spinon tends to couple with holon rather than de-excite to form singlet. In this scheme, the Lorentzian field may come from freeze of hole spin in glassy state.

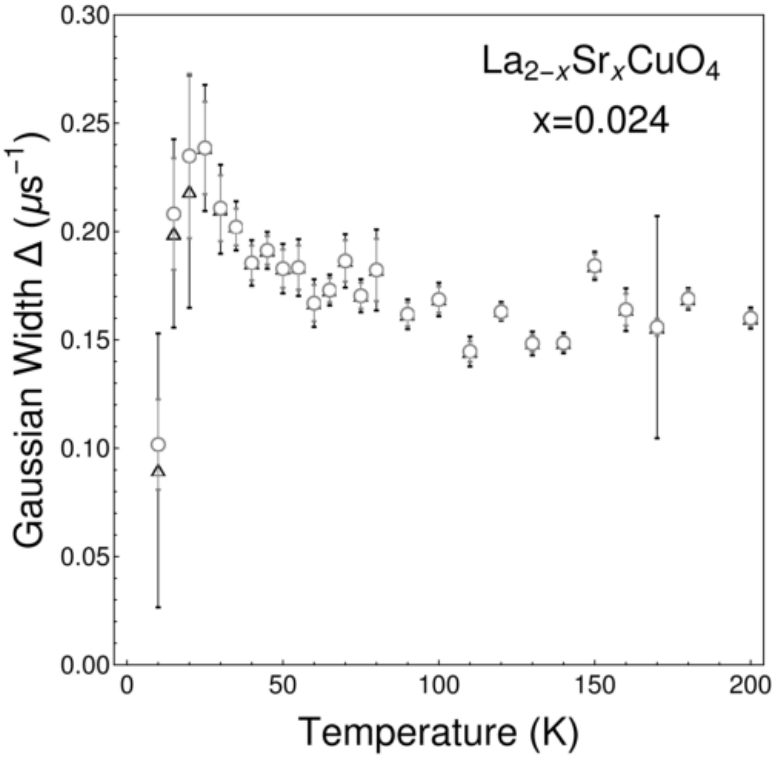

FIGURE 4.11: The temperature dependence of the Gaussian distribution-width parameter in $La_{2-x}Sr_xCuO_4$ with 2.4% Sr at ZF-condition. The unfilled triangles comes correspond to the exact Voigt distribution function, whereas the unfilled circles come from the approximation distribution function

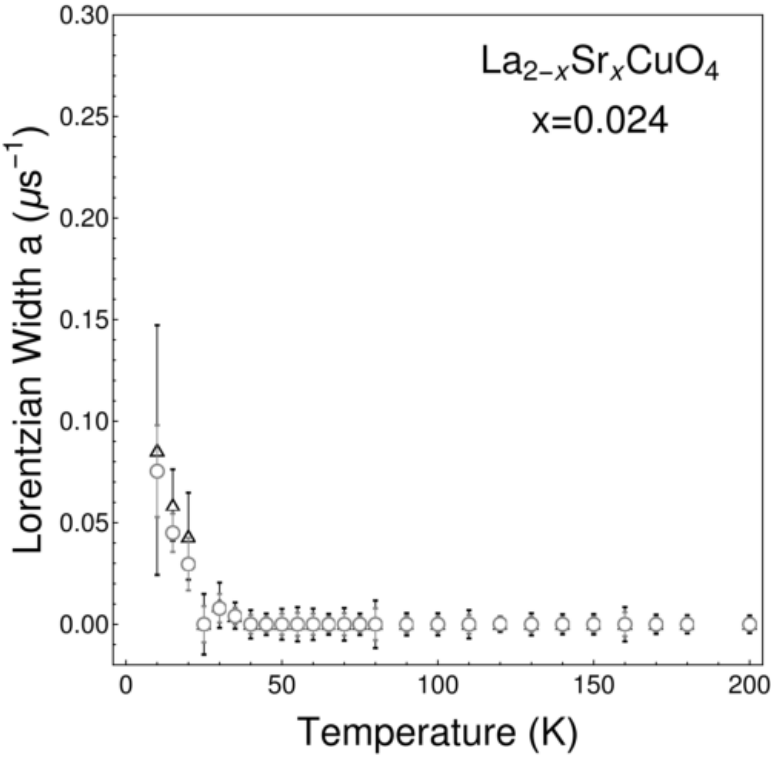

FIGURE 4.12: The temperature dependence of the Lorentzian distribution-width parameter in $La_{2-x}Sr_xCuO_4$ with 2.4% Sr at ZF-condition fitted with the dynamic muon spin depolarization function of Eq. (16) with static function in Eq. (4.16) constructed from the exact Voigt distribution (unfilled triangles) and the approximation Voigt distribution (unfilled circles)

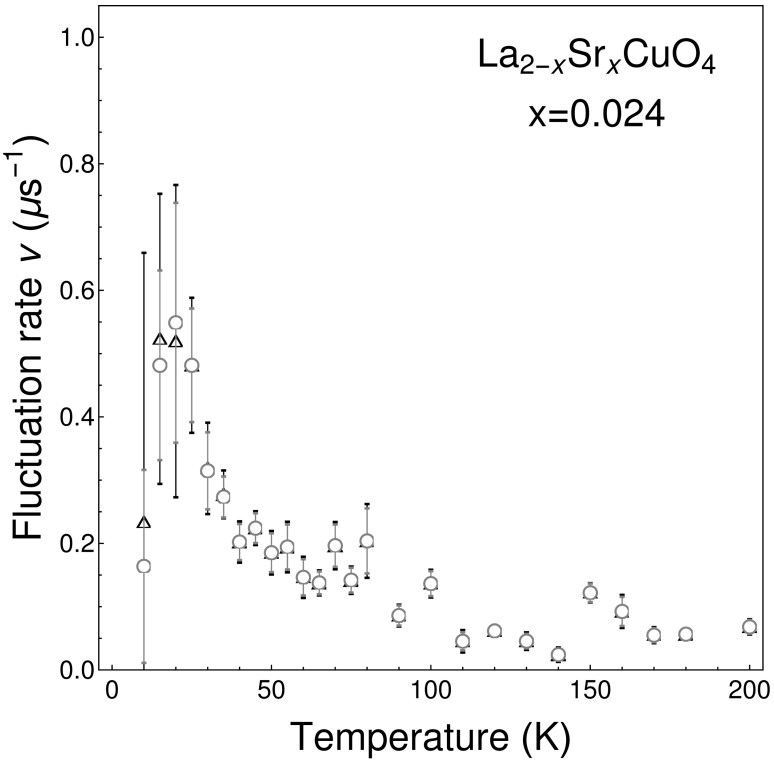

FIGURE 4.13: The temperature dependence of the fluctuation rate of internal field on muon site in $La_{2-x}Sr_xCuO_4$ with 2.4% Sr at ZF-condition fitted with the dynamic muon spin depolarization function of Eq. (16) with static function in Eq. (4.16) constructed from the exact Voigt distribution (unfilled triangles) and the approximation Voigt distribution (unfilled circles)

Chapter 5

Summary and Concluding Remarks

We derived μSR relaxation functions under crossover magnetic fields between Gaussian and Lorentzian. We gave in this report a firm basis for matching the relaxation function parameters to the field distribution. Forms of those relaxation functions were found to be a kind of extension of the Kubo-Toyabe relaxation function. We succeed to describe their relaxation function of the muon-spin polarization which was in the intermediate state between Gaussian and Lorentzian in the zero-field and in-field cases.

As demonstrations of our developed analysis equations, we applied them to real μSR data obtained in the organic molecular superconductor, λ-$(BETS)_2GaCl_4$, and the La-based high-T_c superconducting cuprates, $La_{2-x}Sr_xCuO_4$ for x=0.024 in which the intermediate μSR time spectrum was observed in the paramagnetic state. We have succeeded to reproduce time spectra by using our developed functions. This achievement can correct our previous data obtained from the applications of the phenomenological function of $\exp(-\lambda t)$ which would contain the trading-off effect between two parameters, λ and Δ. The current results and analysis equations described in this report can help to analyze the μSR data, and to discuss the physics outlook of the crossover and magnetic transition phenomenon in a clearer manner.

A convolution between Gaussian and Lorentzian PDFs representing the summation of the two random vector fields on muon site can be interpreted as the presence of two independent sources of random internal field on muon site. The Lorentzian field in $La_{1.976}Sr_{0.024}CuO_4$ may come from static randomly alignment of Localized hole spins. Whereas,low abundance of nuclear dipoles isotope may underlie the presence of Lorentzian field in λ-$(BETS)_2GaCl_4$ case.

The analysis function describing the muon spin motion in the static random fields constructed from a convolution between Gaussian and Lorentzian distributions can be analytically derived by decomposing the 3D-convolution into solvable convolution terms of Fourier transform. The mathematical expression for 3-dimensional distribution function of magnetic fields due to a 3D-convolution of Gaussian and Lorentzian PDFs is performed for the first time. Our result will not only provide a way to understand how Kubo-Formula works in ZF-experiment but

also potentially become a starting point to develop a conversion rule from one- to three-dimensional isotropic PDFs in LF-condition in order to understand how Kubo Formula work in the LF-condition. We also approach the convolution between Gaussian and Lorentzian distributions of internal field by mixing Gaussian and Lorentzian PDFs. The weighting factor as a function of Gaussian (Δ) and Lorentzian widths (a) can be found analytically from a fact that the Gaussian and Lorentzian PDFs as well as their convolution each other have the same HWHM when they have the same peak. The analysis function from a mixing of Gaussian and Lorentzian PDFs reaches an accuracy around 10% located at the dip of static analysis function in ZF-condition associated with the tail of mixing distributions, but the accuracy exponentially become better when getting away from the dip.

The fluctuation of intermediate distributed fields in the form of a convolution between Gaussian and Lorentzian fields in strong collision model will only influence the tail of static lineshapes when fluctuation rate less than its distribution width in the same trend as reported in Gaussian and Lorentzian field cases, but after the fluctuation rate vanishes the dip of static lineshapes, the narrowing effect will be controlled by a competition between Gaussian and Lorentzian fields where the increase of Lorentzian component will make the narrowing effect become weaker. Since the narrowing effect has been only studied due to the fluctuation of Gaussian and Lorentzian distributed fields, so the behavior of narrowing effect due to the fluctuation of intermediate distributed fields has become the first time to be reported. In the future study, the dynamic analysis function in the scheme of weak collision and or non-markovian models also need to be done in order to broad the application of intermediate distributed fields. Assuming that the Gaussian-field component originates from nuclear dipole moments, and Lorentzian field comes from another source associated with an order state for example freezing spin of localized holes, then the fluctuation rate of the intermediate distributed fields indicate the presence of a coupled state between the nuclear dipole moments and the order state. The fluctuation of intermediate distributed fields produce a different location of dip from an analysis function got from a direct product between an exponential and Gaussian Kubo-Toyabe functions when the fluctuation rate has not vanished the dip of static lineshapes, even though the both schemes produce the same initial relaxation. This property makes the dip location of μSR time spectra in ZF-experiment can differentiate whether the change of transition from Gaussian to Lorentzian relaxations originates from either the slowing down of electronic spin dynamic or a coupled state between nuclear spins and electronic order states. Finally, the role of nuclear spins to reveal the order state of samples need to be clarified in other cuprate-based materials.

Acknowledgements

I would like thanks to Professor Isao Watanabe, my advisor, for many suggestions and supports during my doctoral program in Hokkaido University and RIKEN. I am lucky to have a chance to study high-Tc superconductivity material using μSR spectroscopy since superconductivity in high-Tc material is a topic which still amazes and challenges our imagination. I would like to thank to Professor Masahiko Iwasaki who not only accepted me to settle at Meson Science Laboratory but also initiated a collaboration to publish a paper. I would like also to thank to Dr. Katsuhiko Ishida for his contributions and corrections to my work. I have benefited greatly from academic supports and a short discussion with Professor Atsushi Kawamoto. I would like to thank to Professor Hiroshi Amitsuka and Professor Tadashi Adachi as reviewers for discussion and suggestion. I am grateful to Hokkaido University and RIKEN for academic environment and research facilities.

I would like to acknowledge the support of Yunefit (my wife), Anjam, Zafran, Yuki and Wa Ode Kamaria (my mother). Their presence has become an unlimited backrest to my journey.

I also wish thank to Henokh Lugo for the help on mathematica and, my mate, Tomoaki Agatsuma for many discussions.

Finally, I would like to acknowledge to Watanabe's group members: Edi Suprayoga, Sungwon Yoon, Aina Adam, Saidah Sakinah, Dita Puspita, Retno Asih, Fahmi Astuti, Irwan Ramli, Julia Angle, Redo Ramadhan, Horizon Rozak, Utami Widyaiswari, Nurfadillah, Suci Winarsih and Muhammad Hanif.

References

[1] A.A. Abrikosov. "Theory of an unusual metal–insulator transition in layered high-Tc cuprates". In: *Physica C: Superconductivity and its Applications* 460-462 (2007). Proceedings of the 8th International Conference on Materials and Mechanisms of Superconductivity and High Temperature Superconductors, pp. 1–2. ISSN: 0921-4534. DOI: https://doi.org/10.1016/j.physc.2007.03.009. URL: https://www.sciencedirect.com/science/article/pii/S0921453407000846.

[2] Amnon Aharony et al. "Magnetic phase diagram and magnetic pairing in doped La_2CuO_4". In: *Phys. Rev. Lett.* 60 (13 1988), pp. 1330–1333. DOI: 10.1103/PhysRevLett.60.1330. URL: https://link.aps.org/doi/10.1103/PhysRevLett.60.1330.

[3] Hirohito Aizawa et al. "Electronic Structure Calculation and Superconductivity in λ-$(BETS)_2GaCl_4$". In: *Journal of the Physical Society of Japan* 87.9 (2018), p. 093701. DOI: 10.7566/JPSJ.87.093701. eprint: https://doi.org/10.7566/JPSJ.87.093701. URL: https://doi.org/10.7566/JPSJ.87.093701.

[4] A.S. Alexandrov and N. F. Mott. *Polarons and bipolarons*. 1st ed. Singapore: World Scientific, 1995.

[5] Andrea Allais, Debanjan Chowdhury, and Subir Sachdev. "Connecting high-field quantum oscillations to zero-field electron spectral functions in the underdoped cuprates". In: *Nat. Commun.* 5 (2014), p. 5771. DOI: https://doi.org/10.1038/ncomms6771.

[6] Andrea Allais and T. Senthil. "Loop current order and d-wave superconductivity: Some observable consequences". In: *Phys. Rev. B* 86 (4 2012), p. 045118. DOI: 10.1103/PhysRevB.86.045118. URL: https://link.aps.org/doi/10.1103/PhysRevB.86.045118.

[7] J. W. Allen et al. "Resonant photoemission study of $Nd_{2-x}Ce_xCuO_{4-y}$: Nature of electronic states near the Fermi level". In: *Phys. Rev. Lett.* 64 (5 1990), pp. 595–598. DOI: 10.1103/PhysRevLett.64.595. URL: https://link.aps.org/doi/10.1103/PhysRevLett.64.595.

[8] V. K. Anand et al. "Muon spin relaxation and inelastic neutron scattering investigations of the all-in/all-out antiferromagnet $Nd_2Hf_2O_7$". In: *Phys. Rev. B* 95 (22 2017), p. 224420. DOI: 10.1103/PhysRevB.95.224420. URL: https://link.aps.org/doi/10.1103/PhysRevB.95.224420.

[9] S. Andergassen et al. "Anomalous Isotopic Effect Near the Charge-Ordering Quantum Criticality". In: *Phys. Rev. Lett.* 87 (5 2001), p. 056401. DOI: 10.1103/PhysRevLett.87.056401. URL: https://link.aps.org/doi/10.1103/PhysRevLett.87.056401.

[10] P. W. Anderson. "The Resonating Valence Bond State in La2CuO4 and Superconductivity". In: *Science* 235.4793 (1987), pp. 1196–1198. ISSN: 0036-8075. DOI: 10.1126/science.235.4793.1196. eprint: https://science.sciencemag.org/content/235/4793/1196.full.pdf. URL: https://science.sciencemag.org/content/235/4793/1196.

[11] Yoichi Ando et al. "Electrical Resistivity Anisotropy from Self-Organized One Dimensionality in High-Temperature Superconductors". In: *Phys. Rev. Lett.* 88 (13 2002), p. 137005. DOI: 10.1103/PhysRevLett.88.137005. URL: https://link.aps.org/doi/10.1103/PhysRevLett.88.137005.

[12] Yoichi Ando et al. "Electronic Phase Diagram of High-T_c Cuprate Superconductors from a Mapping of the In-Plane Resistivity Curvature". In: *Phys. Rev. Lett.* 93 (26 2004), p. 267001. DOI: 10.1103/PhysRevLett.93.267001. URL: https://link.aps.org/doi/10.1103/PhysRevLett.93.267001.

[13] Yoichi Ando et al. "Mobility of the Doped Holes and the Antiferromagnetic Correlations in Underdoped High Tc Cuprates". In: *Phys. Rev. Lett.* 87 (1 2001), p. 017001. DOI: 10.1103/PhysRevLett.87.017001. URL: https://link.aps.org/doi/10.1103/PhysRevLett.87.017001.

[14] V. Balédent et al. "Two-Dimensional Orbital-Like Magnetic Order in the High-Temperature $La_{2-x}Sr_xCuO_4$ Superconductor". In: *Phys. Rev. Lett.* 105 (2 2010), p. 027004. DOI: 10.1103/PhysRevLett.105.027004. URL: https://link.aps.org/doi/10.1103/PhysRevLett.105.027004.

[15] Sumilan Banerjee, Shizhong Zhang, and Mohit Randeria. "Theory of quantum oscillations in the vortex-liquid state of high-Tc superconductors". In: *Nat. Commun.* 4 (2013), p. 1700. DOI: https://doi.org/10.1038/ncomms2667.

[16] J. Bardeen, L. N. Cooper, and J. R. Schrieffer. "Theory of Superconductivity". In: *Phys. Rev.* 108 (5 1957), pp. 1175–1204. DOI: 10.1103/PhysRev.108.1175. URL: https://link.aps.org/doi/10.1103/PhysRev.108.1175.

[17] Neven Barisic et al. "Universal sheet resistance and revised phase diagram of the cuprate high-temperature superconductors". In: *Proceedings of the National Academy of Sciences* 110.30 (2013), pp. 12235–12240. ISSN: 0027-8424. DOI: 10.1073/pnas.1301989110. eprint: https://www.pnas.org/content/110/30/12235.full.pdf. URL: https://www.pnas.org/content/110/30/12235.

[18] V. Barzykin and D. Pines. "Magnetic scaling in cuprate superconductors". In: *Phys. Rev. B* 52 (18 1995), pp. 13585–13600. DOI: 10.1103/PhysRevB.52.13585. URL: https://link.aps.org/doi/10.1103/PhysRevB.52.13585.

[19] Victor Barzykin and David Pines. "Universal behaviour and the two-component character of magnetically underdoped cuprate superconductors". In: *Advances in Physics* 58.1 (2009), pp. 1–65. DOI: 10.1080/00018730802567505. eprint: https://doi.org/10.1080/00018730802567505. URL: https://doi.org/10.1080/00018730802567505.

[20] J. G. Bednorz and K. A. Müller. "Possible high Tc superconductivity in the Ba-La-Cu-O system". In: *Z. Phys. B-Condensed Matter* 64 (1986), pp. 189–193. URL: https://ci.nii.ac.jp/naid/10029437834/en/.

[21] Kamran Behnia. "The Nernst effect and the boundaries of the Fermi liquid picture". In: *J. Phys.: Condens. Matter* 21 (2009), p. 113101. DOI: https://doi.org/10.1088/0953-8984/21/11/113101.

[22] Kamran Behnia and Hervé Aubin. "Nernst effect in metals and superconductors: a review of concepts and experiments". In: *Reports on Progress in Physics* 79.4 (2016), p. 046502. DOI: 10.1088/0034-4885/79/4/046502. URL: https://doi.org/10.1088/0034-4885/79/4/046502.

[23] Griff Bilbro and W. L. McMillan. "Theoretical model of superconductivity and the martensitic transformation in $A15$ compounds". In: *Phys. Rev. B* 14 (5 1976), pp. 1887–1892. DOI: 10.1103/PhysRevB.14.1887. URL: https://link.aps.org/doi/10.1103/PhysRevB.14.1887.

[24] R. J. Birgeneau et al. "Soft-phonon behavior and transport in single-crystal La_2CuO_4". In: *Phys. Rev. Lett.* 59 (12 1987), pp. 1329–1332. DOI: 10.1103/PhysRevLett.59.1329. URL: https://link.aps.org/doi/10.1103/PhysRevLett.59.1329.

[25] S J Blundell and F L Pratt. "Organic and molecular magnets". In: *Journal of Physics: Condensed Matter* 16.24 (2004), R771–R828. DOI: 10.1088/0953-8984/16/24/r03. URL: https://doi.org/10.1088/0953-8984/16/24/r03.

[26] G. S. Boebinger et al. "Insulator-to-Metal Crossover in the Normal State of $La_{2-x}Sr_xCuO_4$ Near Optimum Doping". In: *Phys. Rev. Lett.* 77 (27 1996), pp. 5417–5420. DOI: 10.1103/PhysRevLett.77.5417. URL: https://link.aps.org/doi/10.1103/PhysRevLett.77.5417.

[27] J.I. Budnick et al. "Observation of magnetic ordering in La2CuO4 by muon spin rotation spectroscopy". In: *Physics Letters A* 124.1 (1987), pp. 103–106. ISSN: 0375-9601. DOI: https://doi.org/10.1016/0375-9601(87)90382-3. URL: https://www.sciencedirect.com/science/article/pii/0375960187903823.

[28] N. Bulut, D. J. Scalapino, and S. R. White. "Comparison of Monte Carlo and diagrammatic calculations for the two-dimensional Hubbard model". In: *Phys. Rev. B* 47 (5 1993), pp. 2742–2753. DOI: 10.1103/PhysRevB.47.2742. URL: https://link.aps.org/doi/10.1103/PhysRevB.47.2742.

[29] I. A. Campbell et al. "Dynamics in canonical spin glasses observed by muon spin depolarization". In: *Phys. Rev. Lett.* 72 (8 1994), pp. 1291–1294. DOI: 10.1103/PhysRevLett.72.1291. URL: https://link.aps.org/doi/10.1103/PhysRevLett.72.1291.

[30] C. Castellani, C. Di Castro, and M. Grilli. "Singular Quasiparticle Scattering in the Proximity of Charge Instabilities". In: *Phys. Rev. Lett.* 75 (25 1995), pp. 4650–4653. DOI: 10.1103/PhysRevLett.75.4650. URL: https://link.aps.org/doi/10.1103/PhysRevLett.75.4650.

[31] C. Castellani, P. Schwab, and M. Grilli. "On Localization Effects in Underdoped Cuprates". In: *Stripes and Related Phenomena*. Ed. by Antonio Bianconi and Naurang L. Saini. 1st ed. Berlin: Springer Boston MA, 2002, pp. 361–367. ISBN: 978-0-306-46419-5. DOI: https://doi.org/10.1007/0-306-47100-0_45.

[32] Sudip Chakravarty et al. "Hidden order in the cuprates". In: *Phys. Rev. B* 63 (9 2001), p. 094503. DOI: 10.1103/PhysRevB.63.094503. URL: https://link.aps.org/doi/10.1103/PhysRevB.63.094503.

[33] C.-C. Chen et al. "Doping evolution of the oxygen *K*-edge x-ray absorption spectra of cuprate superconductors using a three-orbital Hubbard model". In: *Phys. Rev. B* 87 (16 2013), p. 165144. DOI: 10.1103/PhysRevB.87.165144. URL: https://link.aps.org/doi/10.1103/PhysRevB.87.165144.

[34] Han-Dong Chen et al. "Antiferromagnetism and Hole Pair Checkerboard in the Vortex State of High T_c Superconductors". In: *Phys. Rev. Lett.* 89 (13 2002), p. 137004. DOI: 10.1103/PhysRevLett.89.137004. URL: https://link.aps.org/doi/10.1103/PhysRevLett.89.137004.

[35] H. Y. Choi and J. M. Bok. "How to pin down the pairing interaction for high Tc superconductivity in cuprates". In: *Int. J. Mod. Phys. B* 32 (2018), p. 1840026. DOI: https://doi.org/10.1142/S021797921840026X.

[36] Andrey V. Chubukov, Subir Sachdev, and Jinwu Ye. "Theory of two-dimensional quantum Heisenberg antiferromagnets with a nearly critical ground state". In: *Phys. Rev. B* 49 (17 1994), pp. 11919–11961. DOI: 10.1103/PhysRevB.49.11919. URL: https://link.aps.org/doi/10.1103/PhysRevB.49.11919.

[37] H. Clark et al. "Superconductivity in just four pairs of $(BETS)_2GaCl_2$ molecules". In: *Nat. Nanotechnol* 5 (2010), pp. 261–265. DOI: https://doi.org/10.1038/nnano.2010.41.

[38] T. P. Croft et al. "Charge density wave fluctuations in LSCO and their competition with superconductivity". In: *Phys. Rev. B* 89 (22 2014), p. 224513. DOI: 10.1103/PhysRevB.89.224513. URL: https://link.aps.org/doi/10.1103/PhysRevB.89.224513.

[39] M R Crook and R Cywinski. "Voigtian Kubo - Toyabe muon spin relaxation". In: *Journal of Physics: Condensed Matter* 9.5 (1997), pp. 1149–1158. DOI: 10.1088/0953-8984/9/5/018. URL: https://doi.org/10.1088/0953-8984/9/5/018.

[40] O. Cyr-Choinière et al. "Pseudogap temperature T^* of cuprate superconductors from the Nernst effect". In: *Phys. Rev. B* 97 (6 2018), p. 064502. DOI: 10.1103/PhysRevB.97.064502. URL: https://link.aps.org/doi/10.1103/PhysRevB.97.064502.

[41] M. T. Czyzyk and G. A. Sawatzky. "Local-density functional and on-site correlations: The electronic structure of La_2CuO_4 and $LaCuO_3$". In: *Phys. Rev. B* 49 (20 1994), pp. 14211–14228. DOI: 10.1103/PhysRevB.49.14211. URL: https://link.aps.org/doi/10.1103/PhysRevB.49.14211.

[42] Zhehao Dai et al. "Pair-density waves, charge-density waves, and vortices in high-T_c cuprates". In: *Phys. Rev. B* 97 (17 2018), p. 174511. DOI: 10.1103/PhysRevB.97.174511. URL: https://link.aps.org/doi/10.1103/PhysRevB.97.174511.

[43] Andrea Damascelli, Zahid Hussain, and Zhi-Xun Shen. "Angle-resolved photoemission studies of the cuprate superconductors". In: *Rev. Mod. Phys.* 75 (2 2003), pp. 473–541. DOI: 10.1103/RevModPhys.75.473. URL: https://link.aps.org/doi/10.1103/RevModPhys.75.473.

[44] R. Daou et al. "Importance of phase fluctuations in superconductors with small superfluid density". In: *Nat. Phys.* 5 (2009), pp. 31–34. DOI: https://doi.org/10.1038/nphys1109.

[45] Nicolas Doiron-Leyraud et al. "Quantum oscillation and the Fermi surface in an underdoped high-T_c superconductor". In: *Nature* 447 (2007), pp. 565–568. DOI: https://doi.org/10.1038/nature05872.

[46] Gil Drachuck et al. "Comprehensive study of the spin-charge interplay in antiferromagnetic $La_{2-x}Sr_xCuO_4$". In: *Nat. Commun.* 5 (2014), p. 3390. DOI: https://doi.org/10.1038/ncomms4390.

[47] V. J. Emery. "Theory of high-T_c superconductivity in oxides". In: *Phys. Rev. Lett.* 58 (26 1987), pp. 2794–2797. DOI: 10.1103/PhysRevLett.58.2794. URL: https://link.aps.org/doi/10.1103/PhysRevLett.58.2794.

[48] V. J. Emery and S. A. Kivelson. "Importance of phase fluctuations in superconductors with small superfluid density". In: *Nature* 374 (1995), pp. 434–437. DOI: https://doi.org/10.1038/374434a0.

[49] V. J. Emery, S. A. Kivelson, and O. Zachar. "Spin-gap proximity effect mechanism of high-temperature superconductivity". In: *Phys. Rev. B* 56 (10 1997), pp. 6120–6147. DOI: 10.1103/PhysRevB.56.6120. URL: https://link.aps.org/doi/10.1103/PhysRevB.56.6120.

[50] I. Eremin et al. "Spin susceptibility and pseudogap in $YBa_2Cu_4O_8$: An approach via a charge-density-wave instability". In: *Phys. Rev. B* 56 (17 1997), pp. 11305–11311. DOI: 10.1103/PhysRevB.56.11305. URL: https://link.aps.org/doi/10.1103/PhysRevB.56.11305.

[51] Masahiro Eto and Yuhei Natsume. "Zero-Field Spin Relaxation in Systems of Highly-Anisotropic Distribution of Local Fields". In: *Progress of Theoretical Physics* 65.5 (May 1981), pp. 1760–1762. ISSN: 0033-068X. DOI: 10.1143/PTP.65.1760. eprint: https://academic.oup.com/ptp/article-pdf/65/5/1760/5255717/65-5-1760.pdf. URL: https://doi.org/10.1143/PTP.65.1760.

[52] Bradley Fahlman. *Materials Chemistry*. 1st ed. Netherlands: Springer Netherlands, 2011.

[53] B. Fauque et al. "Magnetic Order in the Pseudogap Phase of High-T_C Superconductors". In: *Phys. Rev. Lett.* 96 (19 2006), p. 197001. DOI: 10.1103/PhysRevLett.96.197001. URL: https://link.aps.org/doi/10.1103/PhysRevLett.96.197001.

[54] Eric Fawcett. "Spin density wave antiferromagnetism in chromium". In: *Rev. Mod. Phys.* 60 (1 1988), pp. 209–283. DOI: 10.1103/RevModPhys.60.209. URL: https://link.aps.org/doi/10.1103/RevModPhys.60.209.

[55] A. T. Fiory. "Muon-spin relaxation in systems of dilute dipolar impurities: Numerical treatment of fluctuations". In: *Hyperfine Interact.* 8 (1981), pp. 777–780. DOI: https://doi.org/10.1007/BF01037561.

[56] P. Fournier. "T and infinite-layer electron-doped cuprates". In: *Physica C: Superconductivity and its Applications* 514 (2015). Superconducting Materials: Conventional, Unconventional and Undetermined, pp. 314–338. ISSN: 0921-4534. DOI: https://doi.org/10.1016/j.physc.2015.02.036. URL: https://www.sciencedirect.com/science/article/pii/S0921453415000635.

[57] Masayoshi Fujihala et al. "Possible Tomonaga-Luttinger spin liquid state in the spin-1/2 inequilateral diamond-chain compound $K_3Cu_3AlO_2(SO_4)_4$". In: *Sci. Rep.* 7 (2017), p. 16785. DOI: https://doi.org/10.1038/s41598-017-16935-9.

[58] Shigeki Fujiyama et al. "Anomalous Spin Excitation in the Metallic State of $La_{2-x}Sr_xCuO_4$ Observed by Cu NQR". In: *Journal of the Physical Society of Japan* 66.9 (1997), pp. 2864–2869. DOI: 10.1143/JPSJ.66.2864. eprint: https://doi.org/10.1143/JPSJ.66.2864. URL: https://doi.org/10.1143/JPSJ.66.2864.

[59] Peter Fulde and Richard A. Ferrell. "Superconductivity in a Strong Spin-Exchange Field". In: *Phys. Rev.* 135 (3A 1964), A550–A563. DOI: 10.1103/PhysRev.135.A550. URL: https://link.aps.org/doi/10.1103/PhysRev.135.A550.

[60] Richard L. Garwin, Leon M. Lederman, and Marcel Weinrich. "Observations of the Failure of Conservation of Parity and Charge Conjugation in Meson Decays: the Magnetic Moment of the Free Muon". In: *Phys. Rev.* 105 (4 1957), pp. 1415–1417. DOI: 10.1103/PhysRev.105.1415. URL: https://link.aps.org/doi/10.1103/PhysRev.105.1415.

[61] L. P. Gorkov and A. V. Sokol. "Phase stratification of an electron liquid in the new superconductors". In: *JETP Lett.* 46 (1987), p. 420. DOI: http://jetpletters.ru/ps/1231/article_18602.shtml.

[62] L. P. Gorkov and G. B. Teitelbaum. "Two regimes in conductivity and the Hall coefficient of underdoped cuprates in strong magnetic fields". In: *Journal of Physics: Condensed Matter* 26.4 (2014), p. 042202. DOI: 10.1088/0953-8984/26/4/042202. URL: https://doi.org/10.1088/0953-8984/26/4/042202.

[63] K. Gorny et al. "Magnetic Field Independence of the Spin Gap in $YBa_2Cu_3O_{7-ffi}$". In: *Phys. Rev. Lett.* 82 (1 1999), pp. 177–180. DOI: 10.1103/PhysRevLett.82.177. URL: https://link.aps.org/doi/10.1103/PhysRevLett.82.177.

[64] T.P. Gorringe and D.W. Hertzog. "Precision muon physics". In: *Progress in Particle and Nuclear Physics* 84 (2015), pp. 73–123. ISSN: 0146-6410. DOI: https://doi.org/10.1016/j.ppnp.2015.06.001. URL: https://www.sciencedirect.com/science/article/pii/S0146641015000435.

[65] M. Hamidian et al. "Detection of a Cooper-pair density wave in $Bi_2Sr_2CaCu_2O_{8+x}$". In: *Nature* 532 (2016). DOI: https://doi.org/10.1038/nature17411.

[66] Makoto Hashimoto et al. "Energy gaps in high-transition-temperature cuprate superconductors". In: *Nat. phys.* 10 (2014), pp. 483–495. DOI: https://doi.org/10.1038/nphys3009.

[67] M. Hasimoto. "Photoemission Study of Single-Layer Cuprate High-Temperature Superconductors". PhD thesis. University of Tokyo, 2007.

[68] R. S. Hayano et al. "Zero-and low-field spin relaxation studied by positive muons". In: *Phys. Rev. B* 20 (3 1979), pp. 850–859. DOI: 10.1103/PhysRevB.20.850. URL: https://link.aps.org/doi/10.1103/PhysRevB.20.850.

[69] R. H. He et al. "Doping dependence of the (π, π) shadow band in La-based cuprates studied by angle-resolved photoemission spectroscopy". In: *New Journal of Physics* 13.1 (2011), p. 013031. DOI: 10.1088/1367-2630/13/1/013031. URL: https://doi.org/10.1088/1367-2630/13/1/013031.

[70] Haruhiro Hiraka et al. "Spin Fluctuations in the Underdoped High-Tc Cuprate $La_{1.93}Sr_{0.07}CuO_4$". In: *Journal of the Physical Society of Japan* 70.3 (2001), pp. 853–858. DOI: 10.1143/JPSJ.70.853. eprint: https://doi.org/10.1143/JPSJ.70.853. URL: https://doi.org/10.1143/JPSJ.70.853.

[71] Hideo Hosono et al. "Exploration of new superconductors and functional materials, and fabrication of superconducting tapes and wires of iron pnictides". In: *Science and Technology of Advanced Materials* 16.3 (2015). PMID: 27877784, p. 033503. DOI: 10.1088/1468-6996/16/3/033503. eprint: https://doi.org/10.1088/1468-6996/16/3/033503. URL: https://doi.org/10.1088/1468-6996/16/3/033503.

[72] Chisa Hotta. "Classification of Quasi-Two Dimensional Organic Conductors Based on a New Minimal Model". In: *Journal of the Physical Society of Japan* 72.4 (2003), pp. 840–853. DOI: 10.1143/JPSJ.72.840. eprint: https://doi.org/10.1143/JPSJ.72.840. URL: https://doi.org/10.1143/JPSJ.72.840.

[73] J. Hsiao, G. J. Martyna, and D. M. Newns. "Phase Diagram of Cuprate High-Temperature Superconductors Described by a Field Theory Based on Anharmonic Oxygen Degrees of Freedom". In: *Phys. Rev. Lett.* 114 (10 2015), p. 107001. DOI: 10.1103/PhysRevLett.114.107001. URL: https://link.aps.org/doi/10.1103/PhysRevLett.114.107001.

[74] S Hüfner et al. "Two gaps make a high-temperature superconductor?" In: *Reports on Progress in Physics* 71.6 (2008), p. 062501. DOI: 10.1088/0034-4885/71/6/062501. URL: https://doi.org/10.1088/0034-4885/71/6/062501.

[75] T. Ida, M. Ando, and H. Toraya. "Extended pseudo-Voigt function for approximating the Voigt profile". In: *Journal of Applied Crystallography* 33.6 (2000), pp. 1311–1316. DOI: 10.1107/S0021889800010219. URL: https://doi.org/10.1107/S0021889800010219.

[76] Shusaku Imajo et al. "Gap Symmetry of the Organic Superconductor λ-$(BETS)_2GaCl_4$ Determined by Magnetic-Field-Angle-Resolved Heat Capacity". In: *Journal of the Physical Society of Japan* 88.2 (2019), p. 023702. DOI: 10.7566/JPSJ.88.023702. eprint: https://doi.org/10.7566/JPSJ.88.023702. URL: https://doi.org/10.7566/JPSJ.88.023702.

[77] Shusaku Imajo et al. "Thermodynamic Evidence of d-Wave Superconductivity of the Organic Superconductor λ-$(BETS)_2GaCl_4$". In: *Journal of the Physical Society of Japan* 85.4 (2016), p. 043705. DOI: 10.7566/JPSJ.85.043705. eprint: https://doi.org/10.7566/JPSJ.85.043705. URL: https://doi.org/10.7566/JPSJ.85.043705.

[78] D. S. Inosov et al. "Crossover from weak to strong pairing in unconventional superconductors". In: *Phys. Rev. B* 83 (21 2011), p. 214520. DOI: 10.1103/PhysRevB.83.214520. URL: https://link.aps.org/doi/10.1103/PhysRevB.83.214520.

[79] K. Ishida et al. "Diffusion Properties of the Muon-Produced Soliton in trans-Polyacetylene". In: *Phys. Rev. Lett.* 55 (19 1985), pp. 2009–2012. DOI: 10.1103/PhysRevLett.55.2009. URL: https://link.aps.org/doi/10.1103/PhysRevLett.55.2009.

[80] Takayuki Ishida, Yoshitomo Okamura, and Isao Watanabe. "Long-range order in the one-dimensional cobalt(II)-radical coordination polymer magnet probed by muon-spin rotation and relaxation". In: *Inorganic chemistry* 48.15 (2009), pp. 7012–7014. ISSN: 0020-1669. DOI: 10.1021/ic9009948. URL: https://doi.org/10.1021/ic9009948.

[81] Y. Itoh et al. "Pseudo-spin-gap and slow spin fluctuation in $La_{2-x}Sr_xCuO_4$ ($x = 0.13$ and 0.18) via ^{63}Cu and ^{139}La nuclear quadrupole resonance". In: *Phys. Rev. B* 69 (18 2004), p. 184503. DOI: 10.1103/PhysRevB.69.184503. URL: https://link.aps.org/doi/10.1103/PhysRevB.69.184503.

[82] Akira Iyo et al. "Tc vs n Relationship for Multilayered High-Tc Superconductors". In: *Journal of the Physical Society of Japan* 76.9 (2007), p. 094711. DOI: 10.1143/JPSJ.76.094711. eprint: https://doi.org/10.1143/JPSJ.76.094711. URL: https://doi.org/10.1143/JPSJ.76.094711.

[83] H. Jacobsen et al. "Neutron scattering study of spin ordering and stripe pinning in superconducting $La_{1.93}Sr_{0.07}CuO_4$". In: *Phys. Rev. B* 92 (17 2015), p. 174525. DOI: 10.1103/PhysRevB.92.174525. URL: https://link.aps.org/doi/10.1103/PhysRevB.92.174525.

[84] D. C. Johnston. "Stretched exponential relaxation arising from a continuous sum of exponential decays". In: *Phys. Rev. B* 74 (18 2006), p. 184430. DOI: 10.1103/PhysRevB.74.184430. URL: https://link.aps.org/doi/10.1103/PhysRevB.74.184430.

[85] D. C. Johnston et al. "Influence of oxygen defects on the physical properties of La_2CuO_{4-y}". In: *Phys. Rev. B* 36 (7 1987), pp. 4007–4010. DOI: 10.1103/PhysRevB.36.4007. URL: https://link.aps.org/doi/10.1103/PhysRevB.36.4007.

[86] R. Kadono et al. "Quantum diffusion of positive muons in copper". In: *Phys. Rev. B* 39 (1 1989), pp. 23–41. DOI: 10.1103/PhysRevB.39.23. URL: https://link.aps.org/doi/10.1103/PhysRevB.39.23.

[87] Takashi Kajiwara et al. "Direct Observation of the Ground-Spin Alignment of Fe(II)-Fe(III) Single-Chain Magnet by Muon-Spin Relaxation". In: *Journal of the American Chemical Society* 129.41 (2007). PMID: 17887756, pp. 12360–12361. DOI: 10.1021/ja0741877. eprint: https://doi.org/10.1021/ja0741877. URL: https://doi.org/10.1021/ja0741877.

[88] Hiroshi Kamimura et al. *Theory of Copper Oxide Superconductors*. 1st ed. Berlin: Springer-Verlag Berlin Heidelberg, 2005. ISBN: 978-3-540-25189-7. DOI: 10.1007/3-540-27632-7.

[89] A. Kampf and J. R. Schrieffer. "Pseudogaps and the spin-bag approach to high-T_c superconductivity". In: *Phys. Rev. B* 41 (10 1990), pp. 6399–6408. DOI: 10.1103/PhysRevB.41.6399. URL: https://link.aps.org/doi/10.1103/PhysRevB.41.6399.

[90] M. A. Kastner et al. "Magnetic, transport, and optical properties of monolayer copper oxides". In: *Rev. Mod. Phys.* 70 (3 1998), pp. 897–928. DOI: 10.1103/RevModPhys.70.897. URL: https://link.aps.org/doi/10.1103/RevModPhys.70.897.

[91] Ribhu K. Kaul et al. "Hole dynamics in an antiferromagnet across a deconfined quantum critical point". In: *Phys. Rev. B* 75 (23 2007), p. 235122. DOI: 10.1103/PhysRevB.75.235122. URL: https://link.aps.org/doi/10.1103/PhysRevB.75.235122.

[92] B. Keimer et al. "From quantum matter to high-temperature superconductivity in copper oxides". In: *Nature* 518 (2015), pp. 179–186. DOI: https://doi.org/10.1038/nature14165.

[93] B. Keimer et al. "Magnetic excitations in pure, lightly doped, and weakly metallic La_2CuO_4". In: *Phys. Rev. B* 46 (21 1992), pp. 14034–14053. DOI: 10.1103/PhysRevB.46.14034. URL: https://link.aps.org/doi/10.1103/PhysRevB.46.14034.

[94] John F. Kielkopf. "New approximation to the Voigt function with applications to spectral-line profile analysis". In: *J. Opt. Soc. Am.* 63.8 (1973), pp. 987–995. DOI: 10.1364/JOSA.63.000987. URL: http://www.osapublishing.org/abstract.cfm?URI=josa-63-8-987.

[95] Don H. Kim. "Aspects of spin-charge separation in high Tc cuprates". PhD thesis. Massachusetts Institute of Technology, 1998.

[96] S. A. Kivelson, E. Fradkin, and V. J. Emery. "Electronic liquid-crystal phases of a doped Mott insulator". In: *Nature* 393 (1998), pp. 550–553. DOI: https://doi.org/10.1038/31177.

[97] Hayao Kobayashi et al. "New organic superconductor, λ-$(BETS)_2GaCl_4$ and metal-insulator transition of BETS conductor with magnetic anions (BETS=bis(ethlenedithio)tetrasel
In: *Synthetic Metals* 70.1 (1995). Proceedings of the International Conference on Science and Technology of Synthetic Metals, pp. 867–870. ISSN: 0379-6779. DOI: https://doi.org/10.1016/0379-6779(94)02683-P. URL: https://www.sciencedirect.com/science/article/pii/037967799402683P.

[98] T. Kobayashi and A. Kawamoto. "Evidence of antiferromagnetic fluctuation in the unconventional superconductor λ-$(BETS)_2GaCl_4$ by ^{13}C NMR". In: *Phys. Rev. B* 96 (12 2017), p. 125115. DOI: 10.1103/PhysRevB.96.125115. URL: https://link.aps.org/doi/10.1103/PhysRevB.96.125115.

[99] T. Kobayashi et al. "Unconventional superconductivity in λ-$(BETS)_2GaCl_4$ probed by ^{13}C NMR". In: *Phys. Rev. B* 102 (12 2020), p. 121106. DOI: 10.1103/PhysRevB.102.121106. URL: https://link.aps.org/doi/10.1103/PhysRevB.102.121106.

[100] M. Kofu et al. "Hidden Quantum Spin-Gap State in the Static Stripe Phase of High-Temperature $La_{2-x}Sr_xCuO_4$ Superconductors". In: *Phys. Rev. Lett.* 102 (4 2009), p. 047001. DOI: 10.1103/PhysRevLett.102.047001. URL: https://link.aps.org/doi/10.1103/PhysRevLett.102.047001.

[101] Seiki Komiya and Yoichi Ando. "Electron localization in $La_{2-x}Sr_xCuO_4$ and the role of stripes". In: *Phys. Rev. B* 70 (6 2004), p. 060503. DOI: 10.1103/PhysRevB.70.060503. URL: https://link.aps.org/doi/10.1103/PhysRevB.70.060503.

[102] A. A. Kordyuk. "Pseudogap from ARPES experiment: Three gaps in cuprates and topological superconductivity (Review Article)". In: *Low Temperature Physics* 41.5 (2015), pp. 319–341. DOI: 10.1063/1.4919371. eprint: https://doi.org/10.1063/1.4919371. URL: https://doi.org/10.1063/1.4919371.

[103] R. Kubo. "A stochastic theory of spin relaxation". In: *Hyperfine Interac.* 8 (1981), pp. 731–738. DOI: https://doi.org/10.1007/BF01037553.

[104] R. Kubo and T. Toyabe. "A stochastic model for low field resonance and relaxation". In: *Magnetic resonance and relaxation*. Ed. by R. Blinc. 1st ed. Vol. 1. 3. Amsterdam: North-Holland, 1967. Chap. 10, p. 824.

[105] F. Laliberté et al. "Fermi-surface reconstruction by stripe order in cuprate superconductors". In: *Nat. Commun.* 2 (2011), p. 432. DOI: https://doi.org/10.1038/ncomms1440.

[106] Christopher Lane et al. "Antiferromagnetic ground state of La_2CuO_4: A parameter-free ab initio description". In: *Phys. Rev. B* 98 (12 2018), p. 125140. DOI: 10.1103/PhysRevB.98.125140. URL: https://link.aps.org/doi/10.1103/PhysRevB.98.125140.

[107] A. I. Larkin and Y. N. Ovchinnikov. In: *Sov. Phys. JETP* 20 (1965), pp. 762–769.

[108] M. I. Larkin et al. "Crossover from Dilute to Majority Spin Freezing in Two Leg Ladder System $Sr(Cu,Zn)_2O_3$". In: *Phys. Rev. Lett.* 85 (9 2000), pp. 1982–1985. DOI: 10.1103/PhysRevLett.85.1982. URL: https://link.aps.org/doi/10.1103/PhysRevLett.85.1982.

[109] M.I. Larkin et al. "Exponential field distribution in SrCu1-xZnx2O3". In: *Physica B: Condensed Matter* 289-290 (2000), pp. 153–156. DOI: https://doi.org/10.1016/S0921-4526(00)00337-9.

[110] C. H. Lee et al. "Spin pseudogap in $La_{2-x}Sr_xCuO_4$ studied by neutron scattering". In: *Phys. Rev. B* 67 (13 2003), p. 134521. DOI: 10.1103/PhysRevB.67.134521. URL: https://link.aps.org/doi/10.1103/PhysRevB.67.134521.

[111] Chul-Ho Lee et al. "Energy Spectrum of Spin Fluctuations in Superconducting $La_{2-x}Sr_xCuO_4$ ($0.10 \leq x \leq 0.25$)". In: *Journal of the Physical Society of Japan* 69.4 (2000), pp. 1170–1176. DOI: 10.1143/JPSJ.69.1170. eprint: https://doi.org/10.1143/JPSJ.69.1170. URL: https://doi.org/10.1143/JPSJ.69.1170.

[112] Patrick A. Lee. "Amperean Pairing and the Pseudogap Phase of Cuprate Superconductors". In: *Phys. Rev. X* 4 (3 2014), p. 031017. DOI: 10.1103/PhysRevX.4.031017. URL: https://link.aps.org/doi/10.1103/PhysRevX.4.031017.

[113] Patrick A. Lee, Naoto Nagaosa, and Xiao-Gang Wen. "Doping a Mott insulator: Physics of high-temperature superconductivity". In: *Rev. Mod. Phys.* 78 (1 2006), pp. 17–85. DOI: 10.1103/RevModPhys.78.17. URL: https://link.aps.org/doi/10.1103/RevModPhys.78.17.

[114] T. D. Lee and C. N. Yang. "Question of Parity Conservation in Weak Interactions". In: *Phys. Rev.* 104 (1 1956), pp. 254–258. DOI: 10.1103/PhysRev.104.254. URL: https://link.aps.org/doi/10.1103/PhysRev.104.254.

[115] A. Legros et al. "Universal T-linear resistivity and Planckian dissipation in overdoped cuprates". In: *Nat. Phys.* 15 (2019), pp. 142–147. DOI: https://doi.org/10.1038/s41567-018-0334-2.

[116] M. Leon. "Models for μ^2 depolarization in spin glasses for zero external field". In: *Hyperfine Interact.* 8 (1981), pp. 781–783. DOI: https://doi.org/10.1007/BF01037562.

[117] Shiliang Li et al. "Quantum spin excitations through the metal-to-insulator crossover in $YBa_2Cu_3O_{6+y}$". In: *Phys. Rev. B* 77 (1 2008), p. 014523. DOI: 10.1103/PhysRevB.77.014523. URL: https://link.aps.org/doi/10.1103/PhysRevB.77.014523.

[118] O. J. Lipscombe et al. "Emergence of Coherent Magnetic Excitations in the High Temperature Underdoped $La_{2-x}Sr_xCuO_4$ Superconductor at Low Temperatures". In: *Phys. Rev. Lett.* 102 (16 2009), p. 167002. DOI: 10.1103/PhysRevLett.102.167002. URL: https://link.aps.org/doi/10.1103/PhysRevLett.102.167002.

[119] Yuyan Liu et al. "Simple empirical analytical approximation to the Voigt profile". In: *J. Opt. Soc. Am. B* 18.5 (2001), pp. 666–672. DOI: 10.1364/JOSAB.18.000666. URL: http://josab.osa.org/abstract.cfm?URI=josab-18-5-666.

[120] Hilbert v. Lohneysen et al. "Fermi-liquid instabilities at magnetic quantum phase transitions". In: *Rev. Mod. Phys.* 79 (3 2007), pp. 1015–1075. DOI: 10.1103/RevModPhys.79.1015. URL: https://link.aps.org/doi/10.1103/RevModPhys.79.1015.

[121] J S Lord. "Muon methods for studying nanomagnetism". In: *Journal of Physics: Conference Series* 17 (2005), pp. 81–86. DOI: 10.1088/1742-6596/17/1/014. URL: https://doi.org/10.1088/1742-6596/17/1/014.

[122] B. W. Lovett et al. "Spin fluctuations in the spin-Peierls compound $MEM(TCNQ)_2$ studied using muon spin relaxation". In: *Phys. Rev. B* 61 (18 2000), pp. 12241–12248. DOI: 10.1103/PhysRevB.61.12241. URL: https://link.aps.org/doi/10.1103/PhysRevB.61.12241.

[123] G. J. MacDougall et al. "Absence of Broken Time-Reversal Symmetry in the Pseudogap State of the High Temperature $La_{2-x}Sr_xCuO_4$ Superconductor from Muon-Spin-Relaxation Measurements". In: *Phys. Rev. Lett.* 101 (1 2008), p. 017001. DOI: 10.1103/PhysRevLett.101.017001. URL: https://link.aps.org/doi/10.1103/PhysRevLett.101.017001.

[124] A. Maisuradze et al. "Evidence for time-reversal symmetry breaking in superconducting $PrPt_4Ge_{12}$". In: *Phys. Rev. B* 82 (2 2010), p. 024524. DOI: 10.1103/PhysRevB.82.024524. URL: https://link.aps.org/doi/10.1103/PhysRevB.82.024524.

[125] Efstratios Manousakis. "The spin-half Heisenberg antiferromagnet on a square lattice and its application to the cuprous oxides". In: *Rev. Mod. Phys.* 63 (1 1991), pp. 1–62. DOI: 10.1103/RevModPhys.63.1. URL: https://link.aps.org/doi/10.1103/RevModPhys.63.1.

[126] Martin Mansson and Jun Sugiyama. "Muon-spin relaxation study on Li- and Na-diffusion in solids". In: *Physica Scripta* 88.6 (2013), p. 068509. DOI: 10.1088/0031-8949/88/06/068509. URL: https://doi.org/10.1088/0031-8949/88/06/068509.

[127] T. E. Mason et al. "New Magnetic Coherence Effect in Superconducting $La_{2-x}Sr_xCuO_4$". In: *Phys. Rev. Lett.* 77 (8 1996), pp. 1604–1607. DOI: 10.1103/PhysRevLett.77.1604. URL: https://link.aps.org/doi/10.1103/PhysRevLett.77.1604.

[128] M. Matsuda et al. "Magnetic Dispersion of the Diagonal Incommensurate Phase in Lightly Doped $La_{2-x}Sr_xCuO_4$". In: *Phys. Rev. Lett.* 101 (19 2008), p. 197001. DOI: 10.1103/PhysRevLett.101.197001. URL: https://link.aps.org/doi/10.1103/PhysRevLett.101.197001.

[129] Masahiro Matsumura et al. "Doping Level Dependence of Spin-Gap Behavior in Y(Ba1-xLax)2Cu3Oy Studied by Cu-NQR". In: *Journal of the Physical Society of Japan* 64.3 (1995), pp. 721–724. DOI: 10.1143/JPSJ.64.721. eprint: https://doi.org/10.1143/JPSJ.64.721. URL: https://doi.org/10.1143/JPSJ.64.721.

[130] M. Matsuura et al. "Development of spin-wave-like dispersive excitations below the pseudogap temperature in the high-temperature superconductor $La_{2-x}Sr_xCuO_4$". In: *Phys. Rev. B* 95 (2 2017), p. 024504. DOI: 10.1103/PhysRevB.95.024504. URL: https://link.aps.org/doi/10.1103/PhysRevB.95.024504.

[131] Toshiaki Matsuzaki et al. "Electronic Specific Heat of La2-xSrxCuO4: Pseudogap Formation and Reduction of the Superconducting Condensation Energy". In: *Journal of the Physical Society of Japan* 73.8 (2004), pp. 2232–2238. DOI: 10.1143/JPSJ.73.2232. eprint: https://doi.org/10.1143/JPSJ.73.2232. URL: https://doi.org/10.1143/JPSJ.73.2232.

[132] L. F. Mattheiss. "Electronic band properties and superconductivity in $La_{2-y}X_yCuO_4$". In: *Phys. Rev. Lett.* 58 (10 1987), pp. 1028–1030. DOI: 10.1103/PhysRevLett.58.1028. URL: https://link.aps.org/doi/10.1103/PhysRevLett.58.1028.

[133] Emanuel Maxwell. "Isotope Effect in the Superconductivity of Mercury". In: *Phys. Rev.* 78 (4 1950), pp. 477–477. DOI: 10.1103/PhysRev.78.477. URL: https://link.aps.org/doi/10.1103/PhysRev.78.477.

[134] V. V. Mazurenko, I. V. Solovyev, and A. A. Tsirlin. "Covalency effects reflected in the magnetic form factor of low-dimensional cuprates". In: *Phys. Rev. B* 92 (24 2015), p. 245113. DOI: 10.1103/PhysRevB.92.245113. URL: https://link.aps.org/doi/10.1103/PhysRevB.92.245113.

[135] Jianqiao Meng et al. "Coexistence of Fermi arcs and Fermi pockets in a high-Tc copper oxide superconductor". In: *Nature* 462 (2009), pp. 335–338. DOI: https://doi.org/10.1038/nature08521.

[136] B. Michon et al. "Importance of phase fluctuations in superconductors with small superfluid density". In: *Nature* 567 (2019), pp. 218–222. DOI: https://doi.org/10.1038/s41586-019-0932-x.

[137] Charles Mielke et al. "Superconducting properties and Fermi-surface topology of the quasi-two-dimensional organic superconductor λ-$(BETS)_2GaCl_4$(BETS≡bis(ethylenedithio)tetraselenafulvalene)". In: *Journal of Physics: Condensed Matter* 13.36 (2001), pp. 8325–8345. DOI: 10.1088/0953-8984/13/36/308. URL: https://doi.org/10.1088/0953-8984/13/36/308.

[138] P. Monthoux and D. Pines. "A nearly antiferromagnetic Fermi liquid". In: *Phys. Rev. B* 47 (10 1993), pp. 6069–6081. DOI: 10.1103/PhysRevB.47.6069. URL: https://link.aps.org/doi/10.1103/PhysRevB.47.6069.

[139] Takehiko Mori and Mao Katsuhara. "Estimation of πd-Interactions in Organic Conductors Including Magnetic Anions". In: *Journal of the Physical Society of Japan* 71.3 (2002), pp. 826–844. DOI: 10.1143/JPSJ.71.826. eprint: https://doi.org/10.1143/JPSJ.71.826. URL: https://doi.org/10.1143/JPSJ.71.826.

[140] Toru Moriya and Kazuo Ueda. "Spin fluctuations and high temperature superconductivity". In: *Advances in Physics* 49.5 (2000), pp. 555–606. DOI: 10.1080/000187300412248. eprint: https://doi.org/10.1080/000187300412248. URL: https://doi.org/10.1080/000187300412248.

[141] G.D. Morris et al. "Antiferromagnetism in solid oxygen". In: *Hyperfine Interac.* 104 (1997), pp. 381–385. DOI: https://doi.org/10.1023/A:1012641624313.

[142] K. A. Müller. "Large, small, and especially Jahn-Teller Polarons." In: *J. Supercond.* 12 (1999), pp. 3–7. DOI: https://doi.org/10.1023/A:1007792713484.

[143] K. Nagamine et al. "Construction of Riken-ral muon facility at ISIS and advanced μSR". In: *Hyperfine Interact.* 87 (1994), pp. 1091–1098. DOI: https://doi.org/10.1007/BF02068509.

[144] K. Nagamine et al. "Solitons in Polyacetylene Produced and Probed by Positive Muons". In: *Phys. Rev. Lett.* 53 (18 1984), pp. 1763–1766. DOI: 10.1103/PhysRevLett.53.1763. URL: https://link.aps.org/doi/10.1103/PhysRevLett.53.1763.

[145] Naoto Nagaosa. "Interlayer charge dynamics of the uniform resonating-valence-bond state". In: *Phys. Rev. B* 52 (14 1995), pp. 10561–10568. DOI: 10.1103/PhysRevB.52.10561. URL: https://link.aps.org/doi/10.1103/PhysRevB.52.10561.

[146] Naoto Nagaosa. "Superconductivity and Antiferromagnetism in High-Tc Cuprates". In: *Science* 275.5303 (1997), pp. 1078–1079. ISSN: 0036-8075. DOI: 10.1126/science.275.5303.1078. eprint: https://science.sciencemag.org/content. URL: https://science.sciencemag.org/content/275/5303/1078.

[147] T Naito et al. "Carrier dynamics in an organic magnetic superconductor and related salts κ, λ-(BETS)$_2$MCl$_4$(M = Fe, Ga)". In: *Journal of Physics: Condensed Matter* 22.18 (2010), p. 185701. DOI: 10.1088/0953-8984/22/18/185701. URL: https://doi.org/10.1088/0953-8984/22/18/185701.

[148] Y. Nakamura and S. Uchida. "Anisotropic transport properties of single-crystal $La_{2-x}Sr_xCuO_4$: Evidence for the dimensional crossover". In: *Phys. Rev. B* 47 (13 1993), pp. 8369–8372. DOI: 10.1103/PhysRevB.47.8369. URL: https://link.aps.org/doi/10.1103/PhysRevB.47.8369.

[149] M. R. Norman and J. C. Séamus Davis. "Quantum oscillations in a biaxial pair density wave state". In: *Proceedings of the National Academy of Sciences* 115.21 (2018), pp. 5389–5391. ISSN: 0027-8424. DOI: 10.1073/pnas.1803009115. eprint: https://www.pnas.org/content/115/21/5389.full.pdf. URL: https://www.pnas.org/content/115/21/5389.

[150] M. R. Norman, D. Pines, and C. Kallin. "The pseudogap: friend or foe of high Tc?". In: *Advances in Physics* 54.8 (2005), pp. 715–733. DOI: 10.1080/00018730500459906. eprint: https://doi.org/10.1080/00018730500459906. URL: https://doi.org/10.1080/00018730500459906.

[151] Shigeki Ohsugi et al. "Cu NMR and NQR Studies of High-T c Superconductor $La_{2-x}Sr_xCuO_4$". In: *Journal of the Physical Society of Japan* 63.2 (1994), pp. 700–715. DOI: 10.1143/JPSJ.63.700. eprint: https://doi.org/10.1143/JPSJ.63.700. URL: https://doi.org/10.1143/JPSJ.63.700.

[152] J. Orenstein and A. J. Millis. "Advances in the Physics of High-Temperature Superconductivity". In: *Science* 288.5465 (2000), pp. 468–474. ISSN: 0036-8075. DOI: 10.1126/science.288.5465.468. eprint: https://science.sciencemag.org/content/288/5465/468.full.pdf. URL: https://science.sciencemag.org/content/288/5465/468.

[153] A. Pal et al. "Quasistatic internal magnetic field detected in the pseudogap phase of $Bi_{2+x}Sr_{2-x}CaCu_2O_{8+\delta}$ by muon spin relaxation". In: *Phys. Rev. B* 97 (6 2018), p. 060502. DOI: 10.1103/PhysRevB.97.060502. URL: https://link.aps.org/doi/10.1103/PhysRevB.97.060502.

[154] R. G. Palmer et al. "Models of Hierarchically Constrained Dynamics for Glassy Relaxation". In: *Phys. Rev. Lett.* 53 (10 1984), pp. 958–961. DOI: 10.1103/PhysRevLett.53.958. URL: https://link.aps.org/doi/10.1103/PhysRevLett.53.958.

[155] C. Panagopoulos et al. "Evidence for a generic quantum transition in high-T_c cuprates". In: *Phys. Rev. B* 66 (6 2002), p. 064501. DOI: 10.1103/PhysRevB.66.064501. URL: https://link.aps.org/doi/10.1103/PhysRevB.66.064501.

[156] S. R. Park et al. "Broken relationship between superconducting pairing interaction and electronic dispersion kinks in $La_{2-x}Sr_xCuO_4$ measured by angle-resolved photoemission". In: *Phys. Rev. B* 88 (22 2013), p. 220503. DOI: 10.1103/PhysRevB.88.220503. URL: https://link.aps.org/doi/10.1103/PhysRevB.88.220503.

[157] P.A. Pattenden et al. "μSR studies of magnetism in the organic systems p-NPNN and 3-QNNN". In: *Synthetic Metals* 71.1 (1995). Proceedings of the International Conference on Science and Technology of Synthetic Metals (ICSM94), pp. 1823–1824. ISSN: 0379-6779. DOI: https://doi.org/10.1016/0379-6779(94)03068-H. URL: https://www.sciencedirect.com/science/article/pii/037967799403068H.

[158] A. Perali et al. "d-wave superconductivity near charge instabilities". In: *Phys. Rev. B* 54 (22 1996), pp. 16216–16225. DOI: 10.1103/PhysRevB.54.16216. URL: https://link.aps.org/doi/10.1103/PhysRevB.54.16216.

[159] Jason K. Perry, Jamil Tahir-Kheli, and William A. Goddard. "Ab initio evidence for the formation of impurity $d_{3z^2-r^2}$ holes in doped $La_{2-x}Sr_xCuO_4$". In: *Phys. Rev. B* 65 (14 2002), p. 144501. DOI: 10.1103/PhysRevB.65.144501. URL: https://link.aps.org/doi/10.1103/PhysRevB.65.144501.

[160] Jason K. Perry, Jamil Tahir-Kheli, and William A. Goddard. "Antiferromagnetic band structure of La_2CuO_4 : Becke-3–Lee-Yang-Parr calculations". In: *Phys. Rev. B* 63 (14 2001), p. 144510. DOI: 10.1103/PhysRevB.63.144510. URL: https://link.aps.org/doi/10.1103/PhysRevB.63.144510.

[161] Warren E. Pickett. "Electronic structure of the high-temperature oxide superconductors". In: *Rev. Mod. Phys.* 61 (2 1989), pp. 433–512. DOI: 10.1103/RevModPhys.61.433. URL: https://link.aps.org/doi/10.1103/RevModPhys.61.433.

[162] David Pines. "Nearly antiferromagnetic Fermi liquids: a progress report." In: *Z. Phys. B - Condensed Matter* 103 (1997), pp. 129–135. DOI: https://doi.org/10.1007/s002570050346.

[163] H. Pinkvos, A. Kalk, and Ch. Schwink. "Zero-field μSR measurements in CuMn and AuMn spin glasses interpreted in the frame of a fractal cluster model". In: *Phys. Rev. B* 41 (1 1990), pp. 590–607. DOI: 10.1103/PhysRevB.41.590. URL: https://link.aps.org/doi/10.1103/PhysRevB.41.590.

[164] Nikolay Plakida. *High-Temperature Cuprate Superconductors*. 1st ed. Berlin: Springer-Verlag Berlin Heidelberg, 2010. ISBN: 978-3-642-26483-2. DOI: 10.1007/978-3-642-12633-8.

[165] F. L. Pratt et al. "Low-Temperature Spin Diffusion in a Highly Ideal $S = \frac{1}{2}$ Heisenberg Antiferromagnetic Chain Studied by Muon Spin Relaxation". In: *Phys. Rev. Lett.* 96 (24 2006), p. 247203. DOI: 10.1103/PhysRevLett.96.247203. URL: https://link.aps.org/doi/10.1103/PhysRevLett.96.247203.

[166] E. Razzoli et al. "The Fermi surface and band folding in La2CuO4, probed by angle-resolved photoemission". In: *New Journal of Physics* 12.12 (2010), p. 125003. DOI: 10.1088/1367-2630/12/12/125003. URL: https://doi.org/10.1088/1367-2630/12/12/125003.

[167] J-Ph Reid et al. "From d-wave to s-wave pairing in the iron-pnictide superconductor (Ba,K)Fe2As2". In: *Superconductor Science and Technology* 25.8 (2012), p. 084013. DOI: 10.1088/0953-2048/25/8/084013. URL: https://doi.org/10.1088/0953-2048/25/8/084013.

[168] C. A. Reynolds, B. Serin, and L. B. Nesbitt. "The Isotope Effect in Superconductivity. I. Mercury". In: *Phys. Rev.* 84 (4 1951), pp. 691–694. DOI: 10.1103/PhysRev.84.691. URL: https://link.aps.org/doi/10.1103/PhysRev.84.691.

[169] Risdiana et al. "Muon spin relaxation study of the Cu spin dynamics in electron-doped high-T_c superconductor $Pr_{0.86}LaCe_{0.14}Cu_{1-y}Zn_yO_4$". In: *Phys. Rev. B* 82 (1 2010), p. 014506. DOI: 10.1103/PhysRevB.82.014506. URL: https://link.aps.org/doi/10.1103/PhysRevB.82.014506.

[170] H.O. Roccoa and A. Cruzado. "The Voigt Profile as a Sum of a Gaussian and a Lorentzian Functions, when the Weight Coefficient Depends on the Widths Ratio and the Independent Variable". In: *Acta Physica Polonica A* 122 (Oct. 2012), pp. 670–673. DOI: 10.12693/APhysPolA.122.670.

[171] A. G. Rojo and K. Levin. "Model for c-axis transport in high-T_c cuprates". In: *Phys. Rev. B* 48 (22 1993), pp. 16861–16864. DOI: 10.1103/PhysRevB.48.16861. URL: https://link.aps.org/doi/10.1103/PhysRevB.48.16861.

[172] R. Rousseau, M. Gener, and E. Canadell. "Step-by-Step Construction of the Electronic Structure of Molecular Conductors: Conceptual Aspects and Applications". In: *Advanced Functional Materials* 14.3 (2004), pp. 201–214. DOI: https://doi.org/10.1002/adfm.200305166. eprint: https://onlinelibrary.

wiley.com/doi/pdf/10.1002/adfm.200305166. URL: https://onlinelibrary.wiley.com/doi/abs/10.1002/adfm.200305166.

[173] Subir Sachdev. "Colloquium: Order and quantum phase transitions in the cuprate superconductors". In: *Rev. Mod. Phys.* 75 (3 2003), pp. 913–932. DOI: 10.1103/RevModPhys.75.913. URL: https://link.aps.org/doi/10.1103/RevModPhys.75.913.

[174] Subir Sachdev. "Emergent gauge fields and the high-temperature superconductors". In: *Phil. Trans. R. Soc. A* 374 (2016), p. 20150248. DOI: http://dx.doi.org/10.1098/rsta.2015.0248.

[175] Subir Sachdev. "Quantum Criticality: Competing Ground States in Low Dimensions". In: *Science* 288.5465 (2000), pp. 475–480. ISSN: 0036-8075. DOI: 10.1126/science.288.5465.475. eprint: https://science.sciencemag.org/content/288/5465/475.full.pdf. URL: https://science.sciencemag.org/content/288/5465/475.

[176] Subir Sachdev and N. Read. "Large N expansion for frustated and doped quantum antiferromagnets". In: *Int. J. Mod. Phys. B* 05 (1991), pp. 219–249. DOI: https://doi.org/10.1142/S0217979291000158.

[177] Subir Sachdev and Jinwu Ye. "Universal quantum-critical dynamics of two-dimensional antiferromagnets". In: *Phys. Rev. Lett.* 69 (16 1992), pp. 2411–2414. DOI: 10.1103/PhysRevLett.69.2411. URL: https://link.aps.org/doi/10.1103/PhysRevLett.69.2411.

[178] F. Sanchez-Bajo and F. L. Cumbrera. "The use of the pseudo-Voigt function in the variance method of X-ray line-broadening analysis. Erratum". In: *Journal of Applied Crystallography* 30.5 (1997), p. 550. DOI: 10.1107/S0021889897098956. URL: https://doi.org/10.1107/S0021889897098956.

[179] D. P. Sari et al. "Distorted Superconducting Nodal Line on Single Fermi Surface in Anisotropic Organic Superconductor λ-$(BETS)_2GaCl_4$". In: *Phys. Rev. Lett.* (2021).

[180] D P Sari et al. "μSR Study of Organic Superconductor λ-$(BETS)_2GaCl_4$". In: *IOP Conference Series: Materials Science and Engineering* 196 (2017), p. 012047. DOI: 10.1088/1757-899x/196/1/012047. URL: https://doi.org/10.1088/1757-899x/196/1/012047.

[181] Dita Puspita Sari et al. "Magnetic Study of the Lower Critical Field of Organic Superconductor λ-$(BETS)_2GaCl_4$". In: *Functional Properties of Modern Materials II*. Vol. 966. Materials Science Forum. Trans Tech Publications Ltd, Oct. 2019, pp. 296–301. DOI: 10.4028/www.scientific.net/MSF.966.296.

[182] Y. Sato et al. "Thermodynamic evidence for a nematic phase transition at the onset of the pseudogap in YBa2Cu3Oy". In: *Nat. Phys.* 13 (2017), pp. 1074–1078. DOI: https://doi.org/10.1038/nphys4205.

[183] D.J. Scalapino. "The case for dx2-y2 pairing in the cuprate superconductors". In: *Physics Reports* 250.6 (1995), pp. 329–365. ISSN: 0370-1573. DOI: https://doi.org/10.1016/0370-1573(94)00086-I. URL: https://www.sciencedirect.com/science/article/pii/037015739400086I.

[184] J. R. Schrieffer, X. G. Wen, and S. C. Zhang. "Dynamic spin fluctuations and the bag mechanism of high-T_c superconductivity". In: *Phys. Rev. B* 39 (16 1989), pp. 11663–11679. DOI: 10.1103/PhysRevB.39.11663. URL: https://link.aps.org/doi/10.1103/PhysRevB.39.11663.

[185] Zhi-xun Shen et al. "Anderson Hamiltonian description of the experimental electronic structure and magnetic interactions of copper oxide superconductors". In: *Phys. Rev. B* 36 (16 1987), pp. 8414–8428. DOI: 10.1103/PhysRevB.36.8414. URL: https://link.aps.org/doi/10.1103/PhysRevB.36.8414.

[186] M. Shi et al. "Coherent *d*-Wave Superconducting Gap in Underdoped $La_{2-x}Sr_xCuO_4$ by Angle-Resolved Photoemission Spectroscopy". In: *Phys. Rev. Lett.* 101 (4 2008), p. 047002. DOI: 10.1103/PhysRevLett.101.047002. URL: https://link.aps.org/doi/10.1103/PhysRevLett.101.047002.

[187] T. Shibauchi, A. Carrington, and Y. Matsuda. "A Quantum Critical Point Lying Beneath the Superconducting Dome in Iron Pnictides". In: *Annual Review of Condensed Matter Physics* 5.1 (2014), pp. 113–135. DOI: 10.1146/annurev-conmatphys-031113-133921. eprint: https://doi.org/10.1146/annurev-conmatphys-031113-133921. URL: https://doi.org/10.1146/annurev-conmatphys-031113-133921.

[188] Robert H. Silsbee and Daniel W. Hone. "Comment on motional narrowing". In: *Phys. Rev. B* 27 (1 1983), pp. 85–88. DOI: 10.1103/PhysRevB.27.85. URL: https://link.aps.org/doi/10.1103/PhysRevB.27.85.

[189] Alexander Sokol and David Pines. "Toward a unified magnetic phase diagram of the cuprate superconductors". In: *Phys. Rev. Lett.* 71 (17 1993), pp. 2813–2816. DOI: 10.1103/PhysRevLett.71.2813. URL: https://link.aps.org/doi/10.1103/PhysRevLett.71.2813.

[190] J. E. Sonier et al. "Anomalous Weak Magnetism in Superconducting YBa2Cu3O_{6+x}". In: *Science* 292.5522 (2001), pp. 1692–1695. ISSN: 0036-8075. DOI: 10.1126/science.1060844. eprint: https://science.sciencemag.org/content/292/5522/1692.full.pdf. URL: https://science.sciencemag.org/content/292/5522/1692.

[191] J. E. Sonier et al. "Correlations between charge ordering and local magnetic fields in overdoped $YBa_2Cu_3O_{6+x}$". In: *Phys. Rev. B* 66 (13 2002), p. 134501. DOI: 10.1103/PhysRevB.66.134501. URL: https://link.aps.org/doi/10.1103/PhysRevB.66.134501.

[192] J. E. Sonier et al. "Direct search for a ferromagnetic phase in a heavily overdoped nonsuperconducting copper oxide". In: *Proceedings of the National Academy of Sciences* 107.40 (2010), pp. 17131–17134. ISSN: 0027-8424. DOI: 10.1073/pnas.1007079107. eprint: https://www.pnas.org/content/107/40/17131.full.pdf. URL: https://www.pnas.org/content/107/40/17131.

[193] J. E. Sonier et al. "Spin-glass state of individual magnetic vortices in $YBa_2Cu_3O_y$ and $La_{2-x}Sr_xCuO_4$ below the metal-to-insulator crossover". In: *Phys. Rev. B* 76 (6 2007), p. 064522. DOI: 10.1103/PhysRevB.76.064522. URL: https://link.aps.org/doi/10.1103/PhysRevB.76.064522.

[194] T. Startseva et al. "Temperature evolution of the pseudogap state in the infrared response of underdoped $La_{2-x}Sr_xCuO_4$". In: *Phys. Rev. B* 59 (10 1999), pp. 7184–7190. DOI: 10.1103/PhysRevB.59.7184. URL: https://link.aps.org/doi/10.1103/PhysRevB.59.7184.

[195] Yen-Sheng Su et al. "Crystal Hartree-Fock calculations for La_2NiO_4 and La_2CuO_4". In: *Phys. Rev. B* 59 (16 1999), pp. 10521–10529. DOI: 10.1103/PhysRevB.59.10521. URL: https://link.aps.org/doi/10.1103/PhysRevB.59.10521.

[196] Jun Sugiyama et al. "Li Diffusion in Li_xCoO_2 Probed by Muon-Spin Spectroscopy". In: *Phys. Rev. Lett.* 103 (14 2009), p. 147601. DOI: 10.1103/PhysRevLett.103.147601. URL: https://link.aps.org/doi/10.1103/PhysRevLett.103.147601.

[197] Axel Svane. "Electronic structure of La_2CuO_4 in the self-interaction-corrected density-functional formalism". In: *Phys. Rev. Lett.* 68 (12 1992), pp. 1900–1903. DOI: 10.1103/PhysRevLett.68.1900. URL: https://link.aps.org/doi/10.1103/PhysRevLett.68.1900.

[198] Louis Taillefer. "Scattering and Pairing in Cuprate Superconductors". In: *Annual Review of Condensed Matter Physics* 1.1 (2010), pp. 51–70. DOI: 10.1146/annurev-conmatphys-070909-104117. eprint: https://doi.org/10.1146/annurev-conmatphys-070909-104117. URL: https://doi.org/10.1146/annurev-conmatphys-070909-104117.

[199] J. Takeya et al. "Low-Temperature Electronic Heat Transport in $La_{2-x}Sr_xCuO_4$ Single Crystals: Unusual Low-Energy Physics in the Normal and Superconducting States". In: *Phys. Rev. Lett.* 88 (7 2002), p. 077001. DOI: 10.1103/PhysRevLett.88.077001. URL: https://link.aps.org/doi/10.1103/PhysRevLett.88.077001.

[200] H Tanaka et al. "Chemical Control of Electrical Properties and Phase Diagram of a Series of λ-Type BETS Superconductors, λ-$(BETS)_2GaBr_xCl_{4-x}$". In: *J. Am. Chem. Soc.* 121 (1999), pp. 760–768. DOI: https://doi.org/10.1021/ja9827806.

[201] J. M. Tranquada et al. "Coexistence of, and Competition between, Superconductivity and Charge-Stripe Order in $La_{1.6-x}Nd_{0.4}Sr_xCuO_4$". In: *Phys. Rev. Lett.* 78 (2 1997), pp. 338–341. DOI: 10.1103/PhysRevLett.78.338. URL: https://link.aps.org/doi/10.1103/PhysRevLett.78.338.

[202] C. C. Tsuei and J. R. Kirtley. "Pairing symmetry in cuprate superconductors". In: *Rev. Mod. Phys.* 72 (4 2000), pp. 969–1016. DOI: 10.1103/RevModPhys.72.969. URL: https://link.aps.org/doi/10.1103/RevModPhys.72.969.

[203] Y. J. Uemura. "Muon spin relaxation studies on high-TC superconductors and related antiferromagnets (invited)". In: *Journal of Applied Physics* 64.10 (1988), pp. 6087–6091. DOI: 10.1063/1.342127. eprint: https://doi.org/10.1063/1.342127. URL: https://doi.org/10.1063/1.342127.

[204] Y. J. Uemura. "μSR relaxation in magnetic materials". In: *Muon Science: Muons in Physics, Chemistry and Materials*. Ed. by S. L. Lee, R. Cywinski, and S. H. Kilcoyne. 1st ed. Scodland: CRC Press, 1999, pp. 85–114.

[205] Y. J. Uemura et al. "Muon-spin relaxation in AuFe and CuMn spin glasses". In: *Phys. Rev. B* 31 (1 1985), pp. 546–563. DOI: 10.1103/PhysRevB.31.546. URL: https://link.aps.org/doi/10.1103/PhysRevB.31.546.

[206] D. Vaknin et al. "Antiferromagnetism in La_2CuO_{4-y}". In: *Phys. Rev. Lett.* 58 (26 1987), pp. 2802–2805. DOI: 10.1103/PhysRevLett.58.2802. URL: https://link.aps.org/doi/10.1103/PhysRevLett.58.2802.

[207] C. M. Varma. "Non-Fermi-liquid states and pairing instability of a general model of copper oxide metals". In: *Phys. Rev. B* 55 (21 1997), pp. 14554–14580. DOI: 10.1103/PhysRevB.55.14554. URL: https://link.aps.org/doi/10.1103/PhysRevB.55.14554.

[208] C. M. Varma. "Pseudogap Phase and the Quantum Critical Point in Copper-Oxide Metals". In: *Phys. Rev. Lett.* 83 (17 1999), pp. 3538–3541. DOI: 10.1103/PhysRevLett.83.3538. URL: https://link.aps.org/doi/10.1103/PhysRevLett.83.3538.

[209] C. M. Varma. "Theory of Copper-Oxide Metals". In: *Phys. Rev. Lett.* 75 (5 1995), pp. 898–901. DOI: 10.1103/PhysRevLett.75.898. URL: https://link.aps.org/doi/10.1103/PhysRevLett.75.898.

[210] C. M. Varma. "Theory of the pseudogap state of the cuprates". In: *Phys. Rev. B* 73 (15 2006), p. 155113. DOI: 10.1103/PhysRevB.73.155113. URL: https://link.aps.org/doi/10.1103/PhysRevB.73.155113.

[211] C. M. Varma and Lijun Zhu. "Topological Transition in the Fermi Surface of Cuprate Superconductors in the Pseudogap Regime". In: *Phys. Rev. Lett.* 98 (17 2007), p. 177004. DOI: 10.1103/PhysRevLett.98.177004. URL: https://link.aps.org/doi/10.1103/PhysRevLett.98.177004.

[212] I. Vishick. "Low energy excitations in cuprate high temperature superconductors: ARPES studies". PhD thesis. Stanford University, 2013.

[213] Matthias Vojta. "Lattice symmetry breaking in cuprate superconductors: stripes, nematics, and superconductivity". In: *Advances in Physics* 58.6 (2009), pp. 699–820. DOI: 10.1080/00018730903122242. eprint: https://doi.org/10.1080/00018730903122242. URL: https://doi.org/10.1080/00018730903122242.

[214] S. Wakimoto et al. "Observation of incommensurate magnetic correlations at the lower critical concentration for superconductivity in $La_{2-x}Sr_xCuO_4$ ($x = 0.05$)". In: *Phys. Rev. B* 60 (2 1999), R769–R772. DOI: 10.1103/PhysRevB.60.R769. URL: https://link.aps.org/doi/10.1103/PhysRevB.60.R769.

[215] Andrew C. Walters et al. "Energy gaps in high-transition-temperature cuprate superconductors". In: *Nat. phys.* 5 (2009), pp. 867–872. DOI: https://doi.org/10.1038/nphys1405.

[216] I. Watanabe et al. "Muon-spin-relaxation study of the effect of nonmagnetic impurities on the Cu-spin fluctuations in $La_{2-x}Sr_xCu_{1-y}Zn_yO_4$ around $x = 0.115$". In: *Phys. Rev. B* 65 (18 2002), p. 180516. DOI: 10.1103/PhysRevB.65.180516. URL: https://link.aps.org/doi/10.1103/PhysRevB.65.180516.

[217] Isao Watanabe. "^{139}La NQR Study of the Magnetic Properties of La2-xMxCuO4 (M=Ba, Sr) for $0 \leq x \leq 0.08$". In: *Journal of the Physical Society of Japan* 63.4 (1994), pp. 1560–1571. DOI: 10.1143/JPSJ.63.1560. eprint: https://doi.org/10.1143/JPSJ.63.1560. URL: https://doi.org/10.1143/JPSJ.63.1560.

[218] Isao Watanabe et al. "Change of the Dynamics of Internal Fields in the Normal State of $La_{2-x}Sr_xCuO_4$ Observed by Muon-Spin-Relaxation". In: *Journal of the Physical Society of Japan* 77.12 (2008), p. 124716. DOI: 10.1143/JPSJ.77.124716. eprint: https://doi.org/10.1143/JPSJ.77.124716. URL: https://doi.org/10.1143/JPSJ.77.124716.

[219] Isao Watanabe et al. "Muon-spin-relaxation study of the ground state of the two-dimensional $S = 1$ kagoméantiferromagnet [2-(3-N-methyl-pyridium)-4,4,5,5-tetramethyl-4,5-dihydro-1H-imidazol-1-oxyl 3-N-oxide]BF_4". In: *Phys. Rev. B* 58 (5 1998), pp. 2438–2441. DOI: 10.1103/PhysRevB.58.2438. URL: https://link.aps.org/doi/10.1103/PhysRevB.58.2438.

[220] Pan Wei and Zheng Qing Qi. "Electronic structure of La_2CuO_4 and $YBa_2Cu_3O_6$: A local-spin-density approximation with on-site Coulomb-U correlation calculations". In: *Phys. Rev. B* 49 (17 1994), pp. 12159–12164. DOI: 10.1103/PhysRevB.49.12159. URL: https://link.aps.org/doi/10.1103/PhysRevB.49.12159.

[221] B. O. Wells et al. "E versus k Relations and Many Body Effects in the Model Insulating Copper Oxide $Sr_2CuO_2Cl_2$". In: *Phys. Rev. Lett.* 74 (6 1995), pp. 964–967. DOI: 10.1103/PhysRevLett.74.964. URL: https://link.aps.org/doi/10.1103/PhysRevLett.74.964.

[222] J. J. Wen et al. "Observation of two types of charge-density-wave orders in superconducting $La_{2-x}Sr_xCuO_4$". In: *Nat. commun.* 10 (2019), p. 3269. DOI: https://doi.org/10.1038/s41467-019-11167-z.

[223] G. K. Wertheim et al. "Determination of the Gaussian and Lorentzian content of experimental line shapes". In: *Review of Scientific Instruments* 45.11 (1974), pp. 1369–1371. DOI: 10.1063/1.1686503. eprint: https://doi.org/10.1063/1.1686503. URL: https://doi.org/10.1063/1.1686503.

[224] Robert C. Williams. "Correlated magnetic oxides studied using muon−spin spectroscopy". PhD thesis. Durham University, 2016.

[225] D. A. Wollman et al. "Experimental determination of the superconducting pairing state in YBCO from the phase coherence of YBCO-Pb dc SQUIDs". In: *Phys. Rev. Lett.* 71 (13 1993), pp. 2134–2137. DOI: 10.1103/PhysRevLett.71.2134. URL: https://link.aps.org/doi/10.1103/PhysRevLett.71.2134.

[226] C. S. Wu et al. "Experimental Test of Parity Conservation in Beta Decay". In: *Phys. Rev.* 105 (4 1957), pp. 1413–1415. DOI: 10.1103/PhysRev.105.1413. URL: https://link.aps.org/doi/10.1103/PhysRev.105.1413.

[227] J. Wu et al. "Spontaneous breaking of rotational symmetry in copper oxide superconductors". In: *Nature* 547 (2017), pp. 432–435. DOI: https://doi.org/10.1038/nature23290.

[228] B. Wuyts, V. V. Moshchalkov, and Y. Bruynseraede. "Resistivity and Hall effect of metallic oxygen-deficient $YBa_2Cu_3O_x$ films in the normal state". In: *Phys. Rev. B* 53 (14 1996), pp. 9418–9432. DOI: 10.1103/PhysRevB.53.9418. URL: https://link.aps.org/doi/10.1103/PhysRevB.53.9418.

[229] Jing Xia et al. "Polar Kerr-Effect Measurements of the High-Temperature $YBa_2Cu_3O_{6+x}$ Superconductor: Evidence for Broken Symmetry near the Pseudogap Temperature". In: *Phys. Rev. Lett.* 100 (12 2008), p. 127002. DOI: 10.1103/PhysRevLett.100.127002. URL: https://link.aps.org/doi/10.1103/PhysRevLett.100.127002.

[230] K. Yamada et al. "Doping dependence of the spatially modulated dynamical spin correlations and the superconducting-transition temperature in $La_{2-x}Sr_xCuO_4$". In: *Phys. Rev. B* 57 (10 1998), pp. 6165–6172. DOI: 10.1103/PhysRevB.57.6165. URL: https://link.aps.org/doi/10.1103/PhysRevB.57.6165.

[231] A. Yaouanc and P. D. de Reotier. *Muon Spin Rotation, Relaxation, and Resonance: Applications to Condensed Matter*. 1st ed. Oxford: Oxford Univ. Press, 2011. ISBN: 9780199596478.

[232] Syuma Yasuzuka et al. "In-Plane Anisotropy of Flux-Flow Resistivity in Layered Organic Superconductor λ-$(BETS)_2GaCl_4$". In: *Journal of the Physical Society of Japan* 83.1 (2014), p. 013705. DOI: 10.7566/JPSJ.83.013705. eprint: https://doi.org/10.7566/JPSJ.83.013705. URL: https://doi.org/10.7566/JPSJ.83.013705.

[233] T. Yoshida et al. "Systematic doping evolution of the underlying Fermi surface of $La_{2-x}Sr_xCuO_4$". In: *Phys. Rev. B* 74 (22 2006), p. 224510. DOI: 10.1103/PhysRevB.74.224510. URL: https://link.aps.org/doi/10.1103/PhysRevB.74.224510.

[234] Jaejun Yu, A. J. Freeman, and J. H. Xu. "Electronically driven instabilities and superconductivity in the layered $La_{2-x}Ba_xCuO_4$ perovskites". In: *Phys. Rev. Lett.* 58 (10 1987), pp. 1035–1037. DOI: 10.1103/PhysRevLett.58.1035. URL: https://link.aps.org/doi/10.1103/PhysRevLett.58.1035.

[235] Jan Zaanen and Olle Gunnarsson. "Charged magnetic domain lines and the magnetism of high-T_c oxides". In: *Phys. Rev. B* 40 (10 1989), pp. 7391–7394. DOI: 10.1103/PhysRevB.40.7391. URL: https://link.aps.org/doi/10.1103/PhysRevB.40.7391.

[236] Jian Zhang et al. "Discovery of slow magnetic fluctuations and critical slowing down in the pseudogap phase of $YBa_2Cu_3O_y$". In: *Science Advances* 4.1 (2018). DOI: 10.1126/sciadv.aao5235. eprint: https://advances.sciencemag.org/content/4/1/eaao5235.full.pdf. URL: https://advances.sciencemag.org/content/4/1/eaao5235.

[237] X. G. Zheng et al. "Finite-size effect on Neel temperature in antiferromagnetic nanoparticles". In: *Phys. Rev. B* 72 (1 2005), p. 014464. DOI: 10.1103/PhysRevB.72.014464. URL: https://link.aps.org/doi/10.1103/PhysRevB.72.014464.

[238] X. J. Zhou et al. "Universal nodal Fermi velocity". In: *Nature* 423 (2003), p. 398. DOI: https://doi.org/10.1038/423398a.

[239] Xuetao Zhu et al. "Classification of charge density waves based on their nature". In: *Proceedings of the National Academy of Sciences* 112.8 (2015), pp. 2367–2371. ISSN: 0027-8424. DOI: 10.1073/pnas.1424791112. eprint: https://www.pnas.org/content/112/8/2367.full.pdf. URL: https://www.pnas.org/content/112/8/2367.